5-2016

Inter-droplet Membranes for Mechanical Sensing Applications

Nima Tamaddoni Jahromi
University of Tennessee - Knoxville, ntamaddo@vols.utk.edu

To the Graduate Council:

I am submitting herewith a dissertation written by Nima Tamaddoni Jahromi entitled "Inter-droplet Membranes for Mechanical Sensing Applications." I have examined the final electronic copy of this dissertation for form and content and recommend that it be accepted in partial fulfillment of the requirements for the degree of Doctor of Philosophy, with a major in Mechanical Engineering.

Stephen A. Sarles, Major Professor

We have read this dissertation and recommend its acceptance:

Eric Freeman, William Hamel, Michael Kilbey, Xiaopeng Zhao

Accepted for the Council:

Carolyn R. Hodges

Vice Provost and Dean of the Graduate School

(Original signatures are on file with official student records.)

Inter-droplet Membranes for Mechanical Sensing Applications

A Dissertation Presented for the
Doctor of Philosophy
Degree
The University of Tennessee, Knoxville

Nima Tamaddoni Jahromi
May 2016

DEDICATION

I dedicate my work to my supportive family:

Mitra Hashemian, Mom

Essy Tamaddoni, Dad

Vida Hashemian, Aunt

Hash Hashemian, Uncle

Tina Tamaddoni, Sister

Tannaz Tamaddoni, Sister

Sindokht Hashemian, Grand Mother

Mehrad Hashemian, Uncle

Mehrtash Hashemian, Uncle

Nazzy Hashemian, Aunt

Amme Mehri, Aunt

And to my supportive and lovely cousins, nieces and nephew.

ACKNOWLEDGEMENTS

I would never have been able to finish my dissertation without the guidance of my outstanding Advisor Dr. Andy Sarles. I would like to express my deepest gratitude to my advisor for his excellent leadership, caring, patience, and providing me with an excellent atmosphere for doing research.

I would also like to sincerely thank my committee members, Professor Hamel, Professor Kilbey, Professor Xiaopeng and Professor Freeman for their guidance and suggestions during my PhD studies and taking the time for being an active member in my committee. I like to give a special thank you to Dr. Graham Taylor who brought his valuable experiences from industry to our laboratory. Also I like to sincerely thank my great lab mates Guru Venkatesan and Mary-Anne Nguyen. Also I like to thank Trevor Hepburn, undergraduate research assistant, for helping me conducting some of experimental testing's. Moreover I like to thank Dr. Hulsey for allowing us to conduct all the high speed imaging experiments and recordings in his lab.

I also like to thank Dr. Larry Sharpe and Dr. Douglass for their guidance and supervision during my teaching assistantship in their Dynamics, Mechanics of Materials and Manufacturing Processes.

ABSTRACT

This dissertation combines self-assembly phenomena of amphiphilic molecules with soft materials to create and characterize mechanoelectrical transducers and sensors whose sensing elements are thin-film bioinspired membranes comprised of phospholipids or amphiphilic polymers. We show that the structures of these amphiphilic molecules tune the mechanical and electrical properties of these membranes. We show that these properties affect the mechanoelectrical sensing characteristic and range of operation of these membrane transducers. In the experiments, we construct and characterize a membrane-based hair cell embodiment that enables the membrane to be responsive to mechanical perturbations of the hair. The resulting oscillations of membranes formed between droplets produces measurable current due to the time rate of change of the electrical capacitance of the vibrating membranes. In addition to sensors that feature a single membrane between two droplets, we also study mechanoelectrical transduction in multi-membrane, multi-hair Droplet Interface Bilayer (DIB) array networks formed from more than two droplets. In this work, we show for the first time that multi-membrane Droplet Interface Bilayer (DIB) networks can be used to enhance the sensitivity and frequency selectivity of these sensors.

Therefore, we utilized the same self-assembly phenomena to form more stable and robust interfaces between droplet using synthetic polymers. Copolymer Stabilized Interfaces (CSIs) are formed between triblock polymer-coated

aqueous droplets in alkanes and silicone oil, and we demonstrate that, unlike lipid-coated droplets, triblock-coated droplets do not spontaneously adhere in oil when the organic phase is a good solvent for the hydrophobic PDMS block.

Interestingly, a thinned planar membrane between droplets can be reversibly formed upon the application of sufficient voltage across the interface, which we believe works to remove excess solvent through electro-compression. These results thus show new capability for initiating, controlling, and disconnecting polymer-stabilized membranes between aqueous droplets. These membranes also exhibit wider range of airflow operation when used to construct a hair cell sensors.

TABLE OF CONTENTS

LIST OF TABLES

LIST OF FIGURES

CHAPTER 1: INTRODUCTION AND LITERATURE REVIEW

1.1 Introduction and Motivation

1.1.1 Sensory Hair Cells in Nature

A common feature of all vertebrate species is the use of sensory hairs, or hair cells, to sense sound, inertia tilt, and acceleration [9-12], fluid flow [13], and vibrations [14, 15]. The shared feature of sensory hairs across species, as the name suggests, is the use of protruding “hair-like” structures called cilia [16] that extend from the body of the cell into the surrounding environment (Figure 1). The transduction process works in a few basic steps: First, a physical stimulus such as airflow causes the cilia to deflect. These deflections trigger mechanically sensitive biomolecules [17, 18] contained in the cell membrane to open, thereby changing the internal potential of the cell. Finally, this change in potential leads to the generation of a nerve impulse that is sent to the brain. Building on this basic transduction process, nature has evolved many variants of hair cells, whereby subtle changes in the size and length of the cilia, and in how the cilia interface with the surrounding environment enables a wide range of selectivity and sensitivity [19, 20]. Moreover, in humans, inner and outer hair cells are particularly important in hearing, while vestibular hair cells, also located in the inner ear, are used in detecting changes in position (and rotation) of the head [21, 22].

Nature uses biological soft materials such as cell membrane containing proteins and lipids for transduction mechanisms. The fact that cell membranes provide key functionality to transduction processes [23, 24], indicates the potential of these structures for mechanotransduction sensing. Stretch-activated ion channels, has been shown to contribute to mechanotransduction responses [25-28]. These cell membranes exhibit several limitations such as fragility, difficult for in-vitro assembly and portability, which make them difficult to rebuild them and utilize them out of nature.

In the past few years, different examples of biomimetic hair cell sensors have been developed using synthetic materials like piezoelectric and Micro-Electro-Mechanical Systems (MEMS) [29-34]. Each of these embodiments produces an electrical response as a result of the deflection of an artificial hair. All of these bio-inspired designs employ an artificial hair structure for mechanical sensing or

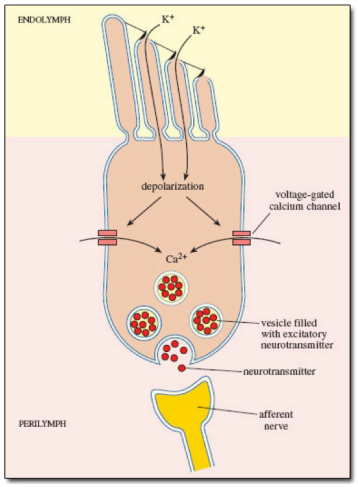

Figure 1: Schematic of hair cell sensor mechanism. Depolarization of hair cell due to flow-coupled deflection of stereocilia (reproduced from [1]).

actuation. Examples include an airflow velocity sensor [35, 36], an oscillating flow sensor [37], a magnetostrictive force sensor [5], a microparticle actuator [38], and an underwater directional flow sensor [36, 39, 40]. One significant difference between these man-made designs and natural hair cells is the use of engineered transducers (i.e. cantilever beams and solid materials) in place of biomolecules to perform transduction. There are some limitations involved with synthetic materials such as heavy weights 7800 kg/m3 [41], space and high energy consumption (hundreds of volts [42]) . Moreover, piezo-electric crystals resonate at frequencies of about 10 kilohertz or more while soft substances such as biological tissues or fluids produce resonate peaks at less than 1 Kilohertz [43-48].

1.1.2 Vision of New Class of Nature-Inspired Membrane-Based Sensors

Scientists combined phospholipid self-assembly methods with soft materials to create an artificial cell membranes as lipid bilayers [49, 50]. Bayley's group, for the first time, were able to form these artificial lipid membranes in between droplets that is called Droplet Interface Bilayers (DIBs) [51]. Lipid bilayers do not have many limitations of natural cell membrane and can form a more stable and durable membranes.

In contrast to other hair cell inspired sensor devices, DIBs are comprised of soft, nanoscale materials, which are light weight (5nm thick membranes) and can be operated with low energy consumption (less than 100mV) to form new class of smart materials. New class of bio-material based hair cell sensors the use

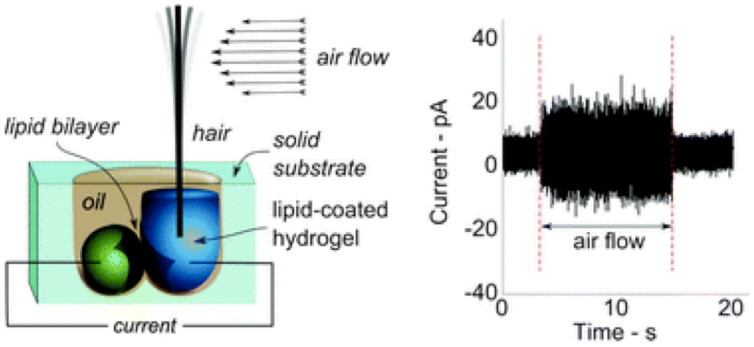

Figure 2: Initial embodiment of hair cell sensors (reproduced from [3]).

inexpensive, light weight soft biomolecules with low energy consumption are first introduced by Sarles and Leo in 2011 [4] as shown in Figure 2. Their sensor featured an artificial cell membrane as the sensing transducer element which used to mimic hair cell mechanotransduction in vertebrates [4]. While this first embodiment produced a sufficient sensitivity to hair motion, the sensor exhibited several limitations. These include low mechanical stability, poor membrane durability due to excessive hair motion, membrane fragility, low sensitivity, and undefined directionality. Our vision is to develop and characterize highly durable membrane based hair cell sensors using sensitivity and frequency tunable soft materials.

1.1.3 Broader Impacts

Our proposed systems offers a new opportunity and approach based on the using of soft materials to produce a low cost and light sensing device which can sense, in low range of frequencies. This innovation could have industrial, scientific, and medical applications in small-scale environment with low cost. Our

broader goal to make an array of membrane-based sensing devices with tunable mechanical and electrical properties for desired range of operation and sensitivities.

In big picture, the possible future innovation centers around the measurement of capacitive membranes formed between aqueous volumes as they deform in response to stimuli such as flow. The sensor can be used to produce better medical devices such as highly sensitive hearing aids, which are highly fluid in a small scale [52-54]. As importantly, the concept could have application in micro-fluidic research leading to innovations in medical diagnostics and energy harvesting systems.

1.1.4 Distinguishing Approach

In this work we utilize, develop and study the mechanotransduction responses of intra-droplet membrane-based systems that are: 1) durable due to the fact that they are not physically coupled to a solid support [55], 2) easy to assemble bilayers form spontaneously between droplets, which can be rearranged and reconfigured [56], 3) stable under vibration [3] 4) portable, because these systems can be integrated into microfluidic environments, they can be packaged in solid substrate[55], and 5) the self-assembly process works across a large range of droplet length scales.

1.2 Literature Review

1.2.1 Synthetic Lipid Bilayers

The cell membrane is a biological bilayer that works as a fluid barrier in all cells, separating the interior of the cell from the extracellular matrix [57, 58]. Proteins [59], enzymes [60], cholesterols [61-63] selectively insert, and ions transfer [64-66], across the membrane, which help the intracellular matrix to communicate with the extracellular matrix. Figure 3 shows the schematics of (a) cell and (b) cell membrane. The key components of these semipermeable membranes are phospholipids (Figure 3c). As shown in Figure 3c, the phospholipid structure contains a polar hydrophilic (i.e., water-seeking) head group and a hydrophobic (water-repelling) tail group [67]. The membrane formed by the self-assembly of these amphiphilic molecules is shown in this figure. A number of studies have investigated the electrical [68-70], and mechanical [71] properties of cell membranes; however, the complexity of natural membranes and the fact that they may contain multiple membrane proteins and various types of lipids makes

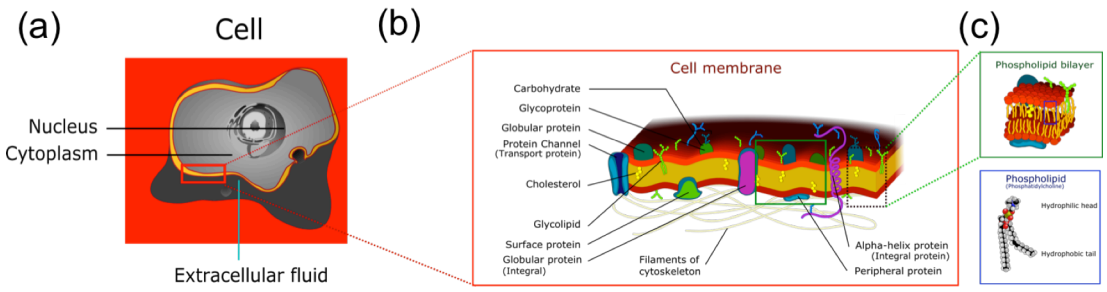

Figure 3: The schematics of complex cell membrane.

them difficult to work with and to characterize them in detail; the techniques required to investigate natural membranes are also labor-intensive and time consuming. To overcome these challenges, many researchers have taken up the study of synthetic lipid bilayers, investigating a wide range of phenomena, including protein insertion [72-74] and the permeability of cell membrane [75-77]. To study the cell membrane synthetically, synthetic lipid bilayers that mimic natural cell membrane structures are formed in-vitro [51, 78, 79] in simpler manner to be able to study the characteristics of these membranes.

Various methods for forming these synthetic bilayers have been developed, including lipid vesicles [80], black lipid membranes (BLM) [50, 81], supported lipid bilayers (SLB) [82-86] and tethered bilayer lipid membranes (t-BLM) [87-89]. One promising kind of lipid bilayers, invented by Bayley and referred to as droplet interface bilayers (DIBs), forms at the boundary between droplets [51]. Advantage of DIBs over other lipid bilayer formations is the small volume of the droplets, ease of assembly and portability, while other methods of bilayer formation require a large-volume bilayer chamber (100μL or more), which makes this embodiment less practical and more expensive than others [55].

1.2.2 Droplet Interface Bilayers

The key components of lipid bilayers are the phospholipid molecules (Figure 4a). The self-assembly of these amphiphilic molecules are derived by hydrophobic effect [90-92] and thermodynamically repulsion forces between the water and the hydrophobic regions of the lipids. The hydrophobic interaction is an entropic

effect originating from disturbance of hydrogen bonds between water molecules and non-polar solvents. These amphiphilic lipid molecules in water form aggregates with different structures of micelles, planar lipid bilayers, and spherical lipid bilayers known as vesicles or liposomes [93-95].

Placing lipid-encased water droplets under the oil causes amphiphilic phospholipids to self-assemble on the water-oil interface, where the hydrophilic head groups remain in water and the hydrophobic tails remain outside of the droplets. Phospholipid self-assembly leads to two monolayers of these amphiphilic molecules on the surface of droplets under the oil to form lipid bilayers by excluding oil between the droplets (Figure 4b).

As the droplets come together, each monolayers assembled on each droplet become adhered together by: 1) entropic effect of monolayer hydrophobic chains that do not mix with the solvent cause the exclusion of oil [96], and 2) van der Waals attractions of hydrophobic chains at close distances to form a planar lipid bilayer termed a “droplet interface bilayer” (DIB) [51]. Droplet adhesion is an entropically-deriven process that favors the exclusion of excess solvent molecules from between the hydrophobic tails of the lipid coating each droplet. As a result, the increase in entropy and thus the adhesion depends on the solubility of the solvent in the monolayers. For example in a very poor solvent you get the maximum change of entropy and the oil is fully excluded whereas in a good solvent, the entropy of the system does not change as much due to high solubility of chains and the oil partially stays in membranes. As a result in

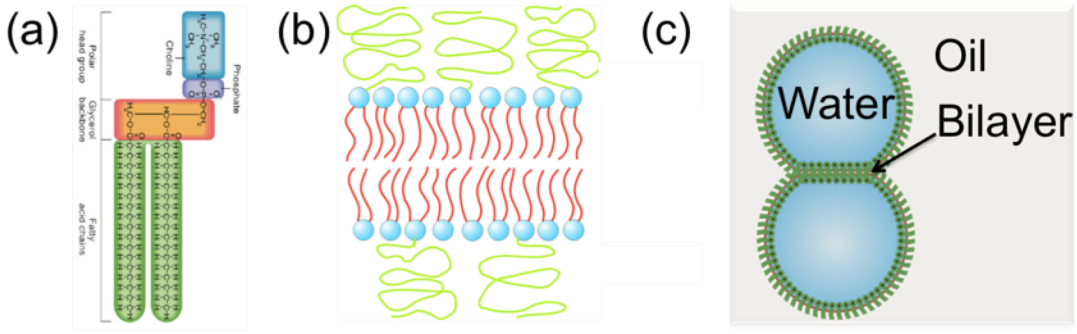

Figure 4: (a) Schematic of phospholipid molecule with a hydrophilic head and hydrophobic tails and with a glycerol backbone that connects these two sections, (b) Schematic of lipid bilayer as the hydrophobic section zips together and hydrophilic heads stays in water phase, (c) Schematic of droplet interface bilayer.

spontaneous adhesion allow the system to reduce the total free energy and the reduction of free energy of the system can be shown in equation below:

$$\Delta F = 2\gamma_m(1-\cos\theta) \qquad \textbf{Equation 1}$$

where the γ_m is the monolayer tension and θ is the contact angle of adhered droplets. The thickness of the planar DPhPC lipid membrane formed between the two droplets is approximately 5 nm [97]. The droplet interface bilayer, shown in Figure 4c, allows the formation of durable, liquid-supported lipid bilayer at the interface of connected, lipid-encased aqueous droplets submersed in oil.

Note that various types of amphiphilic molecules—including amphiphilic polymers [98]—can produce these types of membrane structures by means of self-assembly [55, 99]. Additionally, as previous research has shown, the portable system can be used for a wide variety of environmental biomolecule sensing

measurements [85, 100, 101]. Functionalities of synthetic lipid bilayers are not limited only to these applications and by understanding and improving its mechanical, electrical and chemical properties; they can be feasibly used as a new type of smart structures in various engineering and healthcare applications.

Supported lipid bilayers have several limitations such as fragility and short life time, hard and expensive to recreate and time consuming. To date DIBs are introduced variety of new possibilities that cannot be provided by supported lipid bilayers. Thus far single DIBs and DIB networks have been constructed to study large number of protein interactions with membranes [55, 102-104]. The study by Holden, et alshows the stability of these interfaces is up to few weeks without degradation [105].

1.2.3 Polymer-based Membranes

Similar to amphiphilic phospholipids, biomimetic membranes comprised of polymers permit scientists to study a wide variety of processes that occur at or across cellular membranes. However, due to the fragility and short lifetimes (minutes to days) of phospholipid bilayers [106], scientists have aimed to create more robust membranes using polymer species, including phospholipids [107-111] or polymers [109, 112-115], and they have also looked to un-polymerized block copolymers [116-121] that mimic the structure and amphiphilicity of lipids found in cellular membranes. Like lipids, amphiphilic block copolymers are known to self-assemble spontaneously into planar membranes, spherical vesicles called

polymersomes, or rod-like structures in water [122-124], and yet they exhibit greater mechanical and chemical stability than lipids [119, 120, 125].

A great advantage of copolymer is that they can be synthesized with desired size, chemistry and structure. In addition to a class of molecules called Janus dendrimers [124], diblock and triblock copolymers are the most commonly used types of amphiphilic polymers used to assemble biomimetic membranes. Diblock copolymers (i.e. those with an AB organization) consist of one hydrophilic polymer group attached to a hydrophobic group. With this architecture, diblock copolymers such as poly (ethylene oxide)-b-poly(ethylene ethylene) assemble to form 2-leaflet bilayer membranes in water, similar to the organization of phospholipids into bilayers [122]. The triblock architecture (i.e. ABA or ABC) usually consists of two end groups that are hydrophilic and a middle group that is hydrophobic. Therefore, unlike diblocks, triblock molecules can span the full thickness of the membrane they create [118, 126].

In recent years, several groups have used a specific ABA-format triblock copolymer consisting of hydrophilic poly (methyloxazoline) (PMOXA) end blocks and a hydrophobic poly(dimethyl siloxane) (PDMS) middle block [115, 117-119, 121]. Notably, PMOXA-b-PDMS-b-PMOXA membranes exhibit greater stability than lipid membranes [121] and they still retain the ability to reconstitute functional protein channels and pores [117, 121, 127] due to the elastic, fluid nature of the PDMS block that permits the hydrophobic interior to accommodate transmembrane proteins of varying lengths [126, 128].

Planar freestanding copolymer membranes can be formed by painting a mixture of copolymer and organic solvent across the aperture of a solid support in water [117, 118] via the methods pioneered for forming black lipid membranes (BLMs) [129-131]. As we previously mentioned this approach enables the assembly of a functional planar membrane, significant skill and time is required to initiate membrane formation and this approach yields only one membrane per experiment. In contrast, droplet interface bilayers DIBs are planar bilayer membranes formed at the interface of lipid-coated water droplets immersed in oil [51, 132, 133]. Thus, the ability to construct durable block copolymer-based membranes using the DIB approach could be used to develop new types of robust, compartmentalized materials for hair cell sensing, actuation, and energy harvesting. However, DIBs to-date have only been formed with phospholipids [134] or single-tailed amphiphilic surfactants [135], for which it is known that the structures and sizes of these surfactant molecules play important roles in adhesion properties of the membranes formed between droplets [136-139].

1.2.4 Electrical Characteristics of Synthetic Membranes

This part of the literature survey is intended to describe what is known about the electrical properties of synthetic cell membranes. This information is especially important because of the potential use of the membranes as sensing elements with electrical output.

In electrical terms, the plain (i.e. without protein) lipid membrane barrier is modeled as a capacitor parallel to a resistor [64, 140-142] as Figure 5a. As NaCl

molecules are dissolved in the droplets, the droplets become conductive and the membrane is placed in an electrical circuit [143]. Figure 5a shows the electrical circuit configurations for a droplet interface bilayer where R_b is the membrane resistance, C_b is the membrane capacitance, and R_s is the resistance of the conductive droplets. The bilayer resistance is about 10GΩ whereas the salt water solution has a resistance range of only 1-10KΩ [141, 144, 145]. The impedance of the circuit from point A to B can be written as

$$Z_{AB}(\omega) = \frac{R_b}{1 + jR_bC_b} + R_s \qquad \textbf{Equation 2}$$

When the total impendence of the resistive terms (i.e., R_b, R_s and $C_{b)}$ are plotted versus the frequency, three regions can be seen, as shown in Figure 5b [2, 146]. As the current flows through the minimum resistance in the parallel circuit and is

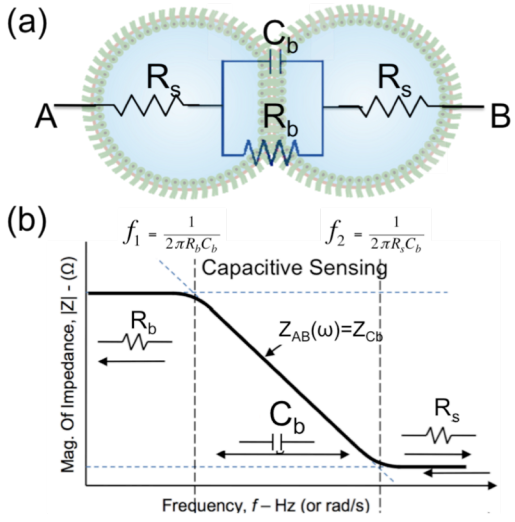

Figure 5: (a) The electrical circuit of of the connected droplets via bilayer. (b) Impedence of the circuit and the dominant circuit behavior based on Equation 1 [2] .

limited by the highest resistance in the series, the following pattern emerges: at low frequency (ω), the impedance of the circuit is approximately equal to the membrane resistance (R_b) (i.e., $Z_{AB} \approx R_b$) while at very high frequency, the impedance of the circuit acts as solution resistance (R_s) (i.e., $Z_{AB} \approx R_s$) because the membrane cannot respond quickly enough to the frequent voltage changes. However, at intermediate frequencies, the circuit acts as a membrane capacitance; that is, the total impedance of the circuit becomes dependent on the frequency of the voltage applied across the membrane. As the current takes the lowest resistance path—in this intermediate region only—the membrane acts as a capacitor, and the tails of the lipid molecules between the two droplets form a dielectric of the capacitor. Therefore, if the voltage frequency can be applied exclusively within this range, the membrane can act as a pure capacitor. In other words, if the input into the circuit can be controlled so that it remains in this range of frequency, the bilayer can function as a capacitor.

The electrical capacitance of a membrane is a function of the area and thickness of the bilayer. The hydrophobic tail molecules act as dielectric of membrane capacitor. The capacitance of the lipid bilayer is measured in real time. The current for the membrane capacitor can be written as

$$I = C\frac{dV}{dt} + V\frac{dC}{dt} \qquad \textbf{Equation 3}$$

where C is the capacitance of the membrane, I is the current flowing through the capacitor, and dV/dt is the time rate change of applied voltage. Through this

relationship and the known input-voltage and measured current, the value of the capacitance of the membrane can be computed based off the measured square wave current. In this process, reversible Ag/AgCl electrodes are used to apply voltage and measure the output current across the membrane. Triangular wave voltage is applied across the membrane, and the square wave current response, representing the capacitance, confirms the existence of the bilayer.

In a physical terms, due to hydrophobic effect and Vander Waals force between hydrophobic chains, as the droplets come into contact with each other and excess oil is extracted from the space between the bilayers [147, 148], the two monolayers on the surface of the droplets become thinner and thinner, forming a bilayer structure. As the bilayer thins, the capacitance of the membrane (i.e., the square wave current response) quickly increases. The capacitance of the membrane can be computed at any moment in the process—before, during or after the full formation of the membranes. In all of our tests, the lipid bilayer was held in a polymeric flexible substrate [56] and was formed between lipid-encased volumes under oil [149]. A regulated attachment technique was used to control the size of the bilayer (i.e., the area of capacitance) formed between the two neighboring droplets [56]. Using electrical measurements, we were able to characterize the capacitance, area, as well as the resistance of the membrane formed between the droplets as it has been described previously [56, 150].

After the formation of the membrane is confirmed by capacitance measurement, cyclic voltammetry is used to characterize the resistance, the sensing capabilities

of lipid bilayer and any failures of the bilayer due to electrical fields or mechanical perturbations. With this method, it is possible to characterize any voltage dependent behavior of the system by applying the voltage across the membrane and measuring the output current. In this technique, which has been applied quite often in this dissertation, the voltage is increased in regular steps up to desired sensing-required voltage.

1.2.5 Lipid Bilayer Mechanoelectrical Transduction

Deformable and capacitive nature of membranes and the fact that membrane's capacitance can be affected by physical stimuli, allows these allows these structures to be used as a sensor [3, 6]. However, change in the capacitance of the membrane that is associated with the vibration of the lipid bilayer can have a

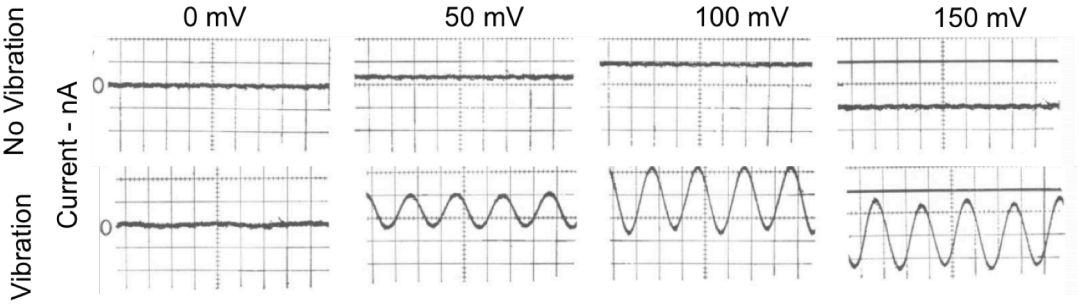

Figure 6: Voltage clamp experiment. From left to right, the membrane was clamped at: 0 V, 50 mV, 100 mV, and -100 mV. In these experiments the shutter was held open for 10 sweeps after the membrane capacitance became charged. The trace was synchronized to the 50 cycle oscillator in both series A and B. The vibration amplitude was 1.75 μm peak to peak, measured at the connecting rod. The membrane was planar. The temperature was 300C (Reproduced with permission from [6]).

number of causes: 1) a change in the thickness of interface, 2) a change in the dielectric constant, or 3) a change in the area of the membrane, the previous research has confirmed that the primary reason for changes in membrane capacitance due to vibration is a change in the area of the membrane [6, 151]. Particularly, previous research has shown that the thickness of the membrane does not change as the membrane curves by electrical characterization of lipid bilayer [6, 151].

The time rate change of the capacitance of the membrane due to vibration produces output-current signals at an applied voltage. The frequency of the current generated by the membrane is correlated to the frequency of the input mechanical oscillations [6]. As the membrane is vibrated at a known frequency, its area increases and decreases, and the output and input frequencies are equal for rounded membranes (i.e., the non-flat interface) [6], whereas the input frequency doubles in measured current when the membrane is planar [6]. In Figure 6 Ochs et al. show the results at the point where the membrane is directly vibrated at a constant frequency. We can see that when there is no vibration, the current output in a voltage clamp mode is very stable, whereas when the membrane is vibrated under a specific constant voltage applied (>0mV), a current is generated. Note that, given a constant rate of perturbation stimuli, the amount of current that is generated increases with increasing voltage. This voltage-dependent transduction has been shown to be the result of a time-rate change of capacitance in the membrane [6]:

$$I_{Vibration} = \frac{dQ}{dt} = V\frac{dC}{dt} \qquad \textbf{Equation 4}$$

Note that the membrane type in this case is specifically a painted membrane [85, 152] and that these membranes are formed in a different way than DIBs.

1.2.6 Hair Cell Inspired Sensor Technologies

The hair cell structures and arrays found in nature have inspired the development of various kinds of engineered devices in the recent years. All of these bio-inspired designs employ artificial hair structures for mechanical sensing or actuation. Examples include an airflow velocity sensor [35, 36], an oscillating flow sensor [37], a magnetostrictive force sensor [5], a microparticle actuator [38], and an underwater directional flow sensor [36, 39, 40] (some of these examples are shown in Figure 7). One of the main differences between these human-made designs and natural hair cells is the use of engineered transducers (i.e., cantilever beams and solid materials) in place of biomolecules to perform transduction.

Motivated to implement a biomolecular hair cell sensor, Sarles and Leo combined the phospholipid self-assembly phenomena with soft materials to create a mechanoelectrical transducer whose sensing element is an artificial cell membrane, or lipid bilayer [4]. This membrane-based hair cell is responsive to mechanical perturbations of a hair, which induce oscillations in the bilayer, which produce a measurable current due to the time rate of change of the electrical

capacitance of the vibrated membrane [4]. This transduction process has been confirmed/tested by observing that the sensing current is proportional to the voltage applied across the lipid bilayer membrane [4]. In this initial hair cell sensor, the perturbation of the hair by means of airflow leads to a time rate change in the capacitance of the membrane, resulting in measured currents on the order of less than 100pA [4].

Although the Sarles embodiment of hair cell sensors produced a sufficient time rate of change in capacitance and thus a measurable signal for exploring bilayer-based transduction via hair motion, the sensor exhibits a number of limitations. These limitations include low mechanical stability of the hair that was supported only by a small hydrogel volume, poor membrane durability due to excessive hair motion, low sensitivity or signal-to-noise ratios, and the lack of any flow directional response. My initial aim in graduate was to revise the sensor design and fabrication methods to establish a well-supported hair cell structure in which

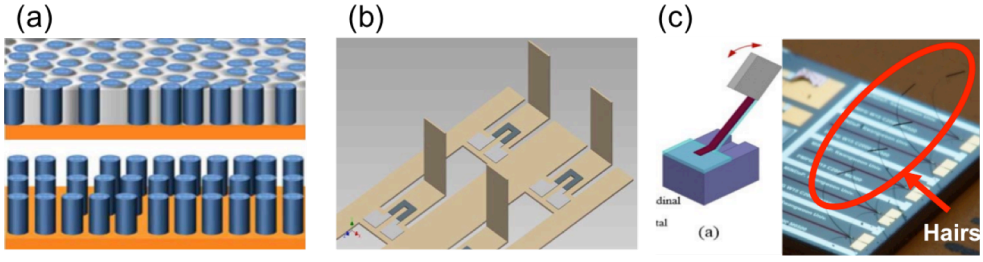

Figure 7: (a) Bio-inspired inorganic nanocilia sensors using magnetic materials [5], (b) Paper-Based MEMS Hair Cell Array using piezoelectric materials [7] and (c) Hair-cell structure based piezoelectric energy harvester operating under three dimensional arbitrary vibrations [8]

the hair would have improved stability and the bilayer would have greater durability, as well as an increased operating range.

Achieving a more durable embodiment would make it possible to achieve our second aim---to thoroughly investigate and characterize the directionality and sensitivity of the hair cell device. Also with more durable sensors and better understanding of the sensing mechanism and operational limits of a single-bilayer, single-hair sensor, arrays can be constructed in such a way that the sensing functionality can be increased. Such arrays of natural hair cells are common in organisms and are known to provide sensing robustness, sensitivity, frequency selectivity, directionality, and spatial awareness [153-156].

1.3 Scientific Gaps

We define the following scientific gaps:

1. A durable and robust membrane-based hair cell embodiment is needed to more fully characterize the sensitivity, directionality, and frequency characteristics of membrane-based hair cell sensors.
2. DIBs allow the formation of multi-membrane arrays, but there is no knowledge of how vibration propagates across multiple droplets and membranes, or how membranes positioned farther from a vibrating hair respond to mechanical perturbation.
3. The assembly or mechanotransduction responses of DIBs formed with amphiphilic polymers instead of lipids has not been performed, thus it is

unknown how the tradeoff between membrane thickness for durability and reduced capacitance affects the sensing output.

4. The prior study of a membrane-based hair cell only included a model for the current-voltage relationship in the membrane, which provided evidence that changes in capacitance due to membrane bending generated current. However, it did not include theory to relate a perturbation to resulting hair motion and then membrane deformation that produces the current. Thus, the lack of a complete mechanotransduction model for this type of assembly limits our understanding of the physical processes and parameters that dictate the sensing response of a membrane-based hair cell sensor.

1.4 Objectives and Contributions

To address the scientific gaps, the objectives of this dissertation are:

1. Develop a more robust hair cell embodiment, and thoroughly characterize membrane-based mechanotransduction, including sensitivity, directionality, and the frequency response of the membrane, in response to airflow and hair flicking.
2. Assemble and experimentally characterize the mechanotransduction responses of each membrane in a multi-membrane droplet array. The specific goals are to: a) understand how multiple membranes respond to the motion of one or more hairs in the array, b) assess the propagation of

vibration in a droplet array by determining how many membranes away from a moving hair yield a sensing current, c) characterize the relative timing of sensing responses of each membrane relative to hair motion, and d) explore how multiple membranes respond to perturbations of multiple hairs in the array.

3. Examine the role of polymer structure and oil selection on the assembly and physical properties of polymer-based membranes formed between droplets, and compare the mechanotransduction responses of polymer-based DIBs to those formed using lipids.

4. Develop a model that captures the entire transduction process to understand the key physical parameters or design variables for the sensing response. This model combines Helfrich theory of membrane deformation and Stokes theory of pendulums moving in fluids to understand how parameters like hair length, membrane stiffness, and membrane capacitance affect the sensing current in response to airflow [2].

CHAPTER 2: METHODS OF ASSEMBLIES AND MEASUREMENT TECHNIQUES

Membrane based systems are constructed using different techniques for characterization of hair cell sensors and membrane properties for lipid and polymer membranessuch as sensing characteristics, specific capacitance, thickness, electrowetting, and monolayer and membrane tensions.

Electrical and optical techniques are used for characterizing intra-droplet interfaces. The electrical characterization techniques are used to validate the formation, measure the electrical properties of membranes such as capacitance, resistance and hair cell sensing responses, while optical measurements are used to estimate the contact angle and area of membranes in some cases. We also discuss different methods that are used as perturbations methods = for characterization of hair cell sensors in our studies.

In this chapter we will discuss all the general techniques that are used throughout my PhD dissertation. Each of these techniques provides a unique platform to precisely study and understand the characteristics of lipid and polymer intra-droplet membranes.

2.1 Experimental Setup for Droplet-Based Membrane Formation

2.1.1 Droplet Interface Bilayer Formation

Droplet interface bilayer (DIB) is formed between two lipid-encased droplets covered in oil. Each droplet contains salt solution containing ions of a sodium chloride (NaCl) and also contains phospholipid vesicles (DPhPC). For electrical measurement across each DIB, conductive electrodes used in this system extend through the oil phase and pierce into the aqueous inner of each droplets. Amphiphilic, phospholipid molecules combined with the water phase result in the assembly of a lipid single monolayer at the oil-water interface surrounding each droplet (Figure 8a) [51]. Waiting time for monolayer formation has been 3-5 minutes. A liquid-supported interface bilayer is formed when the separated droplets come into contact (Figure 8b).

Bilayer thinning occurs as additional oil is first exited from between the two droplets and the monolayers “zip” together due to van der Waals attractive forces in between hydrophobic tails (Figure 8c) [51]. The droplet interface bilayer is a method for creating durable, liquid-supporting lipid bilayers at the interface of connected, lipid-encased aqueous droplets submersed in oil. Self-assembly processes initiate the formation of a lipid monolayer at each oil-water interface, enabling bilayer formation upon contact of droplets. Piercing electrodes are used for electrical characterization of the interface. The electrode-electrolyte solution

interface for each electrode is electrically modeled as a resistor, in parallel with a capacitor (Figure 8d and e). The aqueous electrolyte solution within each droplet contributes to the circuit a series resistance, R_s. A lipid bilayer provides a electrical seal between the droplets (high resistance), thus the interface is modeled as pure capacitor. The conductive pathway existing between electrodes positioned in separate droplets. Since bilayers have high but finite resistance values so both resistive and capacitive terms are used to describe the electrical characteristics of interface formed between two droplets (Figure 8e). Similarly, the resistance of the electrolyte solution and the electrode-electrolyte interface components are extremely low to compare with the bilayer resistance therefore they can be neglected in this series resistors. The use of reversible electrodes by

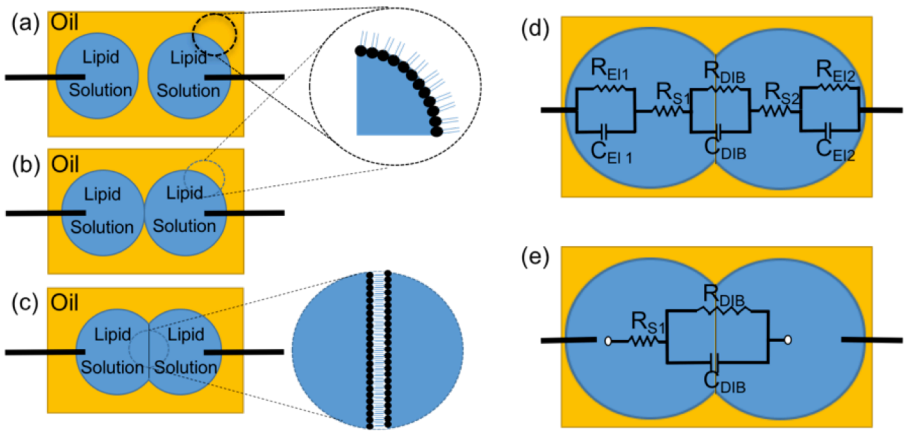

Figure 8: Droplet interface bilayer formation (a) lipid encased droplets are placed under the oil phase for monolayer formation, (b) monolayer formed on the water-oil interface and droplet are brought into contact, (c) the monolayers are “zipped” together and formed bilayer between droplets, (d) electrical configuration model of connected droplet through a conductive droplets, and (e) simplify electrical model of two connected droplets via membrane.

silver-silver chloride helps efficient ion exchange and prevents electrical capacitive double layers from forming at the surface of the electrodes. In Figure 8e, the two series resistances for each electrolyte solution are combined to get an equivalent resistance. With these simplifications, the complete circuit model condenses to the form shown in Figure 8e, thus only the intra-droplet interface and the electrolyte solutions affect the flow of ions.

2.1.2 PDMS Substrate Fabrication

The substrates that are used to support liquid droplets and oils are made of Polydimethylsiloxane (PDMS) [56]. The hydrophobic templates are flexible and elastic. Below are the steps for making PDMS substrate for different experiments:

1. The features that define the droplet compartments and aperture dimensions of the substrate are first machined into an acrylic (PMMA) substrate using a vertical end-mill.
2. Uncured Polyurethen (PU) (2:1 wt-wt ratio of base to curing agent) is poured into the acrylic substrate and crosslinked at 70° for two hours on a hot-plate in order to create the geometrical negative of the original high-packing factor acrylic substrate.
3. The cured PU is soaked in uncured Sylgard 184 (Dow-Corning) PDMS (10:1 wt-wt ratio of base to curing agent). Then again this part is placed on a hot-plate at 70° for two hours.

4. Then using spatula we take the cured PDMS out and our substrate is ready to use. The PU negative template can be reused to make more PDMS substrates.

The final substrate contains compartments (1.02mm in diameter and 1.52mm deep, with hemispherical bottom surfaces) are separated by about 500μm-wide by 1.2mm-tall aperture that spans the window formed between the circular compartments. Then silver-silver chloride (Ag/AgCl) electrodes made from 125μm-thick silver wire (Goodfellow) are then pierced through the sides of the PDMS substrate such that the tip of each electrode is positioned approximately in the center of a compartment and into each droplet (Figure 9). The flexibility of the substrate allow us to be able to control the contact and DIB size plus in case of colescence we are able to divide (Figure 9a) the droplets to two separate droplets (Regulated Attachment Technique [56]) and reform the membrane

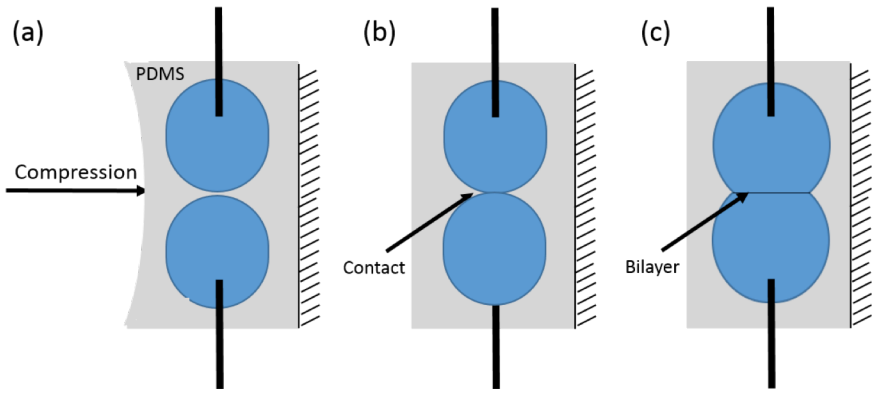

Figure 9: Regulated Attachment Method: (a) droplets are separated by compressing the flexible cubstrate, (b) droplets are brought to contanct and (c) the membrane is formed between the two droplets as they brought into contact.

between droplets (Figure 9b,c). Hair cell embodiments in our work utilized regulated attachment method to control the amount of contact and the area of the membrane formed between droplets.

2.1.3 Suspended Droplet Technique

To characterize monolayers and membrane surface tension, we needed to clearly measure the contact angle as voltage is applied across the membrane. Therefore we used suspended droplets under the oil hanging by the electrodes and measuring the contact angle by inverted microscope through the clear substrate [157]. In this method interfaces are formed between two aqueous droplets suspended under the oil-filled reservoir of a transparent PDMS substrate. As shown in Figure 10 aqueous droplets of 200 nL are pipetted onto electrodes made from 50 μm silver-silver chloride wire (Sigma). Suspended

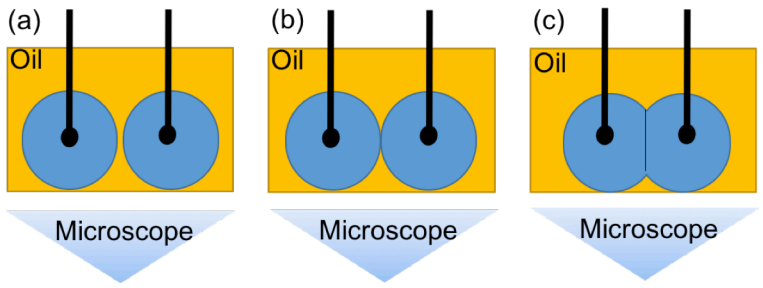

Figure 10: Suspended droplet technique: (a) droplets are pippeted into the oil phase and each electrode pierce in one droplet, (b) after formation of monolayer the droplets are moved via electrodes and dropght into contact and (c) the membrane is formed between droplets. The inverted scope enabled us to estimate to measure the diameter of the circular membrane and therefore the area of membrane formed between droplets.

droplets electrode tips under oil (in some cases the electrodes coated with hydrogels to be able to hold the droplets).

Injecting a small volume of oil between the substrate and the inverted microscope slide develops the clarity of PDMS substrate. Each electrode is attached to a 3-axis micromanipulator (World Precision Instruments, Kite-L and Kite-R models) to bring the droplets in contact (Figure 10b) let the control over the position of each droplet. Figure 10 shows the schematics of the suspended droplets.

To persuade electrowetting between droplets, custom dc step voltage routines are used in defined increments. Images of droplets and interfaces are taken from below through the 4X objective lens of an Olympus IX50 inverted microscope are acquired with a QI Click CCD camera controlled using Q-capture software. Intradroplet interface images are post-processed using ImageJ software to extract contact angles for measurements of tensions and free energies.

2.1.4 Droplet on Hydrogel Bilayers

Due to extremely low tension of our droplets when copolymer is used as surfactant under good solvent, the droplets do not form a spherical shape under the oil. Therefore it makes the area measurement inaccurate by using the side-by-side droplets (in case of spherical droplets, the contact can be measured as the diameter of interface). Therefore we used droplet on hydrogel technique and

formed the membrane between droplets on top of hydrophilic hydrogel layer as shown in Figure 11. In this technique the clear-bottom and flat PDMS substrate is used on a glass slide on top of inverted microscope [158]. First the bottom of the substrate is filled with low-temp agarose (Sigma) 5%w/v liquid and cured as shown in Figure 11. Then electrode is inserted into the hydrogel surface. Then an aqueous droplet of 200 nL is pipetted onto the hydrogel-coated electrode made from 50 μm silver-silver chloride wire (Sigma).

In all of the droplet on hydrogel measurements, we used the polymeric surfactant in oil. After the droplet is held under the oil for the monolayer self-assembly, the droplet is brought into contact with gel surface and the interface is formed between the droplet and hydrogel Figure 11c upon application of voltage (will be discussed in chapter 5). In this technique the electrical measurement is used to

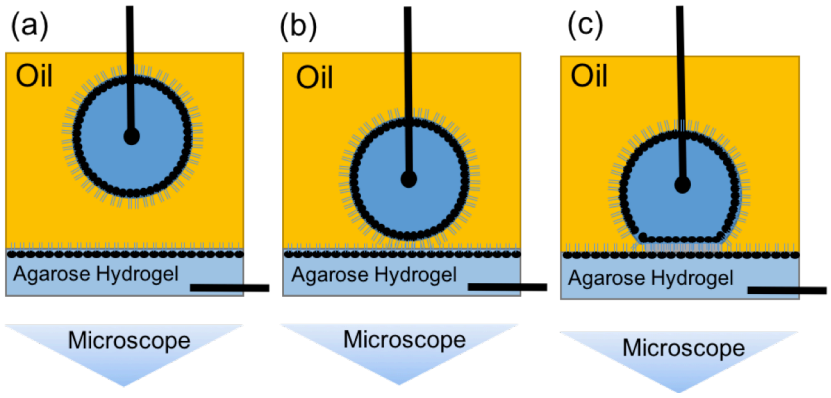

Figure 11: Droplet on hydrogel techniques: (a) the droplet is held on under the oil above the hydrogel layer for monolayer formation and one electrode is inserted to the hydrogel and one holding the droplet, (b) after the monolayer self-assembly on water-oil and hydrogel-oil interface, the drpolet is broght into contact with the hydrogel, and (c) the membrane forms between the hydrogel layer and the droplet.

capture the capacitance of the membrane and optical measurement is used to capture the area of the membrane. To persuade electrowetting between the droplet and hydrogel dc step voltage are used (Figure 11). Images of droplets and interfaces are taken from below through the 4X objective lens of an Olympus IX50 inverted microscope are acquired with a QI Click CCD camera controlled using Q-capture software. Intradroplet interface images are post-processed using ImageJ software to extract contact angles for measurements of tensions and free energies.

2.1.5 Bilayer Formation between Spherical Hydrogels Volumes

In this section we show the method of formation of interfacial lipid bilayer between lipid-encased aqueous volumes (PEG-lipid mixture) contained in the neighboring compartments of the PDMS substrate. Positioning and attachment of the lipid-coated volumes in the substrate is performed via the regulated attachment method discussed before [56]. Reducing compression on the substrate to open the dividing aperture between compartments allows the droplets to come into contact, after which a lipid bilayer spontaneously forms at the interface of the two lipid-encased volumes. The final area of the bilayer is controlled by adjusting the width of the aperture between compartments via lateral compression of the substrate using a manual micromanipulator (KITE-R, World Precision Instruments). Following membrane assembly, PEG-lipid volumes are photopolymerized under ultraviolet (UV) light for 9 minutes using a LED-200 (Figure 12d) portable light (Electro-Lite Corp) with a power output of 2.5 W/cm^2 at

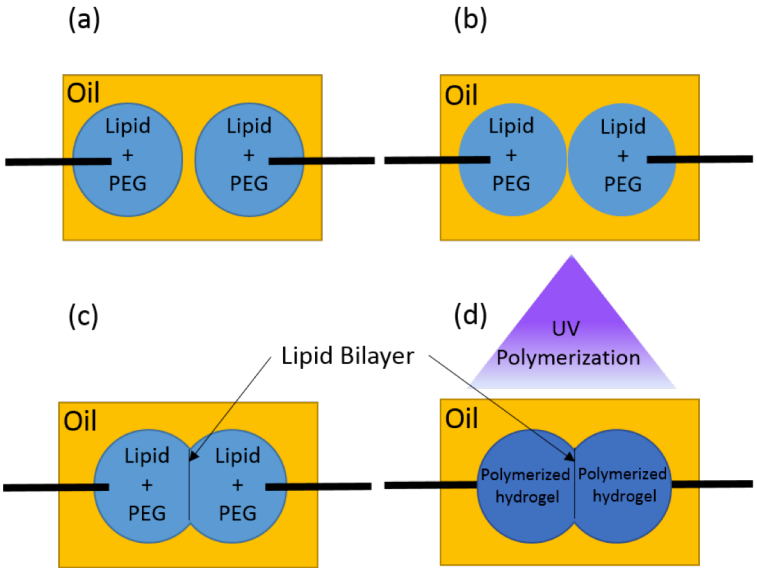

Figure 12: Forming membrane between two spherical hydrogel volume (a) PEG-Lipid solution are placed under the oil for monolayer formation, (b) after monolayer formation the PEG-Lipid encased droplets are brought into contact, (c) membrane is formed between droplets, (d) the PEG-lipid encased droplets are polymerized using the UV light.

365nm. Electrical measurements confirm that the bilayer remains stable during photopolymerization of gel volumes [159]. The schematic of this process can be seen in Figure 12.

2.1.6 Copolymer Stabilized Interfaces

Copolymer-stabilized droplet interfaces are created between adjacent 200nL droplets of aqueous buffer placed in a copolymer-oil mixture, or using the droplet-on-hydrogel bilayer method [160-162] for forming a gel-supported CSI (using techniques discussed in 2.1.4 and 2.1.5). For each oil type, PEO-PDMS-PEO triblock is incorporated into the oil at a concentration of 4 mg/ml, vortexed, and then stirred on a magnetic hot plate at a temperature of >60°C to facilitate

complete dissolution of the polymer. The application of heat ensures that the PEO end-blocks remain above their transition temperature (~30°C), as evidenced by obtaining a clear, homogeneous polymer-oil mixture. Aqueous buffer used in CSI and DIB experiments is 100mM NaCl, 10mM MOPS, balanced to pH 7.4 via titration with an identical solution supplemented with 0.5M NaOH. Buffer pH is verified using a Fisher Scientific Accumet pH probe. Aqueous buffer and polymer-oil solutions are stored at room temperature (23°C), and polymer-oil solutions are reheated before tests to ensure complete dispersion of polymer in the oil phase.

2.2 Electrical Measurement Characterization of Membrane

Electrical measurements are used as main characterization technique during my PhD studies. Electrical measurements are utilized to characterize membrane capacitance, area, sensitivity, specific capacitance and thickness as well as membrane tension. In this section, I briefly explain the common electrical techniques used in next few chapters.

2.2.1 Capacitance Measurements

During interface formation, current measurements are performed using an AxoPatch200B patch clamp amplifier, Digidata 1440A data acquisition system (Molecular Devices) and Tecella Triton 8 to measure the resulting capacitive square-wave current induced by an externally generated known frequency and amplitude triangular voltage waveform. The triangle wave voltage is generated

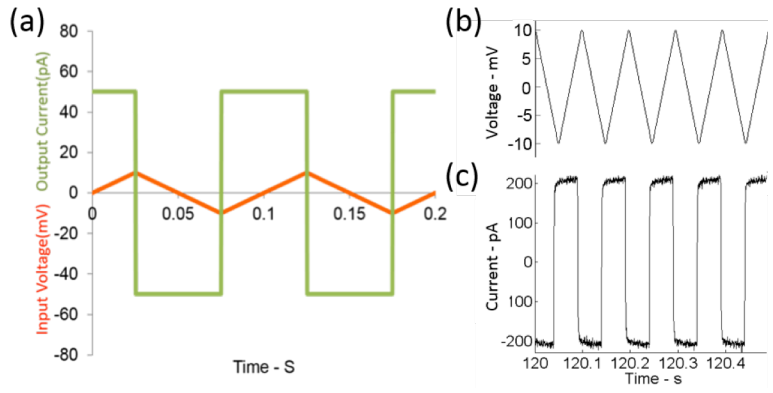

Figure 13: Red is the schematic of triangular wave applied across the membrane and Green is the square wave capacitive current response.

using an Agilent 33210A function generator and Tecella Trion 8 (for array of connected droplets). Capacitance measurements are performed using an AxoPatch200B and Digidata 1440A (Molecular Devices) to measure the resulting square-wave current (sampled at 20kHz, and low-pass filtered at 2kHz) induced by an externally generated, 10mV triangular voltage waveform at 10Hz (the output of a Agilent 33210A function generator) shown in Figure 13. Figure 13a show the schematic of applied voltage (red) and square-wave response current (green). A recorded applied voltage (Figure 13b) and capacitive squarewave current is shown in Figure 13c. The capacitance of the membrane is calculated from these square waves; based on specific capacitance value of a given membranes, the area of membrane is extracted ($A=C/C_s$).

From the resulting squared signals, we approximate the capacitance of membranes, by dividing the measured current by the time rate of change of the applied voltage

$$\frac{I}{C} = \frac{dV}{dt} = 4A.f \qquad \textbf{Equation 5}$$

for 10mV applied triangular voltage amplitude, A, and 10Hz frequency. Therefore tha capacitance will be calculated by:

$$C = \frac{I}{4Af} \qquad \textbf{Equation 6}$$

2.2.2 Sensing Measurement

The sensing response of the revised hair cell is characterized using three forms of mechanical perturbation to the hair. In the first case, a horizontal steady airflow exiting a 0.61 mm inner diameter needle tube at a distance 4-5 mm from the hair is applied at varying flow velocities to perturb the hair Figure 14a. A tank of compressed nitrogen is used as the source for airflow, and pressure is controlled with a two-stage regulator. Pneumatic tubing and push-to-connect fittings are used to connect the tank to the needle fixture. Flow velocities ranging from 3-20 m/s at the hair location are calibrated to the regulated pressure using an anemometer (Multi-Function Instruments, Model: TA 465). Second, an automated flicker consisting of a servomotor and rotating plastic wand is used to induce free vibration of the hair by bending and releasing the hair as the wand rotates. The flicker impacts the hair at a distance of 1-2 mm from the free end (top).

Third, a mechanical shaker (PASCO, SF-9324) is connected to an aluminum rod that attaches to the hair using beeswax to shake the hair at a known frequency.

RMS values of the measured current versus applied voltage for 6 different flow speeds from ~4-18m/s (Figure 14b shows the response of hair cell sensor to 3.7 m/s airflow). In all measurements, the areas of the bilayers were held constant at ca. 0.042mm2 at every voltage level by using the regulated attachment technique [17] to return the bilayer area to its zero-voltage value. This correction was applied to eliminate changes in area of the bilayer due to the electrowetting effect (i.e. α=0) [1]. Then the RMS current versus voltage for the various airflow speeds

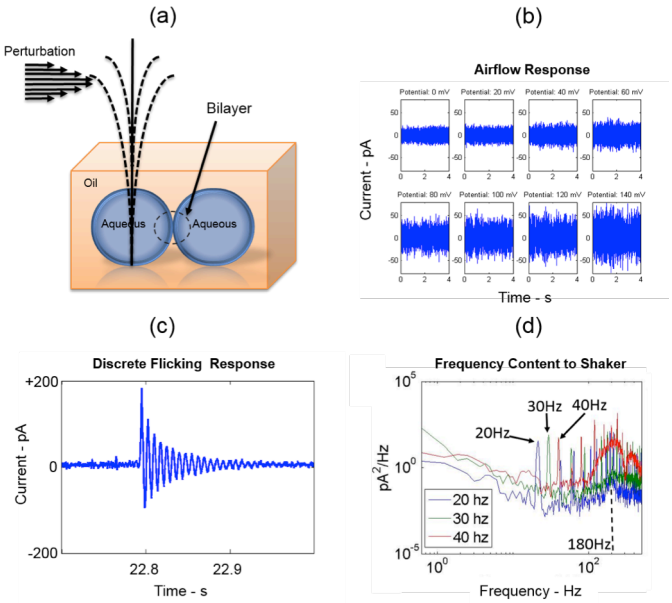

Figure 14: (a) Schematic of single membrane haircell assembly and (b) the sensing response of hair cell sensor to airflow as voltage applied across the capacitive interface, (c) the sensing response of hair cell sensor to discrete flicking, and (d) the PSD of current responded at low frequencies (frequencies lower that natural frequency of the hair), using mechanical shakers.

are measured and computed, where the slope of each current-voltage series represents the time rate of change of membrane capacitance, dC/dt, at each airflow speed.

Figure 14c shows a second-order underdamped current response of a single flick to the hair. We compute the total charge displaced across the membrane during hair vibration as the area under the current, versus time trace.

We also characterized the membrane response to stimuli at frequencies lower than the hair's resonance. In this set of tests, we used a mechanical shaker to vibrate the hair perpendicularly to the plane of the membrane (90°) at 20, 30, and 40Hz. The power spectral densities of the current responses at the three oscillation frequencies at 60mV are shown in Figure 14d, where the arrows indicate the first peak frequencies for the three current traces.

Sensing current generated by the lipid bilayer is low-pass filtered at 2kHz and sampled at 20kHz using the AxoPatch200B and Digidata 1440A with data analysis performed using MATLAB. A power spectral density (PSD) using Welch's method of the current response is performed to determine the average power as a function of frequency for the measured signal as shown in Figure 14d . Additionally, a FASTCAM 1024 PCI high-speed camera is used to track the motion of the tip of the hair during free vibration after flicking. The camera is positioned above the sensor and captures hair motion from a top view at 6000 frames per second. Images are saved in ".tiff" format. The tip position of the hair is projected on a 2D plane for plotting, and the frequency of the hair oscillation is

obtained from tip position versus time data by calculating the power spectral density (PSD) in MATLAB.

CHAPTER 3: FABRICATION AND CHARACTERIZATION OF DURABLE INTRA-DROPLET MEMBRANE-BASED HAIR CELL SENSORS

3.1 Overview

As discussed in chapter 1, the artificial cell membrane can be used as mechanoelectrical transducers. We introduced the first generation of the membrane based hair cell sensors and showed that it exhibits a number of limitations such as low mechanical stability of the hair that was supported only by a small hydrogel volume, poor membrane durability due to excessive hair motion, low sensitivity or signal-to-noise ratios, and the lack of any flow directional response [3]. In this work [1], we develop and characterize a durable and robust hair cell sensor allowing large, and repeated deformations of the hair without rupturing the membranes. Due to greater robustness, we were able to fully characterize the mechanoelectrical transduction process of a membrane-based hair cell sensor both with discrete and continuous perturbations.

3.2 Introduction

Motivated to construct a biomolecular hair cell sensors, Sarles and Leo combined phospholipid self-assembly methods with soft materials to create a transducer whose sensing element is an artificial cell membrane, or lipid bilayer (Figure 15a) [4]. This membrane-based hair cell is responsive to mechanical perturbation of a

[1] Note: This chapter presents findings reported in a recent journal paper published in Smart Materials and Structures – IOP Science entitled, “Sensitivity and directionality of lipid bilayer mechanotransduction studied using a revised, highly durable membrane-based hair cell sensor”.

hair that induces oscillation in the bilayer, which generates a measurable current due to the time rate of change of electrical capacitance of the vibrating membrane [4]. This transduction process was verified by observing that the sensing current is proportional to the voltage applied across the lipid bilayer membrane [4]. The initial hair cell sensor mechanotransduction model is:

$$i = \frac{dC}{dt}(V + \alpha V^3) \qquad \textbf{Equation 7}$$

where *α* is the electrowetting constant for the two monolayers that comprise the membrane and *dC/dt* is the time rate of change of bilayer capacitance induced by mechanical perturbation of the hair. In that study, perturbation of the hair with airflow resulted in measured currents on the order of 10-100pA [4].

Although the first embodiment produced a sufficient time rate of change in capacitance and thus a measurable signal for exploring bilayer-based transduction of hair motion, the sensor exhibited several limitations. These include low mechanical stability of the hair that was supported only by a small hydrogel volume, poor membrane durability due to excessive hair motion, low sensitivity, and undefined directionality. The goal in our current work is to revise the sensor design and fabrication methods to establish a well-supported hair cell structure with improved stability of the hair and greater bilayer durability, as well as an increased operating range. In addition, we are motivated to achieve a more durable embodiment to be able to thoroughly investigate and characterize the directionality and sensitivity of the device. With more durable sensors and better

understanding of the sensing mechanism and operational limits, we aim to construct arrays for providing distributed sensing and increased directionality. Such arrays of natural hair cells are common in organisms and are known to provide sensing robustness, sensitivity, frequency selectivity, directionality, and spatial awareness [153-156].

In this chapter, we present and characterize a revised version of the membrane-based hair cell sensor that utilizes a cantilevered hair, rooted at its base within the polymeric encapsulating substrate. It is shown that this adjustment yields significantly greater mechanical stability for the hair structure and increased bilayer durability by preventing the hair from falling over and rupturing the bilayer. Similar to the previous effort [4], the hair passes through one of two lipid-coated aqueous volumes submerged in oil; the phospholipid-coated volumes connect to form a 5nm thick unilamellar membrane lipid bilayer.

Oscillation of the hair transmits energy to the bilayer, resulting in a measurable current produced by the time rate of change of electrical capacitance of the vibrating membrane [4]. The first target of our study is to experimentally characterize the perturbation-induced current response of the lipid bilayer due to vibration of the modified hair support. Three types of perturbation are utilized to characterize the device: steady airflow, direct oscillation of the hair by a mechanical shaker, and periodic free displacement of the hair using an automated flicking device (Discussed in Chapter 2). Because of enhanced sensor durability, we also perform several experiments that add to our

understanding of the mechanotransduction process and sensing performance for a membrane-based hair cell sensor. Specifically, we measure the directional response of a membrane-based hair cell sensor for the first time, examine its response to low frequency excitation (below the first resonance frequency of the hair), and study the effects of using liquids versus gel materials for the aqueous volumes. Finally, we quantify the sensitivity, minimum sensing threshold, and the dynamic range of the sensor in response to airflow across the hair.

3.3 Materials and Methods

3.3.1 Fabrication of Hair Cell Sensor

The polymeric fiber (90-110μm diameter) used as the hair is obtained from a Prostroke 101B paintbrush. A hole for rooting the hair is created in the PDMS substrate in the center of one of the droplet compartments by piercing from the bottom with a 150μm diameter drill bit. The hair is then inserted through the pierced hole from the top (Figure 15b), such that it will pass through the center of one of the aqueous volumes. The hair can be inserted either before or after a droplet is dispensed into the compartment. We examined the effect of varying the depth of fixation in the substrate and found that deeper hair insertion leads to increased vibration of the substrate that results in greater background current due to the vibration of the electrodes when the hair is perturbed. Thus, the hair is inserted ca.1-2mm into the PDMS substrate. The remaining free length of the hair is 16-18mm, measured vertically from the bottom of the compartment to the tip of the hair. This configuration is used in all measurements performed; Figure

15c shows images of the sensor from top and isometric perspectives. Images of assembled hair cell sensors are obtained through the Leica M80 stereomicroscope using a Canon G12 digital camera.

3.3.2 Materials

Lipid bilayers are formed at the interface of lipid-coated aqueous volumes consisting of either an aqueous liposome suspension (liquid) or a mixture of liposomes and a photopolymerizable hydrophilic polymer (hydrogel) in aqueous buffer. Aqueous liposome solution containing 2mg/ml of 1,2-diphytanoyl-sn-glycero-3-phosphocholine (DPhPC, Avanti Polar Lipids, Inc.) liposomes in 200mM NaCl, 10mM, 4-Morpholinepropanesulfonic acid (MOPS), pH7 is prepared as described by Hwang, et al [163]. Difunctional poly(ethylene glycol) diacrylate (PEGDA, 6000g/mole, Sigma) was obtained and used without further purification. A stock PEGDA solution is prepared by dissolving PEGDA (20% w/v) and Irgacure 2959 (BASF) photoinitiator (0.1% w/v) into deionized water and the mixture is poured into a UV protected bottle at 4°C. The gel stock solution is stored at -20°C until needed when it is combined with the stock liposome solution at a 1:1 (v/v) ratio to yield a final gel-lipid mixture consisting of 10% (w/v) PEGDA, 0.05% (w/v) Irgacure 2959, and 1mg/ml DPhPC vesicles in 100mM NaCl, 5mM MOPS, pH 7. Hexadecane (Sigma, >99%) is used as the oil in all experiments.

3.4 Revised Embodiment of the Sensor

A schematic of the original membrane-based hair cell is shown in Figure 15a In the original version, the hair is rooted in a small volume (~1µl) of hydrogel that comprises one of the two lipid-coated aqueous volumes residing in the oil-filled substrate [4]. In practice, this method for supporting the hair and the aqueous droplets limits durability as intense stimuli causes the hair to fall over and rupture the bilayer. Membrane rupture is also possible if the supporting gel volume rotates within the compartment of the substrate. This variation of contact with the other droplet may also affect the directionality and reproducibility of the sensing response even if the membrane survives the gel's motion. Additionally, the volume of each droplet is different since one droplet is supplemented with gel and polymerized in a separate step before forming a bilayer. The dissimilar aqueous volumes (i.e. one solid and one liquid) can cause unbalanced energy transfer to the membrane from each side. Furthermore, inconsistent positioning

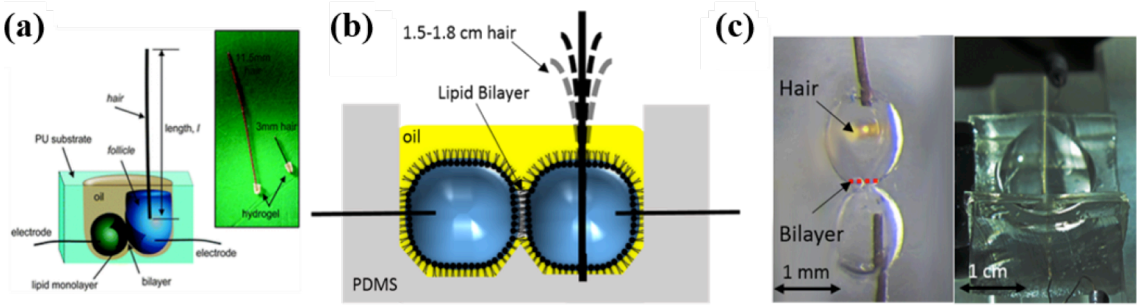

Figure 15: (a) Original hair cell sensor reprinted with permission [4]. (b) Schematic of revised hair cell embodiment (not to scale). (c) A top view (left) and isometric view (right) of the revised hair cell sensor.

of the hydrogel volume or hair within the compartment may also cause problems in maintaining contact with the wire-type electrodes needed to extract sensing current.

The revised hair cell sensor embodiment, shown schematically in Figure 15b and c, features a hair structure that is rooted into the polymeric substrate at the bottom of the droplet compartment for increased durability and mechanical stability. Similar to the previous work, the hair is made from a paintbrush fiber with diameter of 90-110μm. Inserting 1-2mm of the length of the hair into the substrate has multiple advantages: 1) the hair remains fixed in place even during high levels of mechanical perturbation; and 2) either hydrogel or liquid may be used to comprise the aqueous volume that surrounds the hair, since the substrate maintains the hair's orientation. The latter means that symmetric compositions of aqueous volumes can be chosen to construct the sensor, and the volumes are expected to maintain more consistent contact during perturbation because the position of the base of the hair remains fixed. However, this change in boundary conditions may also affect the characteristic frequency of vibration of the hair as well as the force transmissibility of hair motion to the lipid membrane.

One of the limitations of the first membrane-based hair cell sensor was low stability, because supporting the hair at its base with only the small hydrogel volume allowed the hair to easily fall over during perturbation, thereby causing the bilayer to rupture or the gel volume to be displaced from the compartment.

We revised the design by rooting the hair into the polymeric substrate so that the hair does not fall and that it resumes its original orientation after perturbation ends. To characterize the durability, we subjected the revised embodiment to two types of stimuli: repeated-flicking and continuous airflow. Figure 16a shows the response of the revised hair cell sensor to a single flick in which the hair is bent approximately 3-4mm and then released in a direction perpendicular to the bilayer. The resulting current is a second-order underdamped signal that diminishes to the pre-perturbation noise level in about 0.14 seconds. Figure 16b shows a series of transient current responses to 19 flicks of the hair when 60mV is applied across the membrane. The similarity of these transient responses shows that the bilayer remains stable during and between successive flicks and

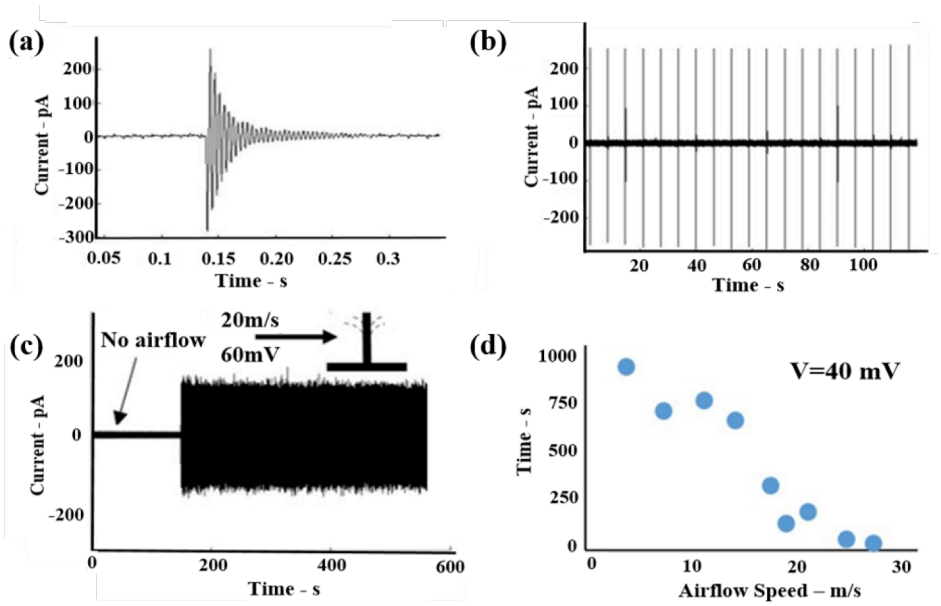

Figure 16: (a) Current response to a single flick of the hair. (b) Current response to 19 successive flicks of the hair. (c) Current response to the airflow at 20 m/s with 60mV applied across the membrane. (d) Bilayer lifetime of the revised transducer at different airflow speeds.

that repeated flicks create consistent motions in the membrane, a clue that indicates both the boundary condition of the hair and the area of the bilayer are unchanging. Moreover, we observed in additional tests that bilayers in the revised sensor are unaffected by the speed or number of the flicking events.

The second type of perturbation stimulus we used to examine the stability of the system is airflow. The sensing response in Figure 16c shows the sensing before and during excitation by airflow at a speed of 20m/s. The applied membrane voltage during this measurement is 60mV, and the data shows that the current amplitude remains stable for 4 minutes at which point the lipid membrane suddenly ruptures, ending the test. We observed that the amplitude of the measured current waveform remains steady prior to spontaneous rupture and that the hair retains its position in the substrate. Compared to the first study [4], which utilized slower airflow for short durations (~10s), this result highlights the added durability of the revised design. Building on this result, a similar routine was then performed for airflow speeds ranging from 5-28m/s at constant voltage of 40mV to identify the relationship between the lifetime of the membrane and the strength of airflow. Figure 16d summarizes the results of these measurements, where the data points indicate a single measurement of the lifetime of the interfacial bilayer after airflow is initiated. These measurements show that the lifetime of the membrane is inversely proportional to the speed of the applied airflow. The sensor provides a stable current response (Figure 16c) for more than 10 minutes in tests using airflow at speeds <10m/s. Above 20 m/s, the sensor

can still provide a current output, but the maximum duration of perturbation before rupture occurs falls to less than 1 minute.

3.5 Characterization of Mechanoelectrical Sensing Response

Previous research demonstrated that the capacitive sensing current in response to airflow is voltage dependent [4]. Specifically, the current generated by the membrane depends on both the time to the third power of voltage, *V*, because the capacitance of the bilayer, *C*, itself follows a linear trend with respect to V^2 due to electrowetting. The expression for sensing current, *i(t)*, is given by

$$i(t) = \frac{dC}{dt}\left(V + \alpha V^3\right) + i_{v=0}, \qquad \textbf{Equation 8}$$

where *α* is the electrowetting constant for the two monolayers that comprise the membrane and *dC/dt* is the time rate of change of bilayer capacitance induced by mechanical perturbation of the hair. The relationship also includes the term, $i_{v=0}$, which represents the current produced by mechanical vibration of the positive electrode [164]. The subscript *v=0* is used to denote that this background current is non-capacitive, and, hence, it does not vary with the applied voltage [164]. As a result, the amplitude of the sensing current increases with respect to the rate change of capacitance due to membrane vibration and the increase in capacitance due to electrowetting by the two droplets.

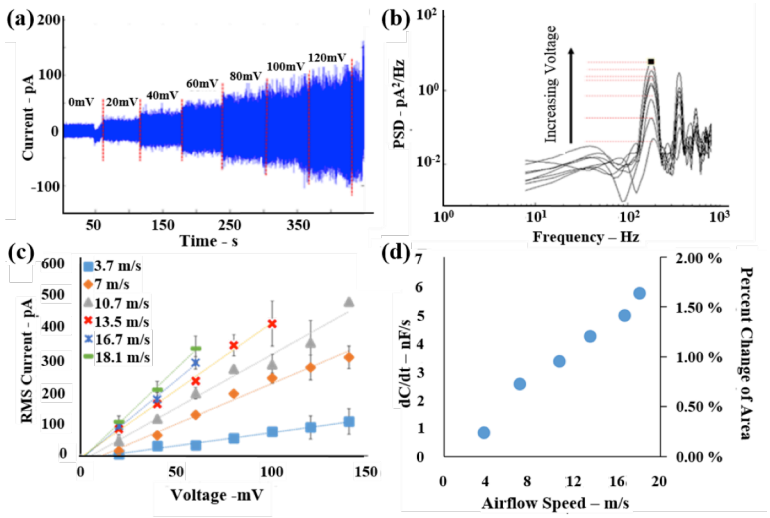

Figure 17: (a) The current response at different voltages for an airflow speed of 7m/s. (b) Power spectral density of current at different voltages for airflow at 7m/s. (c) RMS current versus voltage at different airflow speeds. (d) Time rate change of bilayer capacitance (left axis) and the percent area change (right axis) for different airflow speeds.

3.5.1 Quantification of the Time Rate Change of Membrane Capacitance

The purpose of the first part of the study is to quantify the time rate of change in capacitance of the membrane, *dC/dt,* which provides a measure of how much the bilayer vibrates in response to perturbation of the hair, across a wider range of stimuli strength. To do so, a series of experiments were performed at varying airflow speeds. Airflow was applied to the hair cell in a direction perpendicular to the bilayer in all cases. At each flow speed, the current produced by the bilayer was measured for 20s at applied transmembrane voltages from 0 to +140mV in 20mV steps. Figure 17a shows the raw current response to continuous airflow at 7 m/s applied, and the increases in current correspond to stepwise increases in the applied dc voltage. At each voltage level, the tip of the hair exhibits a net

deflection of ca.1mm, about which it vibrates in the airflow. Since the airflow exits a small, 0.6mm diameter needle, it is likely the hair moves in and out of the flow path during excitation. Under steady airflow, the current at each voltage exhibits two primary resonances (180Hz and 360Hz) as shown in the power spectral densities (PSDs) in Figure 17b. The amplitude of the PSD at resonance increases with the amplitude of the applied voltage. This result confirms that the membrane produces a capacitive current and that the frequency of oscillation is independent of the applied voltage level. Separately, measurements at different airflow speeds also confirm that the frequency of the current oscillation is independent of the airflow speed, indicating that the membrane vibrates at a constant speed regardless of the airflow strength. The fact that the peak frequency of the current of all airflow speeds matches the natural frequency of the hair, as determined by high speed imaging (see *section 3.5.3.*), confirms that the hair vibrates at its natural frequency at all speeds tested. The second harmonic in the PSD analysis (Figure 17b), which is also voltage dependent, indicates that the membrane also vibrates at the first harmonic of the hair's fundamental frequency.

Figure 17c shows RMS values of the measured current versus applied voltage for 6 different flow speeds from ~4-18m/s. Each data point in this figure represents the average of the RMS current measured for three different bilayers formed in the same substrate and tested with the same hair at each voltage and speed. The measured current at zero volts during the airflow has been subtracted from each of the averaged current values to remove background

current ($i_{V=0}$) not associated with membrane vibration. In addition, the areas of the bilayers were held constant at ca. 0.042mm^2 at every voltage level by using the regulated attachment technique [56] to return the bilayer area to its zero-voltage value. This correction was applied to eliminate changes in area of the bilayer due to the electrowetting effect (i.e. α=0) [4]. Consequently, the data show linear relationships between RMS current versus voltage for the various airflow speeds, where the slope of each current-voltage series represents the time rate of change of membrane capacitance, *dC/dt*, at each airflow speed. More generally, the data show that lower airflow speeds produce less current per unit voltage, while faster airflow induces higher current output due to greater deflection of the hair.

3.5.2 Estimation of Percent Change in Membrane Area under Airflow

In this section, we use the frequency content information to compute the dC/dt and maximum change of are of a membrane during perturbation. Based on the frequency content in the measured current, we assume that the sum of sinusoidal membrane oscillations at two resonance frequencies creates a total variation in membrane capacitance, as given by

$$C(t) = C_1 \sin(\omega_1 t) + C_2 \sin(\omega_2 t), \qquad \textbf{Equation 9}$$

that produces current during perturbation. C_1 and C_2 are the respective amplitudes of capacitance change (F) at frequencies ω_1 and ω_2 (rad/s). The time rate of change in total capacitance is thus

$$\frac{dC}{dt} = C_1\omega_1 \cos(\omega_1 t) + C_2\omega_2 \cos(\omega_2 t) \qquad \textbf{Equation 10}$$

The root-mean-squared value of *dC/dt* is given by:

$$\left(\frac{dC}{dt}\right)_{RMS} = \left(\frac{C_1\omega_1}{\sqrt{2}} + \frac{C_2\omega_2}{\sqrt{2}}\right). \qquad \textbf{Equation 11}$$

Integration of the PSDs revealed that the two frequencies contain equal fractions of the total power of the measured current signal, where the electrical power of a variable capacitor at constant voltage is given by

$$P = \left|\frac{dC}{dt}\right| V^2 \qquad \textbf{Equation 12}$$

.

Thus, we can show that the amplitudes of the time rates of change in capacitance for the two frequencies are equal:

$$\left|\frac{dC}{dt}\right|_{\omega_1} = \left|\frac{dC}{dt}\right|_{\omega_2}. \qquad \textbf{Equation 13}$$

Comparing Equation 13 to the amplitudes of the two sine functions in Equation 10 reveals that

$$C_1\omega_1 = C_2\omega_2 \qquad \textbf{Equation 14}$$

.

Because we know that $\omega_2=2\omega_1$, Equation 14 shows that $C_2=C_1/2$. This finding allows Equation 11 to be written in terms of only the first amplitude of capacitance and frequency, as given by

$$\left(\frac{dC}{dt}\right)_{RMS}=\left(\frac{C_1\omega_1}{\sqrt{2}}+\frac{C_1\omega_1}{\sqrt{2}}\right)=\frac{2}{\sqrt{2}}C_1\omega_1 . \qquad \textbf{Equation 15}$$

Solving for C_1 yields

$$C_1=\frac{\sqrt{2}}{2\omega_1}\left(\frac{dC}{dt}\right)_{RMS} . \qquad \textbf{Equation 16}$$

This expression provides a way to estimate the amplitude of the change in capacitance at the first frequency of oscillation. However, because the two frequencies are different ($\omega_2=2\omega_1$) the amplitude of the total change in capacitance is not merely the sum of C_1 and C_2. Instead, the maximum value for $C(t)$ occurs at an angle, θ, that satisfies:

$$\sin(\theta)=\sin(2\theta) . \qquad \textbf{Equation 17}$$

Equation 17 is satisfied for an angle of π/3 (60°). The amplitude of total variation of membrane capacitance at this angle is given by:

$$\left|C(t)\right|=C_1\sin(\pi/3)+\frac{C_1}{2}\sin(2\pi/3) . \qquad \textbf{Equation 18}$$

Solving Equation 18 for $|C(t)|$ and substituting Equation **16** for C_1 thus yields:

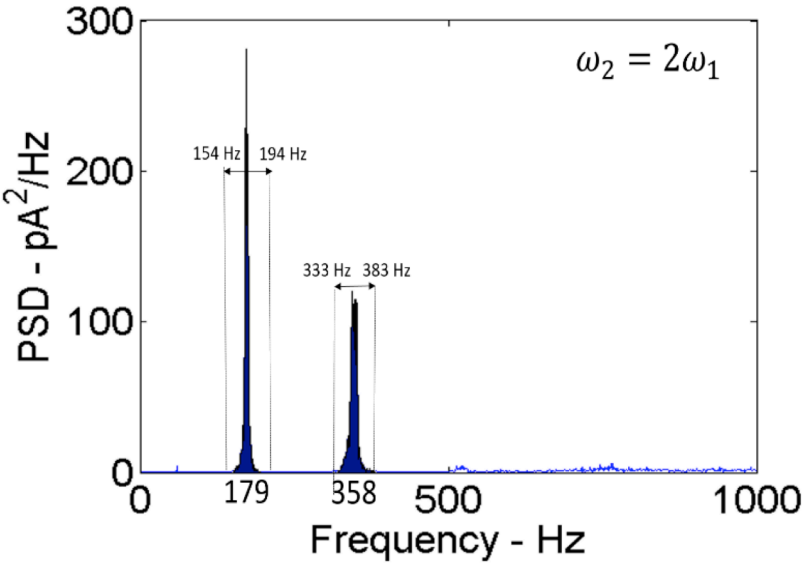

Figure 18: Power spectral density of sensing current measured for a membrane-based hair cell at 7m/s with an applied voltage of 40mV. Shaded areas represent the total power contained in the current signal at both frequencies.

$$|C(t)| = C_1\left(\frac{\sqrt{3}}{2} + \frac{\sqrt{3}}{4}\right) \approx 1.3C_1$$

$$|C(t)| = 1.3\frac{\sqrt{2}}{2\omega_1}\left(\frac{dC}{dt}\right)_{RMS} \quad .$$

Equation 19

Lastly, the percent change in membrane capacitance (and thus area) is calculated by:

$$\%\ \text{change} = \frac{|C(t)|}{C_0} \times 100 \quad ,$$

Equation 20

where C_0 is the capacitance of the bilayer at zero volts. C_0 was controlled using the RAM technique as describe elsewhere [56] to be 250pF in all tests.

Figure 17d shows a plot of the RMS time rate of change of capacitance versus airflow speed taken from the current-voltage series in Figure 17c. This presentation shows clearly that the time rate of change in bilayer capacitance is proportional to the strength of the applied stimulus (i.e. not the transmembrane voltage) and that *dC/dt* increases linearly with respect to the level of hair perturbation as given by airflow. Using the RMS value of *dC/dt,* we also estimated the maximum percentage change in bilayer area for each airflow speed **(**Equation 20**).** The following procedure is used to estimate the magnitude of the change in capacitance and therefore the area of the membrane. The power spectral densities of the sensing currents () showed dominant peaks at two frequencies: 180Hz and 360Hz. Numerically integrating the PSDs at both peaks (±25Hz) (shown for a representative PSD in Figure 18) reveals that more than 90% of the total power in the measured current signal is contained at these two frequencies. Considering just the cumulative area under these two peaks, comparisons of their respective areas shows that the first resonance frequency contains on average 52.3±5.5% of the power and the second harmonic contains the remaining 47.7±5.5%. These average values (±1 standard deviation) reflect many (*n*=32) measurements made on separate bilayers tested across multiple voltages and air speeds. Given these statistics, we assume that the power distributes evenly (50% and 50%) between these two frequencies in our following analysis.

This was accomplished by computing the amplitude of membrane capacitance during hair oscillation as given by:

$$C = \frac{1.3}{\sqrt{2}\omega_1}\left(\frac{dC}{dt}\right)_{RMS}, \qquad \textbf{Equation 21}$$

where, the ω_1 is the first natural frequency (180Hz) of the hair determined from the PSDs of the sensing currents (Figure 17b). The percentage change in the area is computed by dividing the amplitude of membrane capacitance by the capacitance of the membrane measured at zero volts. Because *dC/dt* is dependent only on airspeed, ω_1 does not vary with airflow speed, and the zero volts capacitance of the bilayer was constant in all tests, the computed percentage change in bilayer area is the product of a constant and the measured RMS values of *dC/dt*. Thus, the corresponding percent changes in bilayer area versus airflow speed are provided on the right axis in Figure 17d (see section 3.5.3).

The range of measured *dC/dt* values for the revised sensor is 0.8-6nF/s across airflow speeds from 3-20m/s, which is significantly higher than for the original sensor (45-60pF/s).[4] This increase in *dC/dt* values for the revised sensor is attributed to both higher levels of membrane bending and increased durability, which allows for measuring *dC/dt* at higher flow speeds. At the speeds tested, the measured values for *dC/dt* correspond to variations in membrane capacitance on the order of 0.2-2.0%, which is 10-100X higher than that measured for the initial membrane-based hair cell.[4] For example, the initial hair cell embodiment exhibited 0.027% area change at an approximate air speed of 7m/s [4], whereas we measure a 0.68% change in ≠≠area at the same air speed. Furthermore, at speeds nearing 20m/s, the membranes exhibit changes in area of approximately 1.8%. These values for change in bilayer area agree well with critical areal strains of 1-5% measured elsewhere on phospholipid bilayers [71].

This increase in bilayer bending is attributed to fixing the base of the hair in the substrate, which creates a condition in which vibrational energy of the hair can be more effectively transmitted to the membrane, both through the aqueous volumes and indirectly through the substrate.

3.5.3 Relationship between Hair Motion and Current

In this section we seek to understand the mechanism of mechanoelectrical transduction for our revised sensor by relating the frequency content of the hair's oscillatory motion to the frequency content contained within a PSD of the sensing current. This is accomplished through the use of high-speed imaging is used to correlate the motion of the hair to the measured current. This measurement is

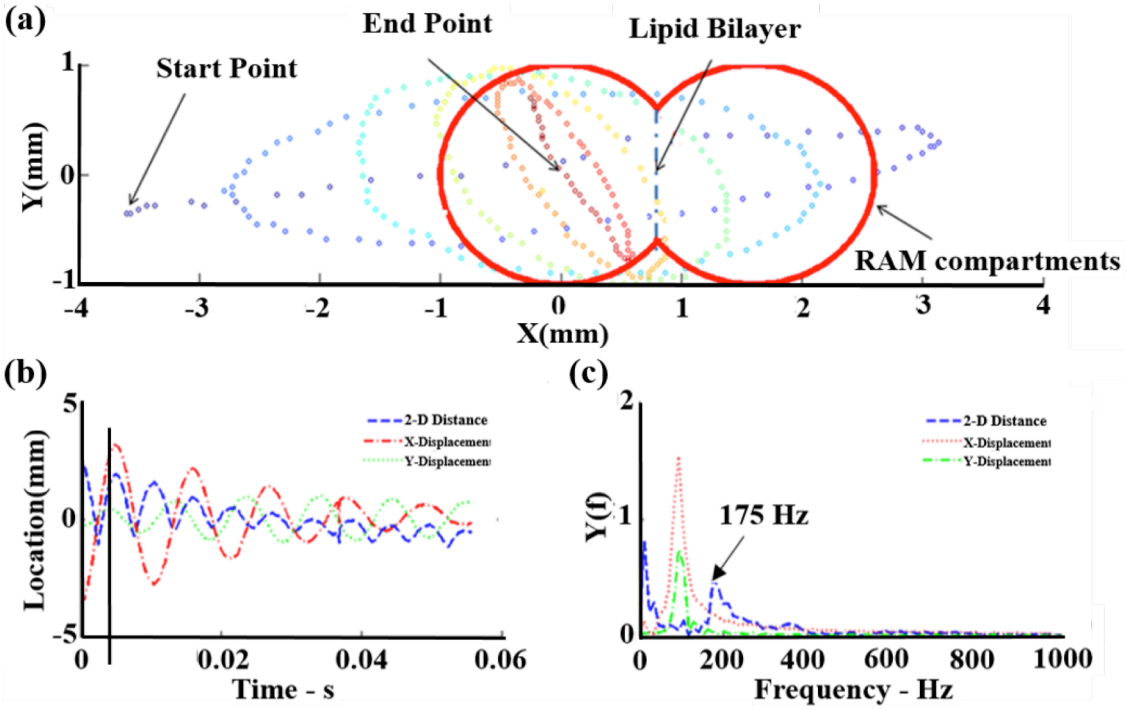

Figure 19: (a) The motion of the hair from the top view captured by 6000fps high speed camera. (b) the FFT of the hair motion in x, y and total distance from the center. (c) FFT spectral of hair motion in x, y and the total distance from the end point.

taken without a bilayer present and without simultaneous recording of current due to instrumentation constraints, yet the fixed hair position and inclusion of liquid volumes provides similar mechanical boundary conditions necessary for replicating the response that would occur during a sensing test of a bilayer formed between two liquid volumes. Figure 19a shows the results of an image tracking routine performed on the high-speed images collected of the tip of the hair (not shown) as the hair is bent (starting point), released, and allowed to vibrate until it returns to the resting position (end point). The data points indicate the *x* and *y* position of the tip of the hair in 0.001s increments in time as imaged from above by the camera at 6000 frames per second. The data points show that while the hair is initially bent and released by the flicker primarily in the *x* direction perpendicular to the membrane, the hair's trajectory changes during the next few oscillations to include motion in the *y* direction as well. Figure 19b shows the *x* and *y* positions of the tip of the hair as a function of time. Also included in this plot is the magnitude of the two-dimensional distance ($d=(x^2+y^2)^{1/2}$) relative to the final resting position of the hair (as marked in Figure 19a). Figure 19c shows fast Fourier transforms (FFT) of hair motion calculated from time traces of *x*, *y*, and *d*. As can be seen, the peak frequencies of hair motion in the x and y directions are approximately equal at 93 Hz, whereas the peak frequency of the two-dimensional displacement is approximately 175Hz. This near-doubling in frequency content for the total distance versus time is attributed to the out-of-phase motion of the *x* and *y* trajectories, which matches very well to the first

resonance peak (175Hz) shown in the PSD spectrogram of the sensing current for the fully assembled hair cell.

This agreement between the motion of the hair and the current response of the membrane provides additional confirmation that motion of the hair is responsible for the time rate of change in the capacitance of the bilayer. Previous studies also suggest that the transverse bending of the bilayer at the same frequency of the hair produces capacitive current at the same frequency [165, 166]. Thus, by adding these two results, we believe that the membrane in the revised sensor undergoes one full bending cycle upon one complete oscillation cycle of the hair. The fact that the membrane shows an ability to transduce hair motion in multiple directions is likely due to redirected motion of the droplet that is caused by perturbation of the hair. We have to note that while movement of the hair in the *x* and *y* directions occur at the same frequency, we see the highest strength of the motion in the direction of the flick (i.e. higher peak strength for *x* as opposed to *y*). Moreover, we will show in the next section that the membrane bends more when the airflow is directed perpendicular to the membrane as opposed to parallel.

3.5.4 Directionality of Sensing Response

While our prior work showed that the cause for changing membrane capacitance and current produced as a result of airflow is transverse bending of the membrane due to hair vibration [4], the effect of perturbation direction on the membrane's mechanoelectrical response has yet to be studied in detail. Thus,

we characterized the sensing response of a membrane to airflow across the hair at angles of 0°, 45°, and 90° with respect to the planar lipid bilayer (Figure 20a, b). At each angle, the RMS current produced by airflow at 13.5m/s is measured as a function of the applied voltage. Each data point in Figure 20c shows the average of the RMS current measured for three different membranes tested at each voltage and perturbation angle, and the error bars indicate ±1 standard deviation of the three responses. Here again, the area of each membrane is kept constant for all voltage levels and perturbation levels.

Similar to the data in Figure 17c, the data in Figure 20c shows that the RMS current increases linearly with increasing voltage, regardless of angle. However, the magnitude of the sensing current also depends on the angle of perturbation.

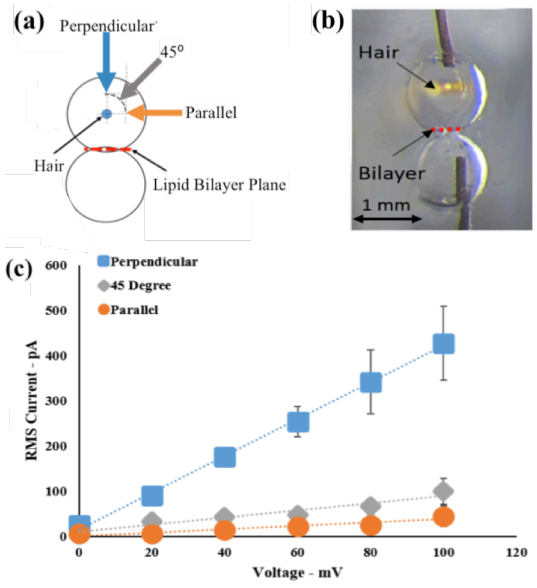

Figure 20: (a) Schematic of direction of airflow relative to membrane orientation and (b) corresponding picture of the hair cell in the same configuration shown in schematic. (c) RMS current versus direction of perturbation for steady airflow at

Airflow across the hair in a direction perpendicular to the bilayer generates the largest response, while perturbations at angles more parallel to the membrane yield less current. Linear fits to the three current versus voltage series is used to compute the time rate change of capacitance at the different airflow directions. The values of R^2 for all linear fits are higher than 0.98. As shown in the previous section, the bilayer moves at the same frequency regardless of airflow speed. A similar effect is observed here with respect to airflow direction, therefore the *dt* portion of the time rate change of capacitance is independent of the direction of airflow. Thus, we can conclude that changing the direction or strength of airflow only affects the capacitance of the membrane, the *dC* in *dC/dt*. The sensitivity value for perpendicular (90°) airflow is highest at 4.05nF/s, whereas measured sensitivity is only 0.81nF/s and 0.27nF/s for 45° and parallel (0°) airflow, respectively. This result shows that the direction of the hair's motion directly influences the membrane's response to a particular perturbation. As the sensor is most sensitive when the hair is perturbed in a direction perpendicular to the membrane, this data provides added proof that transverse bilayer bending is responsible for the time rate change in capacitance. The fact that the raw currents measured for each direction of perturbation exhibit identical frequency responses (not shown) indicates that frequency of the membrane's motion is driven by oscillation of the hair and not the direction of applied airflow. Together, these results suggest that membrane-based hair cell sensors could be used to determine both the magnitude and direction of an applied stimulus.

3.5.5 Low Frequency Response of Haircell Sensor

We also characterized the membrane response to stimuli at frequencies lower than the hair's resonance. In this set of tests, we used a mechanical shaker to vibrate the hair perpendicularly to the plane of the membrane (90°) at 20, 30, and 40Hz. With this form of excitation, the horizontal displacement of the top of the hair decreases with increasing frequency because of power limitations that reduce the periodic displacement of the mechanical shaker. Shaker displacements for 20, 30 and 40Hz frequencies were measured to be 2.5, 2.0 and 1.5mm, respectively. The calculated values of hair deflection at the center of the excited droplet using a similar triangle approximation (i.e. minimal hair bending) are approximately 0.7, 0.6 and 0.5mm, for 20, 30 and 40Hz, respectively. Raw current in response to 30Hz oscillation of the hair with about 2mm deflection is shown in Figure 21a. The applied voltage is increased by 20mV every ten seconds to 120mV before being returned to zero as shown by the arrows. Here again, we see a voltage-dependent response in the measured current, which tells us that the current is generated by a time rate of change in the capacitance of the bilayer as the hair is continuously oscillated. Similar to free vibration or airflow tests that induce resonance in the hair (~180Hz), this result confirms that the bilayer is capable of transducing motion of the hair at frequencies below resonance.

The power spectral densities of the current responses at the three oscillation frequencies at 60mV are shown in Figure 21b, where the arrows indicate the first peak frequencies for the three current traces. For each oscillation setting, the

frequency of this first peak matches the shaker (i.e. the hair) frequency. This result indicates that as the hair is being shaken in a direction perpendicular to the membrane, it produces a time rate change of capacitance in the membrane at the same frequency of the input excitation. The remaining peaks in the computed PSDs are found to be harmonic frequencies of the first peak of the current response. Also, there is a broad peak in the PSD of the current response for 40Hz hair vibration close to the natural frequency of the hair, which is most likely due to detachment of the hair from the connecting rod that allows oscillation at the hair resonance frequency during the shaking.

Figure 21c shows the power distribution of the sensing current at 20 and 30 Hz, respectively, versus voltage. In this analysis the power generated by the positive electrode is taken out from each data points. As shown above with airflow, the power across the membrane generated by the time rate change of capacitance

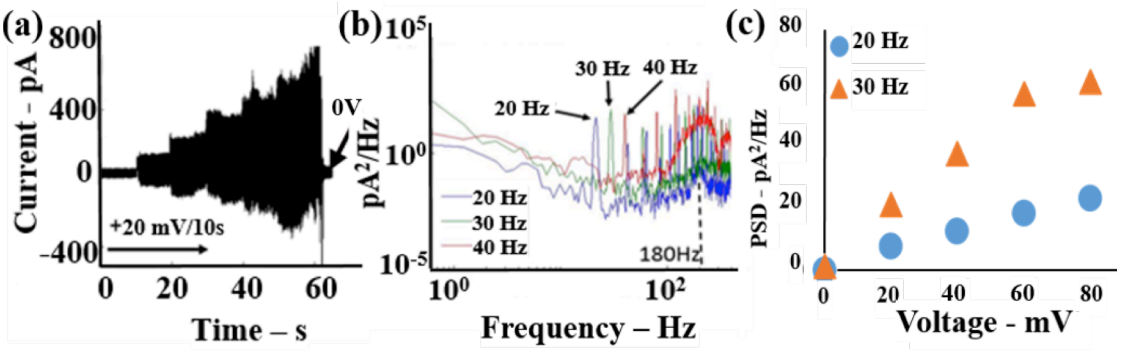

Figure 21: (a) The current response to 30Hz oscillation applied to the hair by a shaker during which the voltage is increased by 20mV every 10s. (b) Frequency content of current responses for perturbation at 20, 30 and 40Hz. (c) The magnitude of the PSD at the driving frequency versus voltage for 20 and 30Hz driving frequencies.

increases by increasing the applied voltage. We notice that higher driving frequency produces higher signal power. Because of this difference in sensor output at the two frequencies, we compare the ratio of time rate change of applied hair displacement, *dx/dt*, to the ratio of the measured RMS current (equal to the ratio of the *dC/dt* at a given voltage) for both 20 and 30Hz vibrations. The computed *dx/dt* ratio of the hair motion of 30Hz to 20Hz ($(dx/dt)_{30Hz}/(dx/dt)_{20Hz}$) is approximately 1.28. The average ratio of measured *dC/dt* for bilayer for 30 to 20 Hz ($(dC/dt)_{30Hz}/(dC/dt)_{20Hz}$) is 1.31±0.12 for voltages between 20 and 80mV. The fact that the ratio of the output (*dC/dt*) is within ±10% of the ratio of the input (*dx/dt*) at the two frequencies shows that the increased current produced at 30Hz is due simply to the higher rate of change in the applied hair displacement. This result also shows that the sensor exhibits a linear response in that the ratio of the output is equal to the ratio of the input at these frequencies. We did not consider the 40Hz response in this comparison because the PSD of this measurement indicated that the hair likely detached from the shaker during excitation, which would cause the magnitude of response to not scale well with the applied frequency. Additionally, higher frequencies were not tested for the reason that the shaker displacement decreased significantly at higher driving frequencies.

3.5.6 Effect of Aqueous Volume Compositions

In the previous work, the lipid bilayer was formed between one lipid-encased liquid volume and one lipid-encased, water-swollen gel volume used to support the hair [4]. The fact that the PDMS substrate supports the hair in the new embodiment affords the use of either liquids or gel materials as the lipid-coated

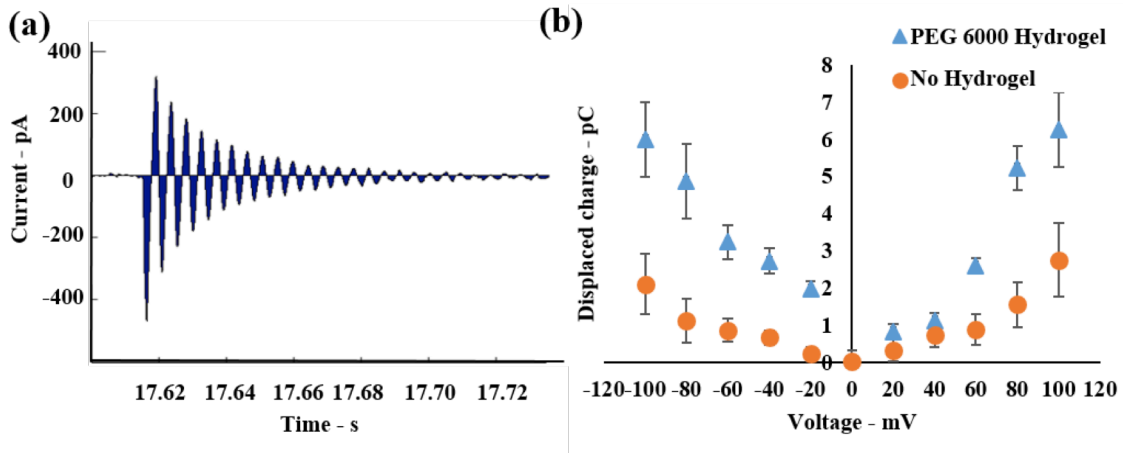

Figure 22: (a) Transient current response due to one flick of the hair (shaded area represents calculated displaced charge). (b) Displaced charge versus applied membrane voltage for bilayers formed between lipid-coated liquid volumes and photopolymerized PEG-

aqueous volumes. Thus, we now examine the effect of using liquid volumes or polymerized hydrogels as the aqueous volumes on the current response of the interfacial bilayer. Specifically, we form and characterize a membrane-based sensor consisting of two volumes of either liquid liposome solution or the hydrogel mixture. A bilayer is formed as described earlier, and, in the case of using gels, the hydrogel volumes are photopolymerized before characterization of sensing response. In place of airflow, sensing current is measured and recorded for 10 to 12 successive flicks of the hair using the automated flicker, each at applied voltages ranging from -100mV to +100mV in 20mV intervals. In this set of experiments, the area of the bilayer in each test is not held constant. Therefore the bilayer area changes due to the electrowetting effect as we apply voltage across the membrane, and the current and displaced charge agree with the third order model of the hair cell provided in Equation 1.

Figure 22a shows a second-order underdamped current response of a single flick to the hair. To compare these transient responses for the two different aqueous compositions tested, we compute the total charge displaced across the membrane during hair vibration as the area under the current, versus time trace (shown as the shaded region). Figure 22b shows the average displaced charge across three separate membranes for each of the two aqueous compositions at varying applied voltages, where the error bars represent ±1 standard deviation. The data show that both compositions display a voltage-dependent charge response, where increasing the applied voltage results in a greater amount of displaced charge for the same flick. Moreover, we see that hydrogel-sandwiched membranes produce a larger response compared to bilayers formed between two liquid aqueous volumes. For example, a bilayer formed using liquid volumes generates a displaced charge of ~4pC at |100mV|, while a bilayer formed between gel volumes generates nearly twice as much charge. The data show that charge for either case does not increase linearly with voltage, due to the fact that the area of the bilayer was not held constant in this experiment.

The slopes of linear fits to the displaced charge versus voltage data are extracted to compare the sensitivity of bilayer response for the two types of aqueous volumes. The observed sensitivity (0.066pC/mV) for the bilayers formed between 10% PEG 6000 hydrogel is significantly higher than that (0.015pC/mV) measured for a bilayer formed between aqueous volumes containing 0% gel. This value is the average absolute value of the slope of linear fits at both positive and negative voltage. The higher sensitivity of the hair cell sensor with bilayer formed between

hydrogels indicates that the stiffer hydrogel materials on both sides of the membrane produce higher *dC/dt* in the membrane. While it may be counterintuitive, since a stiffer gel could possibly restrict bending of the bilayer, the hydrogels likely do a better job than liquid volumes at transmitting energy of the hair's motion to the interface. Instead, liquid volumes likely damp more energy, leading to a lower time rate of change in capacitance of the bilayer. Again, we noted that the membrane did not rupture due to flicking even though it did rupture at high voltage. The durability of the membranes in both cases was similar in response to flicking.

3.6 Quantification of Sensor Performance

The data presented thus far help explain the physical mechanism by which an interfacial lipid bilayer converts a mechanical stimulus into an electrical current. The effects of perturbation strength, direction, and frequency and aqueous volume composition on the magnitude and frequency content of the output current were studied. However, these tests also provide information useful for characterizing the assembly in terms of traditional sensor metrics including sensitivity, dynamic range, detection thresholds, and failure mechanisms.

Figure 23a re-presents the data from Figure 17c in terms of sensor output (RMS current) versus stimulus input (airflow across the hair in a direction perpendicular to the bilayer) at the tested values of membrane voltage. This format is structured specifically to examine the sensitivity, range, and threshold of the transduction

process, instead of measuring *dC/dt*, where the applied voltage can be considered as a tunable operation point for the device. Similar to the current-voltage series, the current-airspeed data series show linear relationships across their operation ranges. The slopes of these series represent the sensitivities in response to airflow at various voltages (Figure 23b). When only 20mV is applied across the bilayer, the sensor exhibits a sensitivity of approximately 5pA RMS per m/s and can withstand airflow rates as high as 28m/s before rupturing due to excessive mechanical perturbation. Conversely, an applied bias of 120mV

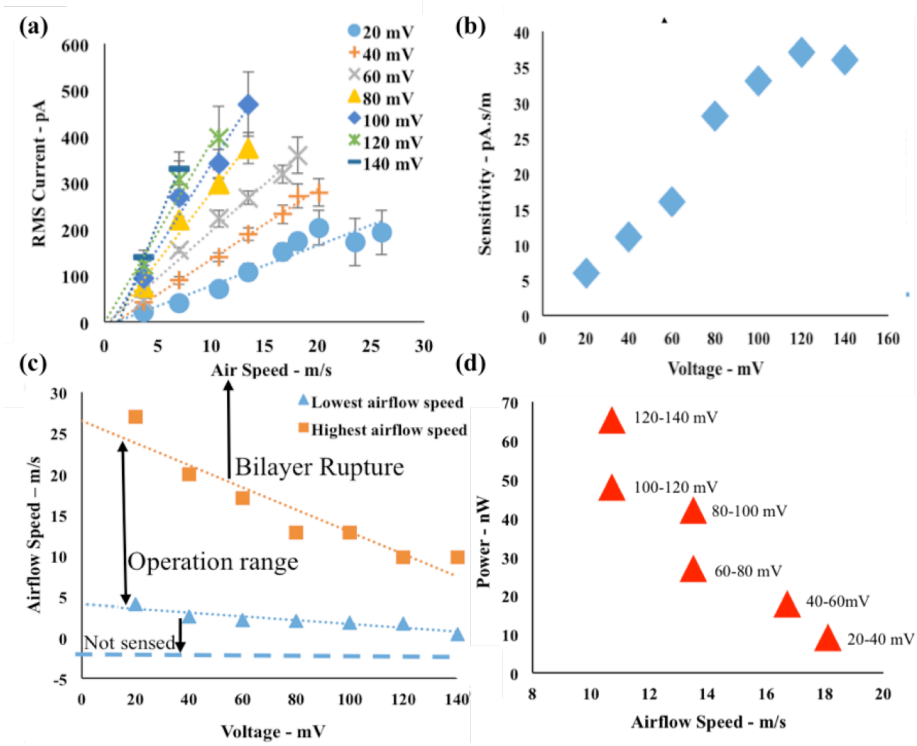

Figure 23: (a) RMS current versus airflow speed at different operation voltages. (b) Sensitivity to airflow at a direction perpendicular to the membrane versus voltage. (c) Minimum (triangles) and maximum (squares) airflow speeds that can be sensed versus operation voltage. (d) Electrical power of the membrane versus air speed at the maximum allowable voltage prior to rupture.

produces a much higher sensitivity (>35pA RMS per/m/s) but across a narrower range of airspeeds (<15m/s). This presentation confirms that sensitivity rises with increasing voltage, where the largest gain in sensitivity is observed between 20 and 100mV.

The minimum current that the hair cell can sense is the interception of the linear fit of current versus airflow at different voltages and zero current (i.e. the *x*-axis) in Figure 23a. Both the minimum sensing threshold and the maximum allowable airflow speed of the sensor, as illustrated in Figure 23c, decrease with increasing applied voltage. For example, the minimum and maximum airflow speed at +20mV are 4.2m/s and 28m/s, respectively, whereas they fall to 0.6 m/s and 13.5m/s, respectively at +140mV. Recalling the computed percent area changes of the membrane are functions of the stimulus level (Figure 17d), these data provide insight into the amount of deformation and voltage that lead to membrane rupture. An air speed of 13.5m/s at 140mV corresponds to a change in membrane area of roughly 1.3% (Figure 17d), whereas biasing the membrane with only 40mV allows for airflow at 18m/s and 1.7% change in membrane area before rupture.

Using Equation **12**, we computed the maximum electrical power of the membrane measured prior to rupture at each airflow speed (Figure 23d) to understand if a common power level leads to membrane rupture. Instead, the data show that the maximum power in the membrane is a combination of both airspeed and voltage. At low applied voltages, a membrane can withstand higher

airspeeds, and thus higher amounts of deformation, without rupturing. In contrast, the membrane is able to withstand much less perturbation from airflow when the applied bias is large. We see the maximum electrical power (~65pW) of the membrane occurs for combinations of slower airflow and higher voltages across the different speeds, since the power is proportional to square of the applied voltage. Yet, for the range tested, neither airflow alone nor voltage was sufficient to cause membrane rupture. Thus, we conclude that both the applied voltage and the sustained perturbation level contribute to causing membrane failure, and that the mechanical energy state as opposed to the electrical power dissipated may provide a better marker of failure. One possibility is that voltage-induced electrostriction of the bilayer creates stored mechanical energy in the membrane that adds to the vibrational energy induced when the hair is perturbed.

3.7 Summary and Conclusions

In this chapter the more durable membrane-based hair cell sensors were developed to better understand sensing and dynamic characteristics of lipid bilayers under both discrete and continuous types of perturbations. In this study, we showed that the current response of a revised membrane-based sensor is dependent on several parameters: 1) the voltage across the membrane, 2) the strength, direction, and frequency of the perturbation, and 3) the material compositions of the aqueous volumes used to form the bilayer. The revised embodiment features a hair that is rooted firmly in the polymeric substrate that

also supports the lipid bilayer. Compared to the first generation membrane-based hair cell sensor, the results of these experiments show that the new embodiment is much more durable, allowing large and repeated deformations of the hair. Due to greater robustness, we were able to more fully characterize the mechanoelectrical transduction process of a membrane-based hair cell sensor.

Cumulatively, the results confirm that the bilayer exhibits a time rate of change in capacitance (dC/dt) due to transverse bending in response to motion of the hair, where the magnitude of dC/dt depends on the strength and direction of the applied stimulus. Similar to the first generation of the hair cell sensor, analysis of the hair's motion relative to measured sensing currents at both resonance and lower frequency excitations show that the membrane vibrates at the same frequency of the hair. However, the higher values of dC/dt (0.8-6nS/s) and percent change in membrane area (0.2-2.0%) indicate that cantilevering the hair in the solid substrate results in greater energy transfer to the membrane resulting in bending; this is likely due to both a stiffening effect of the hair and added transmission of energy through the substrate. A more subtle benefit of the revised embodiment is the fact that the lipid aqueous volumes can be either pure liquids or liquid-swollen gels material. Our tests on both types of volumes show that the freedom to vary the material composition can be used to tailor both the mechanical properties and sensitivity.

In context to its use as a sensor, this study yielded new information regarding the sensitivity and dynamic range of a membrane-based hair cell in response to

airflow. These tests revealed that the current output by a sensor varies linearly with respect to the applied airflow for a given voltage level. However, a trade-off exists: while increasing the voltage amplifies the sensitivity of the response to airflow and reduces the minimum airflow speed that can be detected, it also narrows the range of airspeeds that can be detected without rupturing the bilayer. Nonetheless, the results confirm that the applied voltage can be used to tune the performance to a given application. A voltage <60mV may be best suited for sensing airflow across a wide range of speeds, while increasing the applied voltage to ~100mV can provide greater sensitivity and a lower threshold for detecting slower sources of airflow. This finding is especially important when comparing sensor modalities and in configuring a membrane-based sensor for a specific sensing application.

While this chapter characterized and provided better understanding of the sensitivity, directionality and effect of droplet compositions for intradroplet membrane based hair cell sensing, it is still unknown how the multiple-droplet and multi-hair arrays response to the hair motion. In the next chapter, we will show how multiple droplets can be connected to develop arrays of droplet-based hair cell sensors to study the propagation of vibration in droplet arrays, the relative timing of sensing responses of each membrane, and explore how multiple membranes respond to perturbations of multiple hairs in an array of connected droplets.

CHAPTER 4: TOWARD CELL-INSPIRED MATERIALS THAT FEEL: MEASUREMENTS AND MODELING OF MECHANOTRANSDUCTION IN DROPLET-BASED, MULTI-MEMBRANE ARRAYS [1]

4.1 Overview

Last chapter provided important information about the sensing characteristics and performance of the single membrane hair cell sensor. The goal of this chapter is to assemble and experimentally characterize the mechanotransduction responses of each membrane in a multi-membrane droplet array. The specific goals are to: a) understand how multiple membranes respond to the motion of one or more hairs in the array, b) assess the propagation of vibration in a droplet array by determining how many membranes away from a moving hair yield a sensing current, c) characterize the relative timing of sensing responses of each membrane relative to hair motion, and d) explore how multiple membranes respond to perturbations of multiple hairs in the array.

4.2 Introduction

A distinct feature of the droplet interface bilayer (DIB) is its modular assembly procedure, which allows for multiple lipid-coated water droplets to be joined to construct networks of lipid bilayer membranes in two [51, 102, 133, 167] and

[1] Note: This chapter presents findings reported in a recent journal paper published in Bioinspiration & Biomimetics - IOPscience entitled, “Toward cell-inspired materials that feel: measurements and modeling of mechanotransduction in droplet-based, multi-membrane arrays”.

three [168-171] dimensions, where the bilayers regulate transport between the aqueous interiors of adjacent droplets. Multi-bilayer DIB arrays thus provide a unique platform for mimicking the compartmentalization and coordinated transport that are ubiquitous in living cells and tissues: to-date DIB networks have been employed to convert visible light into proton currents [133], demonstrate tissue-like actuation via osmosis [171], and enable circuit-like functionality using ion channels [102, 104].

The membrane-based, hair cell-inspired sensor [4, 172] was the first use of DIBs to convert a mechanical stimuli such as airflow into an electrical signal. Unlike other hair cell-inspired solid-state devices [34, 37, 39, 173-180], this approach consists of a fluid lipid membrane arranged between two lipid-coated water droplets contained within an oil-filled polymeric substrate. This one-bilayer assembly allowed for experimentally studying the transduction mechanism, as well as exploring the sensor's sensitivity and directionality [172]. An artificial hair (i.e. cilium) inserted into one of the volumes mechanically couples motion of the hair to the bilayer membrane, which behaves as a deformable electrical capacitor. The vibration of the membrane causes a time rate of change of capacitance, dC/dt, which results in sensing current, i, given by the Equation 4 in chapter 2.

A key functional difference between a natural hair cell, such as an outer hair cell in the organ of Corti [10, 181-184], and a droplet-based membrane hair cell is that the synthetic version does not utilize membrane-bound ion channels to

transduce membrane tension or affect membrane curvature in response to cilia motions [185, 186]. And while Najem, et al recently demonstrated dynamic mechanical activation of reconstituted mechanosensitive ion channels in a DIB [187, 188], a lipid-only membrane-based hair cell utilizes the mechanoelectrical response of the capacitive lipid membrane to convert mechanical vibration into current. Past works by our group determined the origin of this passive response [4] and quantified its sensitivity, dynamic range, and directionality [172] using a sensor embodiment that consisted of a hair and a single lipid bilayer formed between two droplets as the transduction element.

Yet, despite the unique capability of the DIB method for constructing multi-bilayer arrays, the mechanoelectrical sensing capability of multi-bilayer droplet networks has not been studied. We hypothesize that the vibration induced by hair motion can propagate through multiple droplets; thereby allowing bilayers formed between droplets that are not in direct contact with the hair to indirectly sense hair motion. By understanding both how mechanical forces affect the sensing current in a single interface and how these mechanical forces transmit in DIB arrays, we propose that in addition to compartmentalized biomimetic systems for regulated transport [51, 102, 189-191], actuation [192-194], and sensing [55, 195], DIB arrays can also be applied to the development of tissue-like materials systems for spatially distributed sensing of dynamic forces, fluid flow, and vibration—just like how spiders [196, 197], fish [198, 199], and mammals [200] use hair cells to perceive their surroundings.

In this chapter, we study the mechanoelectrical responses of multi-membrane DIB arrays constructed from lipid-coated aqueous volumes connected in series and we demonstrate that, despite viscous energy dissipation between neighboring droplets, multiple interface bilayers in a DIB array are able to sense hair motion. The findings of this work provide insights into how droplets, membranes, and hairs can be effectively arranged for sensing and energy harvesting applications, as well as inducing mechanical stimulation necessary to excite transmembrane proteins like mechanosensitive channels [201].

4.3 Materials and Methods

We assemble and characterize serial DIB array configurations that differ in the number and arrangement of droplets, bilayers, and hairs to examine how multiple membranes contribute to mechanotransduction of the hair's motion. Figure 24 shows a representative 5-droplet, 4-bilayer linear array that features a single hair positioned in the leftmost droplet of the series.

4.3.1 Assembly of Droplet Arrays

Same method explained in 2.1.2 is used to fabricate the flexible polydimethylsiloxane (PDMS) substrates to support the hair(s) and contain the droplet arrays in oil (Figure 24a) [4, 56] but this time with multiple compartments. Based on the use of a manual micropipette for dispensing droplets that are ca. 1 mm in diameter, we use molding templates that contain up to five droplet compartments (each 1.016 mm diameter, 2 mm deep with hemispherical bottom

surfaces) arranged in either a collinear series (Figure 24). The compartments are spaced relative to one another to provide a 0.3 mm-wide dividing aperture in the PDMS substrates. Figure 24b shows how a 4-bilayer (B1-B4) array is supported in the substrate and instrumented for measurements. Silver-silver chloride wire-type electrodes (E1-E5) made from bleaching 125 μm diameter silver wire are inserted through the sides of the substrate such that the electrode tips pierce the lipid-coated droplets (Figure 24b). Paintbrush fibers (80 mm in diameter) are inserted vertically in the center of the desired compartments. Hairs of two lengths are used in these experiments: one is 12–14 mm (free length, defined as the length of the hair not inserted in the substrate, of 11–13 mm) and the other is approximately 16-18 mm (free length of 15–17 mm). These hair dimensions allow for easy insertion through the center of 1mm-diameter droplets and provide a free length that is significantly taller than the droplets such that perturbations can be applied independently to the hair without affecting the oil or droplets. Figure 24c shows a top view image of a 5-droplet array, with an Ag/AgCl electrode in each of the droplets.

Hexadecane (99% Sigma Aldrich) is used as the immersing oil phase in all experiments. All droplets consist of a 2 mg/mL solution of 1,2-diphytanoyl-sn-glycero-3-phosphocholine (DPhPC, Avanti Polar Lipids, Inc.) small unilamellar liposomes suspended in electrolyte containing 200 mM NaCl (Sigma Aldrich), 10 mM 3-(N-Morpholino) propanesulfonic acid (MOPS, Sigma Aldrich) and buffered to pH 7. Liposome solution is prepared as described elsewhere [189] and stored at 4°C for use within two weeks.

The following procedure is performed to dispense, position, and attach lipid-coated droplets in a substrate after insertion of the hair: 50 µL of hexadecane is first dispensed into the vacant compartments in the substrate and then 750 nL of lipid solution is pipetted into each compartment. The droplets are incorporated in an order such that each droplet resides in oil for 3–5 minutes to allow for monolayer formation prior to being placed in contact with droplets in adjacent compartments. These volumes can be divided after coalescence upon bilayer rupture by laterally compressing the solid substrate with a micromanipulator (SM-325, World Precision Instruments Inc.) as described elsewhere [56] for two-compartment substrates. The apertures are then reopened after 3–5 minutes by reducing compression on the substrate, whereby bilayers form spontaneously between every adjacent lipid-encased droplet.

4.3.2 Measurements of Electrical Sensing Currents

Bilayer formation is confirmed and perturbation-induced sensing responses are characterized using current measurements via the Ag/AgCl electrodes contacting the droplets. The electrode from each compartment is connected to a separate measurement channel on a Triton 8-channel patch clamp amplifier (Tecella) such that voltage is independently applied to each droplet and the current entering or exiting each droplet is independently measured. Capacitance measurements are performed to verify the increase in membrane capacitance that occurs upon bilayer thinning [202]; these measurements are also used to estimate the area of each membrane using a specific capacitance of 0.65 µF/cm^2 [167]. Specifically,

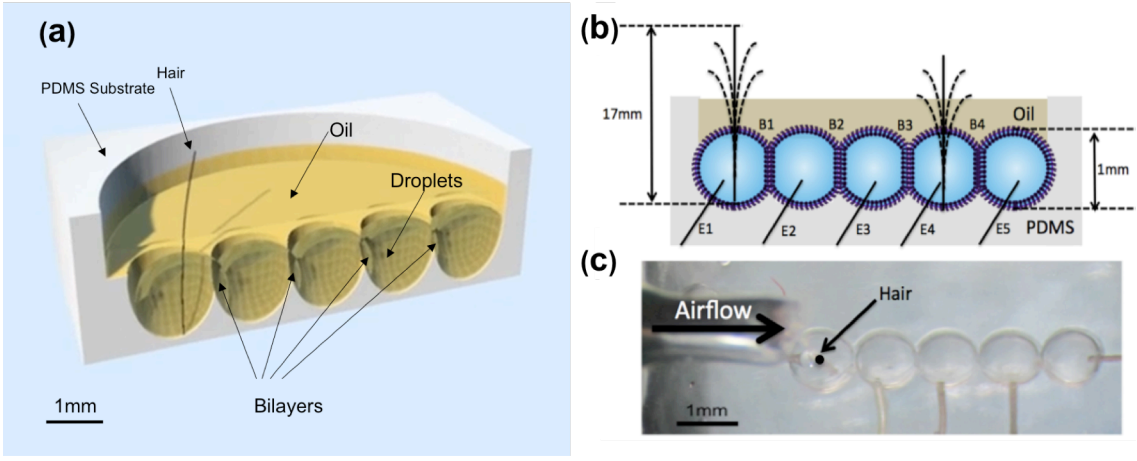

Figure 24: (a) Isometric view illustration a multi-membrane, serial droplet array hair cell sensor. (b) Side view schematic of the 5-droplet series instrumented with wire-type electrodes. (c) A top view image of an assembled 5-droplet serial array. The hair (out of focus) is oriented vertically, extending out of the plane of the image.

the multi-channel amplifier is employed to record the resulting square-wave currents induced by a 100 mV, 5 Hz triangular voltage waveform designed in TecellaLab software and output by the same amplifier. The triangular voltage waveforms are removed after measuring the capacitances of all membranes in an array.

A *dc* voltage is applied across every membrane to characterize its sensing response to hair perturbation since capacitive current is voltage-dependent [3, 172]. In a serial array of droplets, one droplet is assigned as the “virtual ground” for the circuit [167] and each lipid bilayer receives an identical transmembrane voltage (e.g. 40 mV) by assigning the voltage at the other electrodes to successive multiples of the same value. All current measurements are sampled at 20 kHz, low-pass filtered at 2 kHz within the amplifier, and saved as text files

for analysis in MATLAB. All experiments are performed within a grounded, homemade Faraday cage.

4.3.3 Characterization of Sensing Responses

In this work we perturb hairs using two methods: 1) with a narrow horizontal stream of air at constant velocity across a portion of the free length of the hair, which causes the hair to vibrate, and 2) by bending and releasing the hair with a motorized 'flicker' that impacts the hair at a distance of 1–2 mm from the free end. As described previously [172], a narrow stream of air impacting the hair causes the hair to bounce in and out of the stream. Thus, analysis of the sensing currents generated by airflow induced vibration enables measurement of the root-mean-squared (RMS) sensing response [3, 172]. Separately, sensing responses to hair flicking are used specifically to investigate the relative timing between sensing currents in multi-bilayer arrays. The subsequent hair motion caused by either source transfers vibration to the lipid bilayer, causing a time rate change of capacitance in the membrane that generates current [3, 172]. The *dc* transmembrane voltage applied equally to all bilayers is varied from 0 to +80 mV, and measurements are performed multiple times at each voltage level and for each array configuration. Flicking responses are assessed by computing the net charge displaced across each bilayer—i.e. the area under the current-time trace—during ring-down. The displaced charge across a single bilayer for a single flick of the hair is ca. 2-20 pC/mm^2 [172]. Before each sensing experiment, a control measurement is performed by flicking the hair rooted in the substrate

containing only electrodes and oil (i.e., no droplets and bilayers) to quantify the charge displaced by electrode vibration—a feature that is independent of applied voltage [172]. These amounts of background current (or displaced charge) for each electrode are then removed from the measured responses when a vibrating membrane is present.

4.4 Results

4.4.1 Sensing Responses in Multi-bilayer Serial Droplet Arrays

We first characterized the voltage-dependent sensing responses for membranes in a 5-droplet, 4-bilayer serial array that contained a single, 17 mm-long hair positioned in the leftmost droplet. Automated flicking and steady airflow are used separately to perturb the hair, and an equal potential applied to each membrane was varied between 0 and +80 mV. Figure 25a shows the resulting bilayer currents generated by all bilayers in response to a single flick of the hair in a direction parallel to the droplet series (i.e., perpendicular to the membranes) at a transmembrane potential of +40 mV. To help visualize this response, a slow-motion animation of the incurred motion of the hair and droplets in this multi-bilayer hair cell assembly is provided in video format in the ESI.

All four interfaces produce nearly synchronized, underdamped currents of about 100 pA or less that decay to the noise level within ca. 0.15 s (Figure 25a). The first bilayer, at the perimeter of the droplet with the hair, generates the largest response, whereas the next three yield currents that are successively smaller in

amplitude in response to the same flick. Integrating the sensing currents across the decay period and dividing each by their respective interfacial areas [172] allows for comparing the average responses of each successive interface in the series at a fixed voltage level; as shown in Figure 25b bilayer 1 exhibits a net charge displacement of ca. 14.8 pC/mm^2, whereas bilayer 4 generates only 2-3 pC/mm^2 in response to a single flick. The data points in this plot correspond to the displaced charge for each bilayer in a 5-droplet series averaged across identical measurements on three separate arrays; the response for each bilayer

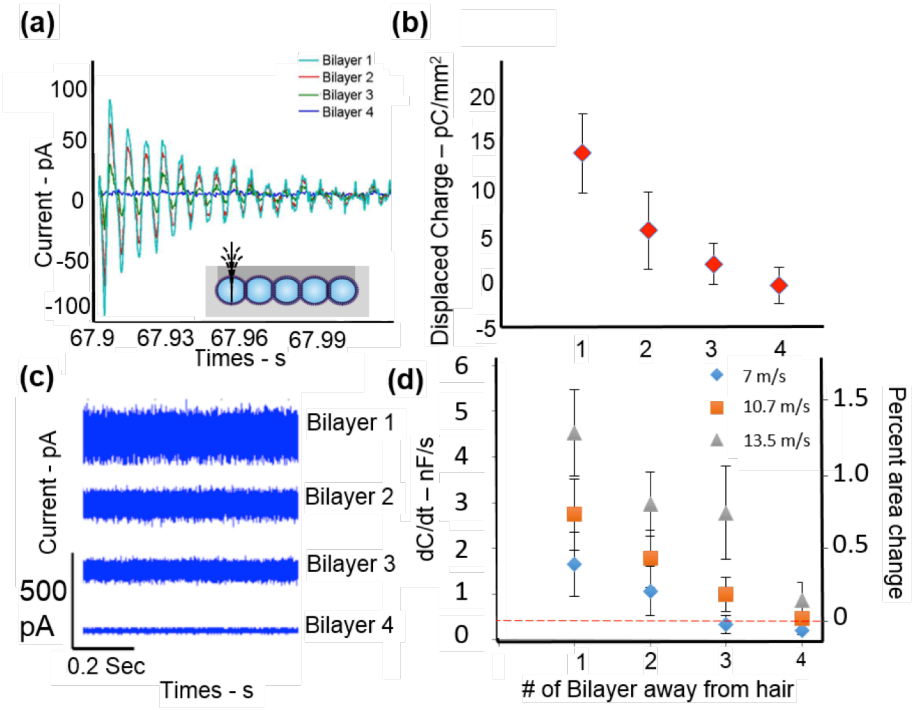

Figure 25: (a) Current response of each bilayer in the array after one flick of the hair. (b) Displaced charge of each bilayer at transmembrane voltages of +40 mV. (c) Raw current response of each bilayer in the array under airflow at 7 m/s and +40 mV transmembrane potentials. (d) RMS current of each bilayer at transmembrane voltages of +40 mV.

in a given array represents the average response to 10 hair flicks at +40mV bias. The error bars represent ± 1 standard deviation of displaced charge for the three separate arrays (*n*=3). Similarly, Figure 25c shows that the membrane closest to the hair (i.e., bilayer 1) produces the largest amplitude of current, while the interface farthest from the hair (i.e., bilayer 4) again produces the smallest response to airflow across the tip of the hair. Like with a single bilayer DIB [3, 172], these sensing currents are functions of the third power of voltage as described by Equation 1. Furthermore, plotting the power spectral density (PSD) of each current signal computed using Welch's method in MATLAB shows that all membranes vibrate at the same frequency (158Hz), which we have previously shown to correspond to the first natural bending frequency of the cantilevered hair [172].

Figure 25d specifies that measuring sensing currents across each of the four membranes at varying voltages (+20, +40, +60, +80, and +100 were used here) can be used to estimate the time rate change in capacitance of each interface in the array. Using this approach, we determine values of *dC/dt* from RMS current measurements for all four membranes in the array for three airflow speeds across the hair. Figure 25d shows that, like the raw current traces, the time rate change in capacitance decreases with distance away from the hair. Here, the data points and error bars represent the average *dC/dt* (and % area change) ± 1 standard deviation, respectively, for each bilayer determined from measurements at 5 different transmembrane voltages (required for computing dC/dt) and averaged across *n*=3 separate 5-droplet arrays. Tests were performed

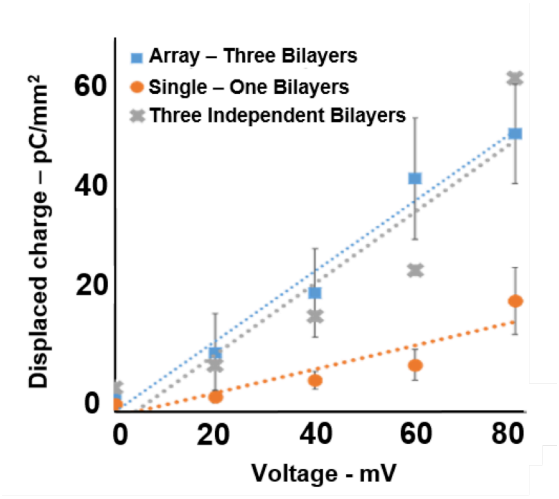

Figure 26: The total displaced charge versus voltage for three different sensor embodiments: 1) an asymmetric 4-droplet, 3-bilayer serial array (blue); 2) a 2-droplet, single bilayer hair cell (orange circles); and 3) the sum of 3 separate single bilayer hair cell sensors (gray squares) estimated by multiplying the output of the single-DIB sensor by three.

identically at 3 different airflow speeds. Consistent with single membranes [172], we also observe that faster airflow yields higher values of *dC/dt* (left axis) for all bilayers, corresponding to higher percentage changes in membrane area (right axis) [172]. For example, the bilayer closest to the hair exhibits a *dC/dt* of approximately 4.5 nF/s and a maximum change in membrane area of approximately 1.3% when airflow at 13.5 m/s is applied to the hair, compared to ca. 2.9 nF/s and 0.7%, respectively, for airflow at 10.7 m/s.

As a result, these data demonstrate that multiple membranes in a droplet array are capable of performing mechanoelectrical transduction of hair motion via membrane bending. The magnitudes of current response, as expected, show that membranes closer to the moving hair result in larger capacitive currents due

to greater amounts of bending, whereas membranes farther away generate smaller responses. The observed decay in sensing response is likely due to the viscous damping in the system that dissipates the strength of the propagating pressure front originating in the liquid from the moving hair. Exponential fits to find the decay rates of displaced charge in Figure 25b or dC/dt in Figure 25d shows that the decay rate generated signal is independent of the voltage and stimuli strength. The decay rate of displaced charge induced by flicking at three different transmembrane voltages is -0.59 ± 0.13 pC/mm^2/bilayer. Moreover, the average decay rate for airflow-induced *dC/dt* at three different air speeds is found to be -0.36 ± 0.06 nF/s/bilayer.

The data also specifically show that the maximum distance a membrane can be located away from the hair and still elicit a measureable sensing response depends in part on the amplitude of the mechanical input that drives hair motion. In these experiments, the motion of the hair resulted in measurable sensing currents up to the 4th bilayer in the series. As is shown in Figure 25d, the measured values of *dC/dt* at 7 and 10.7 m/s airflow speeds are barely detectable above the baseline level determined in control experiments with no airflow. Therefore, bilayers that would be located farther away in a longer droplet series are likely insensitive to hair motion in the current sensor embodiment.

Not surprisingly, the membrane positioned closest to the hair was also consistently the first to rupture in the array upon further increases in airflow speed. We found this response is a function of both the applied airflow speed

and the applied voltage level. For example, in separate experiments the membrane closest to the hair ruptured when we applied |120 mV| at 7 m/s airflow, |100 mV| at 10.7 m/s airflow, and |80 mV| at 13.5 m/s, respectively. These boundaries indicate that both the dynamic range of operation and the minimum sensing threshold are tied to the ability to transmit and withstand mechanical vibration along the droplet series.

To compare the total displaced charge (in response to hair flicking) produced by a single-DIB membrane sensor versus those obtained here with a multi-bilayer hair cell, we plot the total displaced charges in an asymmetric 4-droplet, 3-

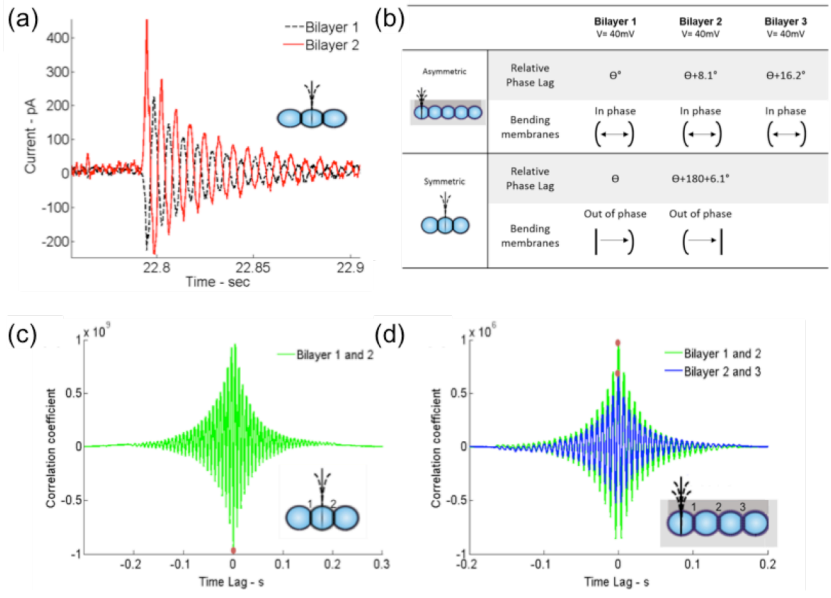

Figure 27: (a) Measured sensing currents of both bilayers in a three-droplet array i response to flicking a hair positioned in the middle droplet. (b) Table of phase analysis c sensing currents and membrane bending in asymmetric and symmetric serial arrays Phase correlation coefficient versus time lag of membrane currents for symmetric (c and asymmetric (d) hair cell array configurations. The red circle in both plots marks th location of the largest amplitude coefficient.

membrane hair cell sensor array versus that for a single membrane sensor (Figure 26). This result shows that the response generated by the one-hair, 3-membrane sensor is considerably larger than that of a one-hair, single bilayer sensor. We are also interested to compare the sensing response generated by an equal number of bilayers arranged in separate single-DIB hair cell sensors to the total current (sum of individual bilayer currents) from the 4-droplet, 3-membrane serial array. Figure 26 reveals that a 4-droplet, 3-interface serial array produces a similar magnitude of displaced charge to that estimated for three separate single-bilayer hair cells sensors.

4.4.2 Phase of the Sensing Currents with Respect to Hair Motion

In addition to understanding the magnitudes of sensing response by adjacent bilayers, we seek to understand how hair placement in an array affects the relative timing, or phase angle, of bilayer currents. Figure 27a shows the transient bilayer currents recorded at equal transmembrane potentials of +40 mV for all bilayers in a *symmetric* 3-droplet, 2-bilayer array when a hair placed in the central droplet is flicked. This response is compared to that of the first 3 membranes (counted left to right) in the 5-droplet, 4-bilayer array with a single hair inserted into the leftmost droplet shown in Figure 24a —referred to in this section as the *asymmetric* array due to the asymmetric position of the hair. We observe that for both series hair motion induces a current response at every membrane. This result shows that bilayers positioned on the same side of the excited droplet (Figure 24a) or symmetrically on both sides of the excited droplet

(Figure 27a) transduce vibrational energy from the hair with the amplitude being a function of distance from the hair. The slight differences in the amplitudes of current produced by both adjacent membranes in the symmetric array may be due to differences in their areas or because of variations in membrane orientation relative to the motion of the hair [203].

The more apparent difference between the transient responses of these droplet arrays is that the sensing currents for the asymmetric 3-bilayer array appear to occur in synchronization, while the measured currents for the two bilayers positioned symmetrically on opposite sides of the hair are out-of-phase with each other (Figure 27a). We performed cross-correlation analyses of these signals using MATLAB to quantify the time delays between sensing currents of adjacent membranes in both systems. The coefficients versus lag times for cross-correlations performed between membrane currents for both the 2 bilayers of the symmetric array and the 3 membranes of the asymmetric array are plotted in Figure 27 c,d. The delay time between current responses is determined by locating the lag time corresponding to the largest absolute value of correlation coefficient. Positive coefficients indicate that the signals are in-phase with one another (i.e., positive correlation), and negative coefficients indicate the signals are out-of-phase, where an increase in one signal corresponds to a decrease in the other (i.e., negative correlation). The data shown in Figure 27b summarize that currents produced by all three bilayers in the asymmetric array are positively correlated with a time lag of 0.18 ms. In other trials (not shown), multiple membranes aligned on the same side of the hair again exhibited positive

correlations, indicating that currents are nearly “in-phase”. The small time lag per successive droplet interface averages between 0.18 and 0.20 ms, which for vibration of the hair 158 Hz, corresponds to a phase angle of ca. 8.1°. Separately, cross-correlation analysis of the two bilayers for the symmetric 3-droplet, 2-bilayer array showed a negative maximum correlation coefficient at a time lag of 0.13 ms, confirming quantitatively that the currents are 180° ± 6.1° “out of phase” (Figure 27b).

This information provides insight into the relative motions of the multiple membranes in each array during hair perturbation. Recall that the current produced by a membrane is a function of both the applied voltage and the *dC/dt* caused by transverse bending of the bilayer during vibration [4]. Thus, the sign of the sensing current from a given membrane depends on both the sign of the transmembrane potential and whether bending produces a positive or negative time rate of change in capacitance. In these experiments, positive bilayer current is defined as that which flows in the direction of decreasing potential. Because all membranes are biased with a positive potential, negative current instead results from decreases in *dC/dt*. Because the membranes in an asymmetric array yield currents that are nearly “in-phase” for voltages of equal sign indicates that they experience deformations that are also nearly in-phase. Because our previous studies [4, 172] have shown that transverse membrane bending is the primary mode of deformation, we interpret a positive *dC/dt* to correspond to an increase in bilayer curvature (and thus surface area). A negative *dC/dt* value in an oscillation cycle, conversely, corresponds to when the membrane flattens. Using

this process, we conclude that the “in-phase” currents produced by the asymmetric array indicate that these interfaces experience increases and decreases in curvature together with minor phase delays due to viscous damping. This same analysis also suggests for the three-droplet symmetric array that one membrane becomes more curved while the other loses curvature. The missing detail in this process is whether interfaces that respond “in-phase” with one another experience curvature in the same direction, The schematics in the table in Figure 27b summarize how the phase differences in sensing currents relate to the relative deformations of the bilayers in serial arrays.

4.4.3 Distinguishing Perturbations of Separate Hairs In A Serial Array

Because vibrational energy dissipates with distance, a larger array of droplets may need multiple hairs to effectively distribute a perturbation to the network or locally excite specific membranes. Thus, we consider a variation of the original 5-droplet, 4-bilayer array shown in Figure 24a, which now includes a second, 12 mm hair inserted into a different droplet. Different lengths for the two hairs are intentionally selected to separate their characteristic frequencies of vibration. We used two hairs of different lengths to examine the frequency selectivity of a multi-bilayer DIB array. This system was comprised of four droplets connected in series to form three bilayers, with hairs placed in the end droplets as shown in the inset in Figure 28b. A 5-droplet series was not used since the fourth bilayer in a series was shown to produce minimal response to flicking (Figure 2a). Per the inset in Figure 28a, the flicker bends and releases the shorter hair in the fourth

droplet and then flicks the longer hair located in the first droplet. Figure 28a also shows the currents generated by each lipid membrane in response to the two flicks. As shown by the arrows in this figure, the first set of underdamped current responses is due to perturbation of the shorter hair, while the second series of responses are generated when the flicker strikes and releases the longer hair. The largest current from the first flick comes from bilayer 3, which is positioned nearest to the shorter hair, and the smallest current comes from bilayer 1, which is the farthest bilayer from this hair. In contrast, bilayer 1 produces the largest

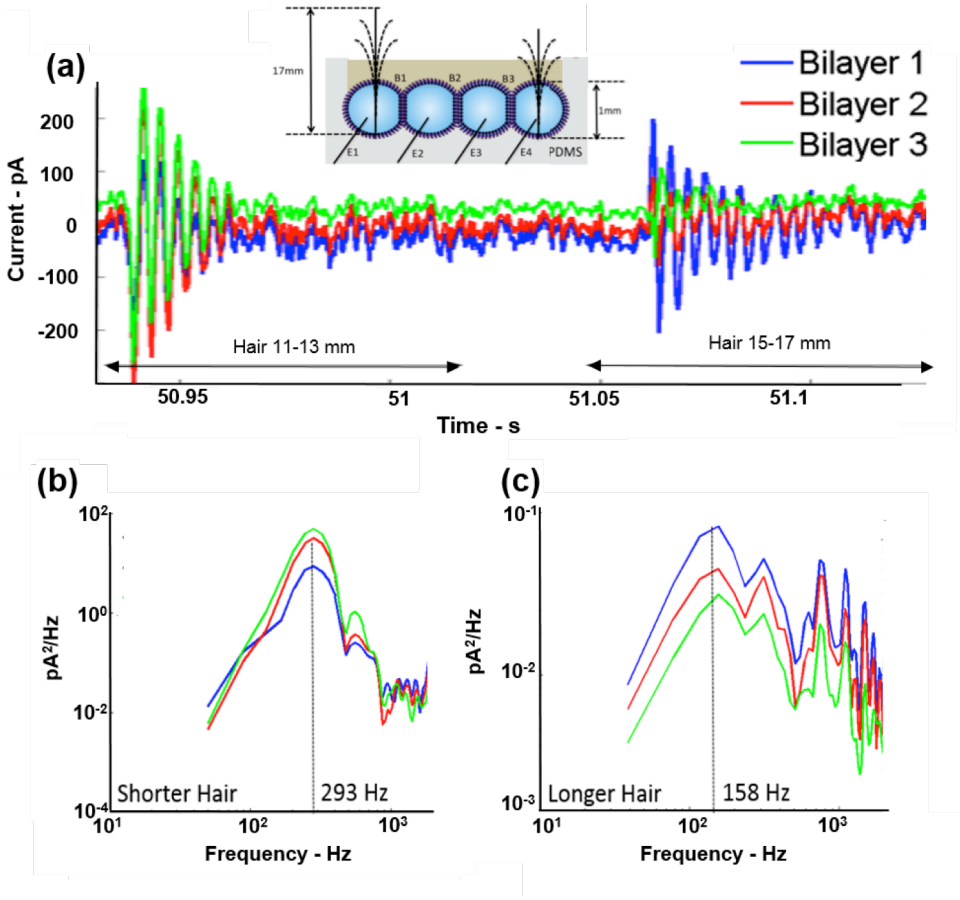

Figure 28: (a) Currents of three bilayers in response to flicks of a short and then long hair. PSDs of the currents produced by flicking the 15–17mm hair (b) and the 11–13mm hair (c).

current and bilayer 3 generates the smallest response when the flicker perturbs the longer hair. In addition to spatial differences, we observe in Figure 28a that flicking the shorter hair produces larger currents from all three membranes than when the longer hair is perturbed. This difference is explained by the shorter hair's higher bending stiffness, which allows it to transmit more energy into the adjacent droplets upon flicking.

Power spectral densities (PSDs) of these same sensing currents reveals a predominant peak frequency at 293 Hz in all three currents when the shorter hair is flicked (Figure 28b) and a separate peak at 158 Hz in all three signals when the longer hair is flicked (Figure 28c). The higher frequency peaks (>800 Hz) in the spectrogram correspond primarily to harmonics of 60 Hz noise. These results confirm that membrane vibration is driven by hair motion, and they provide proof that all three bilayers in the array are able to respond to motion by either hair. Recall, the natural frequency, ω_n, of a cantilever beam in bending is given by

$$\omega_n = \alpha_n^2 \sqrt{\frac{EI}{ml^4}} \qquad \textbf{Equation 22}$$

where, E is the elastic modulus, I is the cross-sectional area moment of inertia, m is the mass per unit length, and l is the length of the beam. This equation shows that the natural frequency of a cantilever beam is inversely proportional to its length squared. Thus, the ratio of natural frequencies for hairs that differ only in length are given by:

$$\frac{\omega_l}{\omega_s} = \frac{l_s^2}{l_l^2} \quad \textbf{Equation 23}$$

The subscripts *l* and *s* are used to denote the longer and shorter hairs, respectively. Comparing the ratio of measured peak frequencies (158 and 293Hz) to the ratio of the squares of hair lengths (17 mm and 12 mm, respectively) as given by Equation 3 shows that they have very similar values (0.54 and 0.50, respectively) and confirms that both hairs respond as cantilevered beams in the system. While the oil and water droplets also likely contribute to the measured natural frequencies of the sensing currents, the fact that the frequency content of the bilayer currents are directly related to the natural frequencies of the hairs shows that multi-bilayer arrays can be used to provide frequency selectivity by tuning the natural frequency of the hair. In summary, this experiment shows that the relative magnitudes and characteristic frequencies of bilayer sensing responses can be used to distinguish motions of multiple hairs in an array, which could be used to investigate differences in perturbation timing and direction.

4.5 Conclusion and Contribution

In this chapter for the first time, serial arrays of lipid-coated droplets were connected to create a multi-bilayer hair cell sensor featuring one or more hair structures. In this manner, multi-bilayer DIB networks resemble the membrane-divided compartments native to living cells. This finding was confirmed by measuring the individual bilayer currents across all interfaces in the array.

Bilayers positioned closest to the hair generate the largest capacitive currents, while those positioned farther away generated lower outputs. The reduction in currents across successive interfaces shows that energy is dissipated in the system, likely in the form of viscous damping, both in the droplets and in the surrounding oil reservoir. Our experiments also showed that a serial DIB array produces a similar total sensing response to that predicted for several single DIB hair cell sensors.

Different length hairs in the hair cell sensor produced currents with different characteristic frequencies, which we used to show how the motion of the hair induces current in every membrane of a serial array and how hairs rooted in the PDMS substrate act as cantilevered beams in free vibration. Inserting multiple hairs of different lengths into different droplets in the array yields sensing currents that exhibit multiple characteristic frequencies in addition to location specific current intensities, features that can be used to spatially localize mechanical perturbations. Also, shorter, stiffer hairs produced larger bilayer currents than longer, more compliant hairs. The fact that bilayer currents decay at successive interfaces away from the hair enables stimulus localization in arrays with multiple hairs.

In this chapter we gained a better understanding of a) how a single hair creates vibrations that propagate across several droplets and b) how the placement of the hair affect the sensing signal and relative motion of membranes in arrays of connected droplets. While the array of hair cell sensor showed the great potential

to achieve higher sensitivity and frequency selectivity in droplet based hair cell transducers, the lipid membranes are still exhibit low durability and small range of airflow operation.

Our next goal in chapter 5 is to assemble and characterize intra-droplet membranes using triblock copolymers, which are known to provide more stable and durable interfaces. In next chapter, for the first time, we will discuss the formation and characterization of intradroplet interfaces using triblock copolymers for achieving even larger durability, stability and range of operation.

CHAPTER 5: REVERSIBLE, VOLTAGE-ACTIVATED FORMATION OF BIOMIMETIC MEMBRANES BETWEEN TRIBLOCK COPOLYMER-COATED AQUEOUS DROPLETS [1]

5.1 Overview

In chapter 3 and 4, we studied durable droplet-based sensors to better understand the mechanotransduction characteristics of single-bilayer and multi-bilayers hair cell sensors. In those studies, we understood different parameters that affect the sensitivity and frequency selectivity in droplet-based sensors such as droplet material compositions, hair properties and placement, voltage across the membranes and sensing performance. While these droplet based systems exhibited a great potential for sensing applications, the membranes still exhibit a low stability under larger airflow or high electrical potential [204]. The goal in this chapter is to develop and characterize interfaces between droplet formed by polymers instead of lipids. In this work we also study the effect of solvents on properties of these membranes

5.2 Introduction

Biomimetic membranes assembled from block copolymers attract considerable interest because they exhibit greater stability and longetivity compared to lipid bilayers, and some enable the reconstitution of functional transmembrane

[1] Note: This chapter presents findings reported in a recent journal paper submitted in Soft Matter - RSC Publishing - Royal Society of Chemistry entitled, “Reversible, voltage-activated formation of biomimetic membranes between triblock copolymer-coated aqueous droplets in good solvents”.

biomolecules (explained in detail in section 1.2.3). Yet to-date, block copolymer membranes have not been achieved using the droplet interface bilayer (DIB) method, which uniquely allows assembling single- and multi-membrane networks between water droplets in oil. Therefore we are interested to understand the formation and the properties of these membranes in droplet-based systems for sensing applications. In this chapter, we investigate the formation of poly (ethylene oxide)-b-poly(dimethyl siloxane)-b-poly(ethylene oxide) triblock copolymer stabilized interfaces (CSIs) between polymer-coated aqueous droplets in alkanes and silicone oil.

5.3 Methods and Materials

Five oil compositions are used in this study: n-decane, n-hexadecane, AR20 silicone oil, a 3:1 (v:v) mixture of hexadecane and AR20, and a 1:1 (v:v) mixture of hexadecane and AR20. All solvents, sodium chloride (NaCl), 3-(N-Morpholino)-propane-sulfonic acid (MOPS), sodium hydroxide (NaOH), and agarose (A9539) are acquired from Sigma Aldrich. PEO-b-PDMS-b-PEO (2kDa-b-2kDa-b-2kDa, P7300-EODMSEO) triblock copolymer is obtained from Polymer Source Inc. 1,2-diphytanoyl-sn-glycero-3-phosphocholine (DPhPC) phopspholipid is obtained as a lyophilized powder from Avanti Polar Lipids, Inc.

Copolymer-stabilized droplet interfaces are created between adjacent 200nL droplets of aqueous buffer placed in a copolymer-oil mixture, or using the droplet-on-hydrogel bilayer method [205] for forming a gel-supported CSI (see Chapter

2). For each oil type, PEO-PDMS-PEO triblock is incorporated into the oil at a concentration of 4 mg/ml, vortexed, and then stirred on a magnetic hot plate at a temperature of >60°C to facilitate complete dissolution of the polymer. The application of heat ensures that the PEO end-blocks remain above their transition temperature (~30°C), as evidenced by obtaining a clear, homogeneous polymer-oil mixture. For comparison, DPhPC DIBs are formed in hexadecane between droplets containing 2mg/mL small (~100nm) unilamellar DPhPC liposomes in aqueous buffer prepared via extrusion as described elsewhere 45. Aqueous buffer used in CSI and DIB experiments is 100mM NaCl, 10mM MOPS, balanced to pH 7.4 via titration with an identical solution supplemented with 0.5M NaOH. Buffer pH is verified using a Fisher Scientific Accumet pH probe. Liposome solutions are stored at 4°C and are used within 2-3 weeks of preparation. Liposome-free aqueous buffer and polymer-oil solutions are stored at room temperature (23°C), and polymer-oil solutions are reheated before tests to ensure complete dispersion of polymer in the oil phase. Note that only reported values of rupture potential for DPhPC DIBs in hexadecane are measured herein. All other reported values of DPhPC DIBs, including specific capacitance, thickness, contact angle, and monolayer and bilayer tensions, were sourced from prior studies by our group [157, 206], that contained higher numbers of trials. All DIB and CSI tests are performed at room temperature.

Electrical measurements and optical imaging are used collectively to assess adhesive interfaces between lipid- and copolymer-coated aqueous volumes in oil. The application of voltage and measurement of current across CSIs and DIBs

are made using wire-type silver/silver chloride (Ag/AgCl) electrodes.Electrodes for DIB measurements are ball-ended as described elsewhere, whereas those for most CSI measurements lack a ball-ended tip and hydrogel coating, since these features complicate insertion of electrodes into polymer-encased droplets where a monolayer forms rapidly. In these experiments positive current represents flow of electrons into the headstage, however measurements are performed only at positive biases due to symmetric membrane compositions in all tests. Droplet positions are controlled with the technique explained in 2.1.3 and 2.1.4.

5.4 Copolymer Stabilized Interfaces

In this work we present the formation and characterization of fully reversible, voltage-activated copolymer stabilized droplet interfaces—which we refer to as

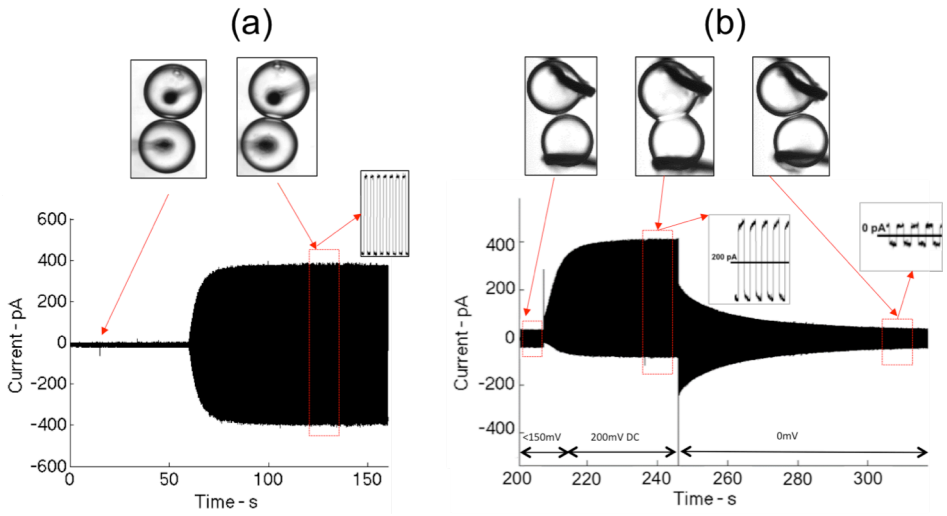

Figure 29: (a) Spontaneous thinning of a DPhPC DIB in hexadecane. (b) Voltage-induced thinning of a CSI in a 1:1 (v:v) hexadecane:AR20 mixture. Droplet diameters are ca. 700-800 µm.

copolymer stabilized interfaces (CSIs)—assembled between aqueous droplets coated in a monolayer of triblock copolymer molecules. The ABA triblock copolymer used in this work consists of poly(ethylene oxide) (PEO) end groups with a poly(dimethylsiloxane) (PDMS) middle group. Our results show that unlike previous efforts to form planar triblock membranes using a *poor* solvent for the copoylmer hydrophobic block [117, 121], the incorporation of PEO-b-PDMS-b-PEO into a *good* solvent for the middle block does not result in spontaneous membrane thinning and droplet adhesion. However, stable droplet adhesion and film formation is achieved when a voltage-induced compression is used to drive excess solvent from the hydrophobic regions of opposing triblock monolayers. Unlike spontaneous droplet adhesion, voltage-induced thinning is fully reversible; removing the applied voltage allows the droplets to completely separate as solvent returns to the region between droplets.

The following sections present our study of the mechanism of reversible CSI formation between water droplets placed in various *good* solvents. Specifically, we perform mutiple experiments with the same copolymer dispersed in multiple organic solvents to investigate the role of solvent exclusion. For each, we determine the minimum voltage required to initiate membrane thinning, and we utilize a combination of electrical measurements and imaging to characterize multiple physical properties of the resulting copolymer stabilized interfaces. Using techniques developed recently by our group with lipid-based DIBs [157], we measure the specific capacitance and electrowetting response of CSIs to determine the hydrophobic thickness and lateral tension of the membrane,

respectively. These data allow us to investigate structural differences between lipid-based DIBs and CSIs assembled in various oils, and our results show that planar copolymer membranes are considerably thicker than lipid DIBs due to solvent retention and polymer midblock length. Additionally, we observe that CSIs exhibit increased resistance to rupture during physical perturbation and significantly higher rupture potentials compared to DIBs. Simultaneously, CSIs also exhibit similar magnitudes of membrane resistance to ion transport as lipid bilayers even though they can exist in a significantly lower tension state when formed in a silicone oil-based solvent. Thus, the ability to prevent coalescence/mixing between aqueous volumes and be reversibly connected and disconnected with voltage provides a new approach for membrane-based smart materials and reconfigurable droplet-based assays.

5.5 Voltage-induced Adhesion of Triblock-coated Droplets Placed in a Good Solvent

CSIs and DIBs between adjacent aqueous droplets are prepared using a similar procedure with only very minor differences. In both CSI and DIB cases, aqueous droplets are pipetted into a less-dense nonpolar solvent and allowed to incubate for a short period of time (<30 s for droplets in copolymer-oil mixtures versus 2-5 min for liposome droplets in oil [207]) to allow the amphiphiles time to self-assemble into monomolecular layers at the water-oil interfaces. Each adsorbed copolymer molecule is believed to be arranged in a looped configuration, i.e., with both hydrophilic endblocks in water and the hydrophobic midblock looping

out into the oil. However, once droplets are brought into contact, the two systems show significant differences. Lipid-coated droplets (Figure 29a) spontaneously adhere upon the exclusion of excess solvent from between opposing lipid monolayers, as reported in the extensive literature on DIBs[51]. Spontaneous thinning and subsequent growth of the lipid bilayer increases the interfacial electrical capacitance which results in a measurable increase in the amplitude of the squarewave current (Figure 29a). We also observe a brighter, planar connection between adhered droplets (right inset) that is different from what is seen in adjacent, but disconnected droplets prior to the capacitive current increase (left inset). A 10 mV amplitude triangular voltage waveform is applied continuously to induce the squarewave current necessary for measuring

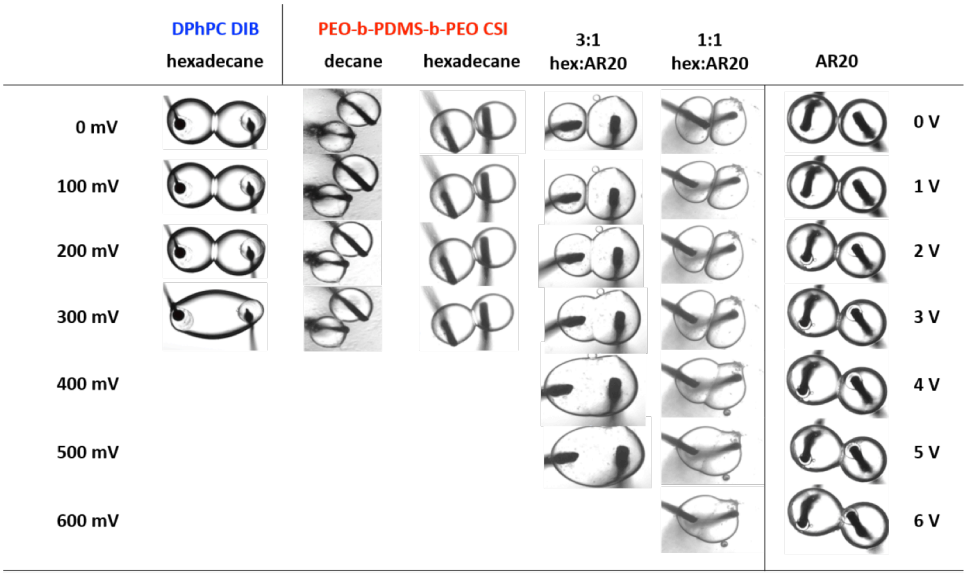

Figure 30: DPhPC DIB versus voltage-induced CSI formation and rupture in different oils. Droplet diameters are ca. 700-800 µm (200 nL).

interfacial capacitance, however, it is important to note that adhesion between lipid-coated droplets in hexadecane occurs even in the absence of electrodes and applied voltage. In contrast, PEO-b-PDMS-b-PEO-coated droplets in a 1:1 (v:v) mixture of hexadecane and AR20 silicone oil (as used elsewhere[168] to minimize density differences between the aqueous and organic phase) do not adhere spontaneously when placed in contact. The same result also occurs when aqueous droplets are placed in pure decane, hexadecane, or silicone oil.

Applied voltage can be used to expedite bilayer thinning in lipid-based DIBs. Therefore a voltage difference was applied between non-adhseive copolymer-coated droplets in 1:1 hexadecane: AR20 oil to see if adhesion could be also obtained for this system. The leftmost section of the current trace in Figure 29b corresponds to separated droplets (see left inset image) despite the application of 150 mV (note, voltage was increased incrementally to this level). The background capacitive current in Figure 29b is slightly larger than in Figure 29a due to higher electrical noise during this experiment. In the next section of Figure 29b (middle inset), increasing the voltage from 150 mV to 200 mV results in a sudden significant increase in the amplitude of the squarewave current response. Images obtained simultaneously show that there is a visible interface to accompany the increase in interface capacitance. The middle inset image shows that the droplets are clearly connected, sharing a large planar interface and a larger contact angle between droplets at a voltage of 200 mV. Finally, when the voltage is reduced to 0 mV, the capacitive current returns to its original amplitude and an image of the droplet pair shows that the droplets return to a separated

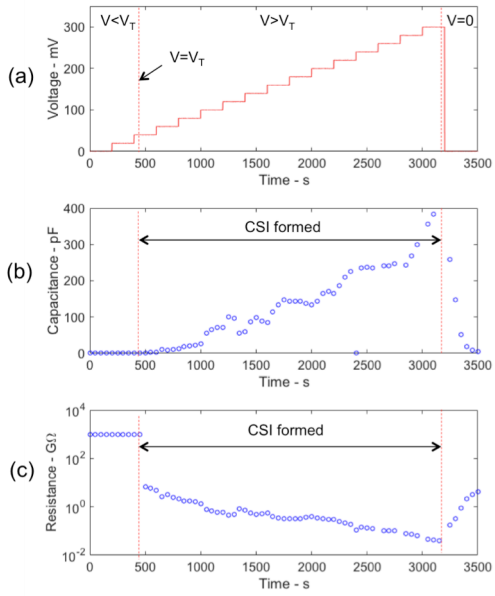

Figure 31: (a) The applied bias voltage and (b) the resulting CSI membrane capacitance and (c) resistance.

state. This process is repeatable (see ESI for video showing repeatable adhesion across multiple CSIs between electrodes), and adhesion could be regenerated by increasing the applied voltage again to above 150 mV. Moreover, the amount of adhesion between droplets can be reversibly varied by modulating the applied voltage at a level greater than the minimum required to drive adhesion (and quantified in the next section). In summary, the voltage activated CSI's are manipulatable and reversible.

Figure 30 shows that this same type of fully reversible, voltage-induced adhesion between droplets is also obtained for triblock-coated droplets placed in *n*-decane, *n*-hexadecane, a 3:1 (v:v) hexadecane:AR20 mixture, and pure AR20 silicone oil, each containing the same concentration (4 mg/mL) of PEO-b-PDMS-b-PEO copolymer. By incrementally increasing voltage in 20 mV steps, we determine

that the average minimum voltage, V_T, required to initiate adhesion between droplets is 166 mV (n = 5) in decane, 83 mV (n = 5) in hexadecane, 179 mV (n = 5) in 3:1 hexadecane:AR20 (n = 5), 371 mV (n = 5) in 1:1 hexadecane:AR20 (n = 5), and >1V (n = 5) in pure AR20. Figure 30 also lists the rupture potential (the voltage at which the interface ruptures causing the droplets to coalesce) for a DPhPC DIB and for CSIs assembled in each solvent. Similar to the threshold potential for adhesion, we obseve that CSIs assembled in oil mixtures containing AR20 silicone oil display higher rupture potentials than those obtained in alkanes. Interestingly, a rupture potential was not reached for applied voltages up to 30 V (the limit of our power supply) for CSIs contained in pure AR20. Further, the rupture potential values for CSIs tested here are all significantly higher than that (212 mV, n = 7) found with DPhPC DIBs formed in hexadecane.

5.6 Quantitative Characterization of Voltage-induced CSIs

5.6.1 Formation of CSI's under Different Types of Oils

A lipid bilayer is commonly modeled as a resistor and capacitor wired in parallel [64]. Therefore, to better understand the structures of CSIs and to evaluate their barrier properties, we measured the squarewave current induced by the sum of a 10 mV, 10 Hz triangle wave voltage and a dc bias varied between the adhesion threshold and rupture potential. Values for nominal membrane capacitance and resistance at each bias level are extracted from the current traces using a custom MATLAB script as described elsewhere [208, 209]. Figure 31 shows an example set of capacitance and resistance data obtained from the induced

squarewave current measured while also applying a sequentially step-wise increasing bias potential (Figure 31a) across a CSI in hexadecane. Reflecting the behavior seen in Figure 29b for separated droplets, we observe that membrane capacitance is negligible and membrane resistance is maximum (our fitting routine permits a maximum value of 1000GΩ) until the bias reaches a value of approximatley ~50 mV. However as applied potential exceeds V_T (t ~ 450s in Figure 31), nominal capacitance begins to increase and nominal resistance exhibits a sharp decrease to a value of ca. 40-50GΩ. The changes in these electrical properties coincide with formation of a planar adhesive connection between the droplets. The data in Figure 31 show that additional increases in the bias potential cause the capacitance and resistance to continue to rise and fall, respectively. Finally, we observe these parameters rebound to the values of C and R observed when $V = V_T$ as the droplets detach upon returning the bias to zero. Resistance does not return to a maximum value of 1000GΩ because of the non-linear nature of the fitting routine, which overestimates values of R prior to initial droplet adhesion.

These data pose interesting questions about the mechanism for changes in both capacitance and resistance as a function of the bias. Specifically, what causes the capacitance to increase: a change in area of adhesion, or a decreasing interfacial thickness, or both? Also, does the reduction in membrane resistance correspond to a voltage-dependent leakage, or is this change driven solely by changes in membrane area? To answer these questions, we performed a separate set of experiments with gel-supported CSIs assembled using the

droplet-on-hydrogel (DHB) method [160, 161, 210]. This approach allows us to accurately image the area of the interface while performing current measurements.

5.6.2 Electrowetting Characteristics of CSI's

Figure 32a shows the visual changes in the adhesive region underneath a gel-supported polymer coated droplet in decane when the voltage is increased from 0 mV to 300 mV; the arrows indicate the perimeter of the adhesive region (i.e., the CSI). Note, the DHB method for CSI formation is utilized here due to the extremely low monolayer tensions of polymer-coated droplets in oil that complicates the calculation of bilayer area using images of adjacent, sagging droplets. Plotting the measured capacitance versus the square of the bias voltage (Figure 32b) shows that the capacitance of the CSI exhibits a sharp increase at the threshold potential (~200 mV) and then increases linearly with respect to voltage squared. This trend is indicative of electrowetting behavior observed at capactive liquid interfaces as has been quantified for DIBs in recent publications [157, 160, 195]. For comparison, the voltage-dependent change in membrane capacitance for a DPhPC DIB (~30% increase) is provided in Figure 32b to emphasize the much larger change (~400%) in membrane capacitance relative to nominal capacitance measured at V_T observed for the CSI. Repeating this experiment for CSIs in different oils shows that normalized membrane capacitance (relative to capacitance at V_T) varies linearly with respect to the square of the voltage difference between the bias potential and the threshold

potential for that oil type (Figure 32c). The slopes of the curves for each oil type in Figure 32c represent the electrowetting constant, α, which describes the voltage-sensitivity of a capacitive interface. The bar graph in Figure 32d compares the average values of electrowetting coefficient for CSIs formed in different oils (n = 3 in each oil) to that for DPhPC DIBs formed in hexadecane. All values range from 10-20 V^{-2}, and the data show that the strength of CSI electrowetting increases with the fraction of silicone oil in the nonpolar solvent

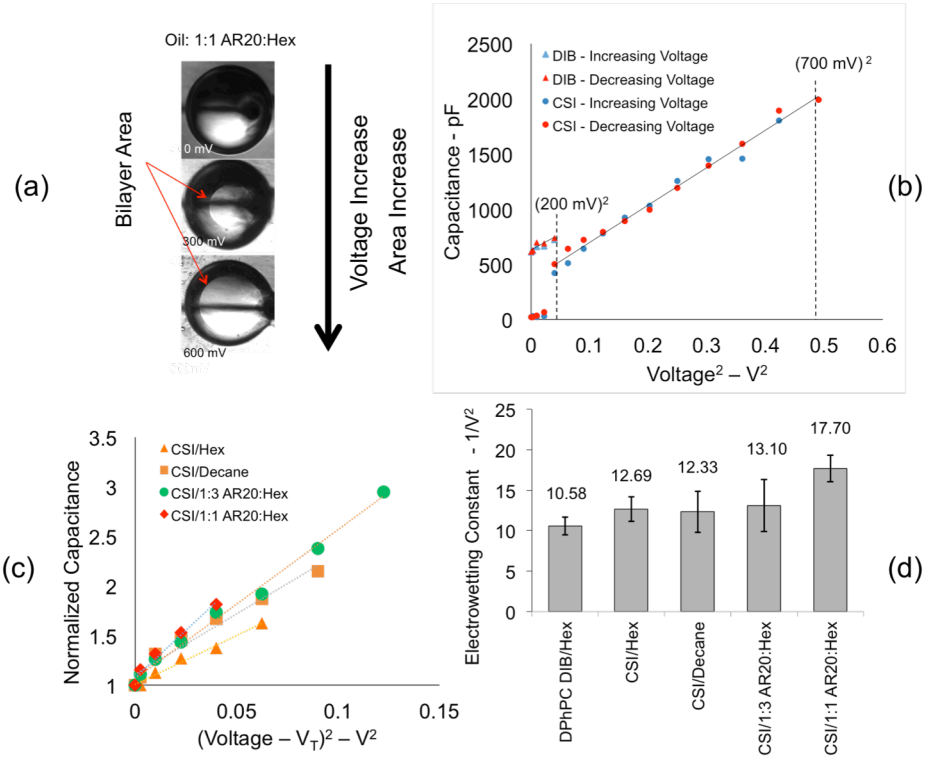

Figure 32: (a) A gel-supported CSI in 1:1 AR20:hexadecane shows the visible growth in adhesive area due to voltage. (b) Nominal capacitance measured on a DPhPC DIB in hexadecane and a CSI in the same oil as (a) versus the square of the applied bias. (c) Normalized capacitance versus change in voltage squared, and (d) the mean electrowetting constant after formation of the membrane for both a DPhPC DIB in hexadecane and CSIs in different oils.

surrounding droplets.

5.6.3 Specific Capacitance and Thickness of CSI's

Figure 33a shows the steady-state capacitance determined from the squarewave current magnitude, plotted versus the optically measured interfacial area of a CSI formed in 1:1 hexadecane:AR20. Unlike lipid-based DHBs which enable control of membrane area by changing the vertical position of the droplet [160, 161, 211], these data reflect variations in membrane area caused by changing the applied bias voltage. Attempts to lift droplets with an electrode resulted in the droplets falling from the probe due to the low surface tension of copolymer-encased droplets. Yet, similar to a DIB [157, 160], we find that nominal capacitance varies linearly with interfacial area. The slope of the capacitance-area curve, which for this oil type has a value of 0.126 μF/cm^2, represents the specific capacitance, C_m, as given by:

$$C_m = \frac{C}{A} = \frac{\varepsilon_r \varepsilon_0}{t}, \qquad \textbf{Equation 24}$$

where ε_r is the relative permittivity of the hydrophobic region of the membrae, ε_0 is the dielectric permittivity of vacuum (8.85x10^{-12} F/m), and t is the hydrophobic thickness of the membrane. Linear relationships between nominal capacitance and interface area are also found for the other oils (not shown; C_m cannot be determined in pure silicone oil due to the voltage limit of our current measurement device). The linearity of these data indicate that for $V>V_T$, voltage-driven increases in CSI capacitance cause the interfacial area to increase at

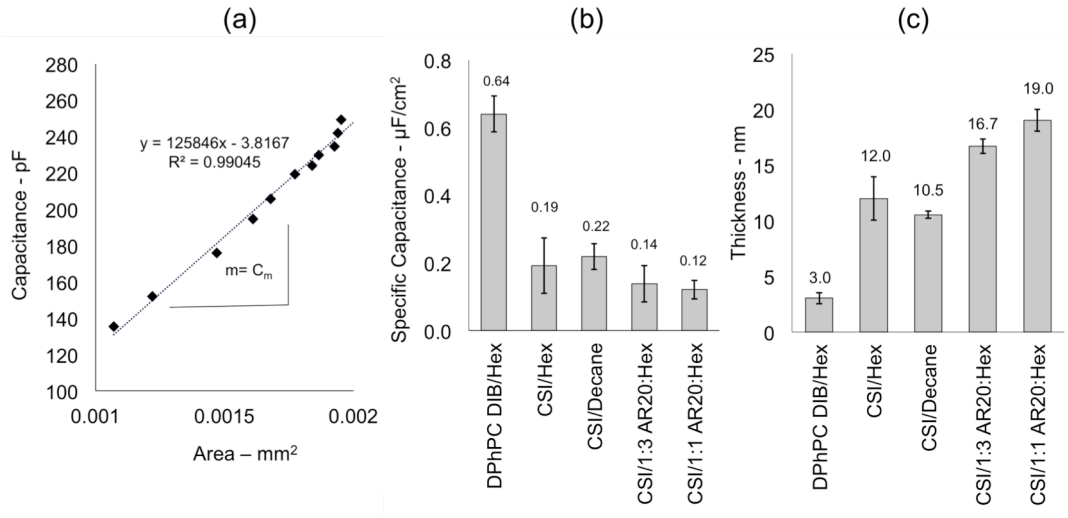

Figure 33: (a) Representative nominal capacitance versus adhesive area data obtained for a CSI formed in 1:1 AR20:hexadecane. This type of data for each interface allows calculation of the average specific capacitance (b) and equivalent membrane thickness (c).

constant hydrophobic thickness. Figure 33b compares the average values of C_m measured for CSIs in various oils. Compared to a DPhPC DIB in hexadecane, CSIs exhibit much lower values of C_m. Moreover, we observe that CSIs formed in oils containing silicone oil exhibit slightly lower values of C_m than those formed in alkanes.

The hydrophobic thickness for each CSI is determined from these values of C_m using Equation 1 and shown in Figure 33c. The calculation is performed by using a value of ε_r=2.6 to describe the dielectric properties of the triblock copolymer interface hydrophobic region (ε_r for PDMS ranges from 2.3-2.8 [212, 213]). It is noted that thinned CSIs may contain some residual amount of solvent as with lipid bilayers [214, 215], and the relative permittivity of alkanes like decane and

hexadecane tends to be closer to 2.2 [216], thus this approximation may slightly overestimate hydrophobic thicknesses (especially in cases where pure alkanes are used, since AR20 and PDMS are expected to both have a dielectric permittivity of ~2.6). Nonetheless, these calculations show (Figure 33b) that the reduction in C_m for CSIs compared to a DIB (ε_r=2.2) is the result of the interface having a considerably thicker hydrophobic region (10 – 20 nm). These data also show that CSIs in alkanes are thinner than those in silicone oil mixtures, which suggests that CSIs formed in alkanes contain less residual solvent upon voltage-initiated adhesion. Measured thickness values also compare well to those predicted for polymer brushes with 100% surface coverage using Flory-Huggins theory [217]

$$L \approx Na \qquad \textbf{Equation 25}$$

where L represents the length of the hydrophobic PDMS middle block extending into the oil, N is the number of PDMS segments, and a is the segment length. A 2 kDa PDMS block consists of approximately 28 repeat units, however we estimate N as being at most 14 segments in length to account for the fact that the copolymer likely resides in a looped configuration in at the oil-water interface. With a value of 0.6 nm for the segment length from literature [218], L is estimated to be 8.4 nm. Therefore, a bilayer formed between co-polymer droplets displays a hydrophobic thickness on the order of ~17 nm. These values (8.4 nm and 17 nm) represent a membrane composed of PDMS chains that are well-packed laterally and maximally extended into the oil. In oils where PDMS is less soluble,

we expect the brush height and total membrane thickness to lower due to the fact that the PDMS block would prefer to reside in a more compact, less swollen state. The differences between the measured values of hydrophobic thickness and the predicted total membrane thickness may also be the result of inclusion of oil in the midplane, which can occur in planar lipid bilayers formed in oil [219].

5.6.4 Electric Field and Membrane Resistance of CSI's

With values of thickness known for CSIs in different oils, we next computed the magnitudes of electric field required to initiate adhesion and cause rupture (**Figure 34**a). These data are again compared to that for a DPhPC DIB, and we see that despite the higher rupture potentials for CSIs, the electric field sustained by a much thinner lipid membrane is approximately 2-3X higher than that which is required to cause rupture in the triblock-stablized interfaces. These results clarify that electrical breakdown, while occuring at a higher nominal voltage, occurs at a considerably lower electric field for CSIs than for DIBs, a result that may stem from differences in molecular packing, compressibility, and mobility of the amphiphiles in the bilayer interfacial region.

Finally, values of area-normalized membrane resistance, R_m are computed by multiplying the measured resistance of a CSI by its respective area (determined by dividing nominal capacitance by C_m) at every bias voltage (Figure 34b). Despite CSIs exhibiting far lower values of nominal resistance (0.2-2 GΩ) than lipid bilayers (10-100GΩ), values of CSI membrane resistance on the order of 20-30MΩcm^2 are quite similar in magnitude to those for lipid bilayers (10-

100MΩcm^2). Additionally, we see that the membrane resistance of each CSI-oil combination is generally constant versus voltage, and thus interfacial area. As a result, we can interpret the decrease in nominal resistance observed in Figure 31c as being due primarily to the increase in area, and not due to voltage-initiated permeation. The permeability of this type of membrane to species other than ions is still largely untested, however a preliminary experiment demonstrated that carboxyfluoroscein does not diffuse through a CSI formed (with $V>V_T$) in a 1:1 mixture of AR20:hexadecane.

5.6.5 Monolayer and Bilayer Tension of CSI's

While the results described thus far show how voltage affects CSI thickness and area, little is known about the organization of triblock molecules and thus the

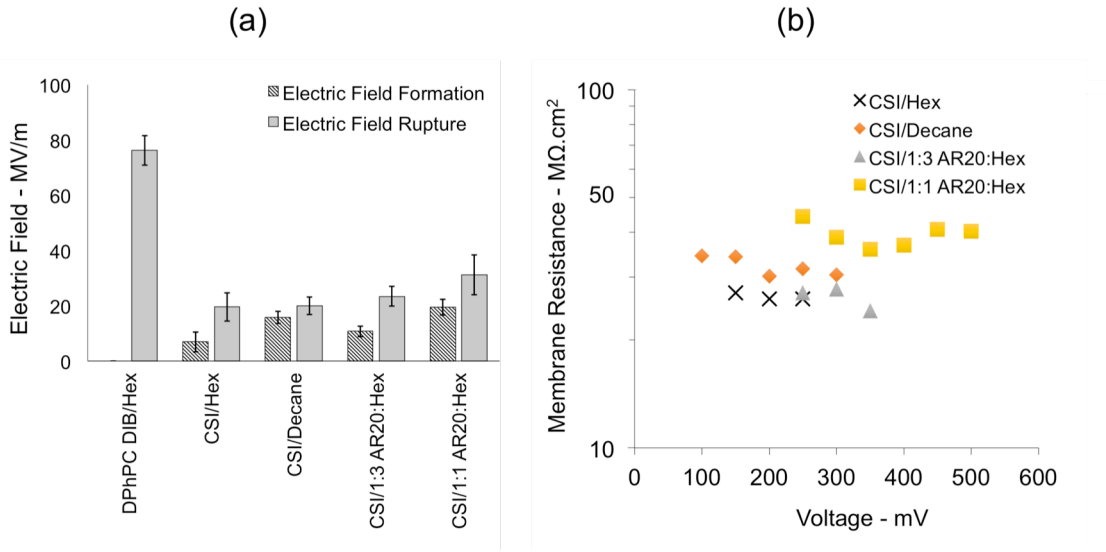

Figure 34: (a) Computed elecric field at both formation and rupture voltages for a DPhPC DIB in hexadecane and for CSIs under different solvents. (b) Membrane resistance versus nominal voltage ($V>V_T$) of CSIs.

tension states for both monolayer and the adhesive interface of a CSI. Knowledge of the monolayer and interfacial tensions of droplet-supported CSIs assembled in different oils would shed light on the mechanism for voltage-initiated adhesion, specifically pertaining to the role of solvent. Ininitally, we attempted to measure the monolayer tension of a triblock-covered water droplet in oil using a pendant drop goniometer. However, we observed the droplet to quickly sag in the less dense oil and then fall from the dispensing tip, which prevented us from being able to determine steady-state monolayer tension using the conventional pendant drop method.

Taylor et al. recently demonstrated that the steady-state monolayer tension of a DIB can be measured by tracking the electrowetting response of an interface for which C_m is known [157]. The method is based on the Lippmann relationship[220] which states that upon application of voltage across the capacitive bilayer interface, bilayer tension, γ_b, is reduced by the magnitude of the energy stored at the interface due to capacitive charging as given by

$$\gamma_{b,0} - \gamma_b(V) = \frac{C_m}{2} V^2 , \qquad \textbf{Equation 26}$$

where $\gamma_{b,0}$ is the bilayer tension at zero volts, C_m is the specific capacitance of the interface, and V is the applied voltage. For adhesive droplets that exhbit a planar interface and an external half contact angle, θ, γ_b is related to the monolayer tension, γ_m, via Young's relationship which is given by

$$\gamma_b = 2\gamma_m \cos\theta \,. \qquad \textbf{Equation 27}$$

For a DIB that forms spontaneously at a zero bias, combining Equations 3 and 4 produces an expression that relates the change in the cosine of the contact angle to C_m, γ_m, and V. However, because CSIs exhibit electrowetting only at non-zero biases, Equations 3 and 4 are rewritten as

$$\cos\theta_{ref} - \cos\theta(V) = \frac{C_m}{4\gamma_m}\left(V^2 - V_{ref}^2\right) \qquad \textbf{Equation 28}$$

to reflect how the cosine of the contact angle changes with respect to θ_{ref}, defined as the external contact angle measured at a non-zero reference bias V_{ref}

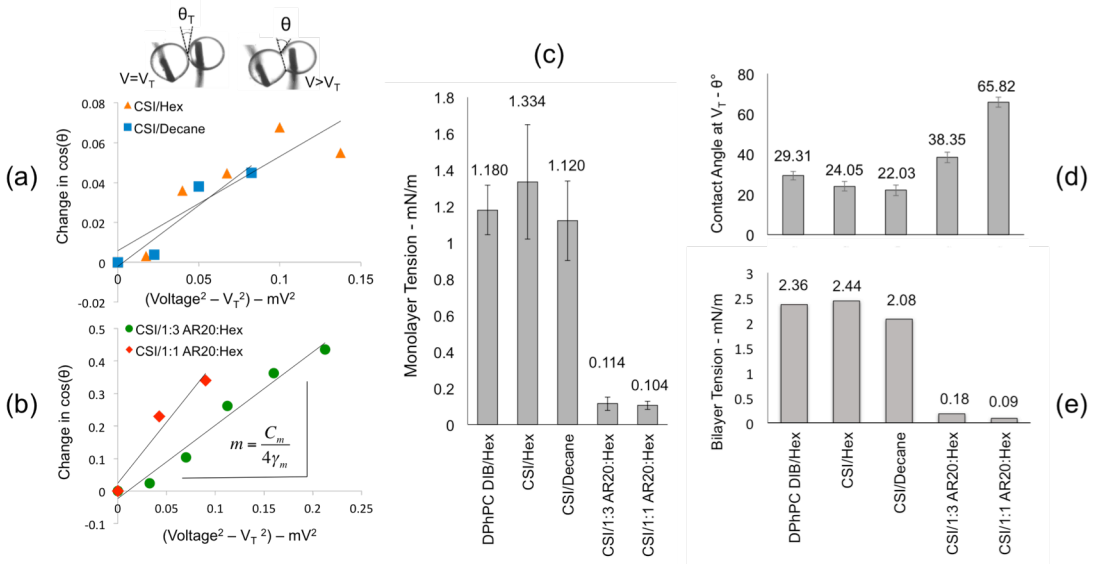

Figure 35: The change in cosine of contact angle versus voltage squared for (a) CSIs in hexadecane and decane, and (b) for CSIs in 1:3 AR20:Hex and 1:1 AR20:Hex. (c) Monolayer tensions, (d) contact angles at the theshold voltage, and (e) computed average membrane tensions for a DPhPC DIB in hexadecane and for all CSIs.

located above the threshold potential.

Since C_m is known for the CSIs in various solvents, Equation 28 and Equation 27, respectively can be used to determine unknown values of γ_m and γ_b by measuring the change in the cosine of θ versus the change in V^2. Therefore, a final series of experiments was performed on CSIs formed between adjacent droplets to investigate how the contact angle between droplets changes with the bias. Figure 35a and b shows representative data for the measured change in the cosine of the contact angle versus (V^2-V_{ref}^2) for CSIs in each oil. The data are plotted on separate axes to account for the difference in scale between the values obtained

for CSIs in alkanes versus those in silicone oil mixtures. All curves display a generally linear relationship between change in cosine of the contact angle and the difference in the square of the applied bias; R^2 correlation coefficient values for all curves are greater than 0.89, and greater than 0.96 for CSIs in silicone oil mixtures. In total, data were obtained from three separate interfaces formed for each CSI-oil combination. With Equation 5 and the corresponding average value of C_m for each CSI-oil (Figure 35a), the slope of each linear regression is used to calculate γ_m. Figure 35c compares the average monolayer tension of CSIs to that measured on a DPhPC DIB. Interestingly, while the monolayer tensions for CSIs in alkanes are similar in magnitude to that for a DPhPC monolayer (~1-1.3mN/m [221]), these data show that copolymer monolayers at a water-silicone oil mixture interface are considerably lower (~0.1mN/m).

Average values for γ_b at V_T are computed for each CSI-oil case via Young's equation (Equation 4). γ_m was computed for each in the previous section, and the contact angle, θ_t, measured at V_T is measured from images taken of adhered droplets after equilibration at V_T. Resulting values of θ_t and γ_b are shown in Figure 35d,e for all CSIs and a DPhPC DIB. As observed with γ_m, these data again show that CSIs in alkanes exhibit membrane tensions (~2.0-2.5 mN/m) similar in magnitude to a lipid DIB, due to both similar values of monolayer tension and contact angle (20-30º). However, CSIs formed in silicone oil mixtures, those which display very low monolayer tensions, have substantially larger contact angles and thus even smaller relative membrane tensions (<0.2 mN/m). The Lippman (Equation 26) and Young (Equation 27) relationships predict that these interfaces reach an even lower tension, which corresponds to a higher contact angle, due to electrowetting at higher biases. This behavior is confirmed indirectly by the increasing contact angle observed with increasing voltage prior to rupture (Figure 30). In fact, some of these interfaces approach an external half angle of 90º, which signifies the membrane reaches a zero-tension state.

These findings confirm why polymer-coated droplets consistently fell from the syringe tip during goniomenter trials (extremely low γ_m), but they also reveal important differences about molecular packing at the interface. Specifically, the difference in tensions for CSIs in alkanes versus silicone oil mixtures suggest that copolymer molecules, likely in a looped configuration at the oil-water interface, are packed more tightly when the solvent contains silicone oil. Building

on analysis by deGennes [222], we interpret the reduced tension and increased thicknesses of CSIs in silicone oil mixtures to confirm that they hydrophobic-PDMS middle block, which likely resides in a looped configuration at the oil-water interface, is extended from the interface but tightly packed in a lateral direction which serves to more effectively minimize the interfacial tension. In alkanes, our data suggest that the molecules are arranged in a more expanded state laterally, and they are also less swollen by solvent and thus shorter in height. Figure 37a shows a qualitative representation of these differences in molecular arrangement.

5.7 Discussion on the Mechanism and Energetics of Reversible, Voltage-Iniated Adhesion

Our experiments highlight key differences between the adhesion behaviors of DIBs and CSIs. DPhPC-coated droplets adhere spontaneously in hexadecane as well as in decane and silicone oil (not shown), confirming that these oils acts as *poor* solvents for the acyl chains of the DPhPC monolayers [137]. In a *poor* solvent, solvent is excluded entropically in favor of creating a solvent-depleted region of contact between droplets. This mechanism causes the area of the solvent-depleted region and the contact angle between droplets to scale inversely with tail solubility in the oil, which has been previously demonstrated elsewhere: DPhPC DIBs formed in dodecane [195], a smaller-molecule solvent in which the acyl chains have greater solubility, have a significantly smaller contact area compared to lipid-coated droplets connected in silicone oil [223].

Like DIBs, polymer-coated droplets in alkane and silicone oil mixtures do not coalesce when placed in contact. However, unlike DIBs, they required a bias voltage to form an adhesive connection, and they fully separate when this voltage is removed. The images and table in Figure 30 highlight that the miminum voltage required to cause adhesion depends on the type of oil surrounding the droplets and that it increases for silicone-based oils versus pure alkane mixtures and with decreasing alkane length (i.e. decane versus hexadecane), a trend that is also observed in lipid bilayers [224]. In a separate experiment, we studied the interactions of droplets coated with PEO-b-PDMS-b-PEO in a mixture of chloroform, hexadecane, and squalene at a volume ratio of 0.1:0.8:3.2. In this sufficiently *poor* solvent, we observed droplets to spontaneously adhere without voltage (Figure 36). The complete characterization of triblock interfaces formed spontaneously in *poor* solvents is currently in preparation.

The corresponding manuscript focuses on CSIs formed in *good* solvents, where applied dc voltage is required to initiate thinning and drive adhesion. We are currently preparing a separate manuscript that describes how CSIs form spontaneously, without the need for applied dc voltage, when a sufficiently *poor* solvent is used in the oil phase. Figure 36a a and b show PEO-b-PDMS-b-PEO and PMOXA-b-PDMS-PMOXA CSIs, respectively, formed in 0.1:0.8:3.2 (v:v:v) chloroform:hexadecane:squalene. Unlike those in good solvents, triblock-coated droplets in this solvent mixture adhere spontaneously without applying voltage. The separate manuscript in preparation will provide fuller description and

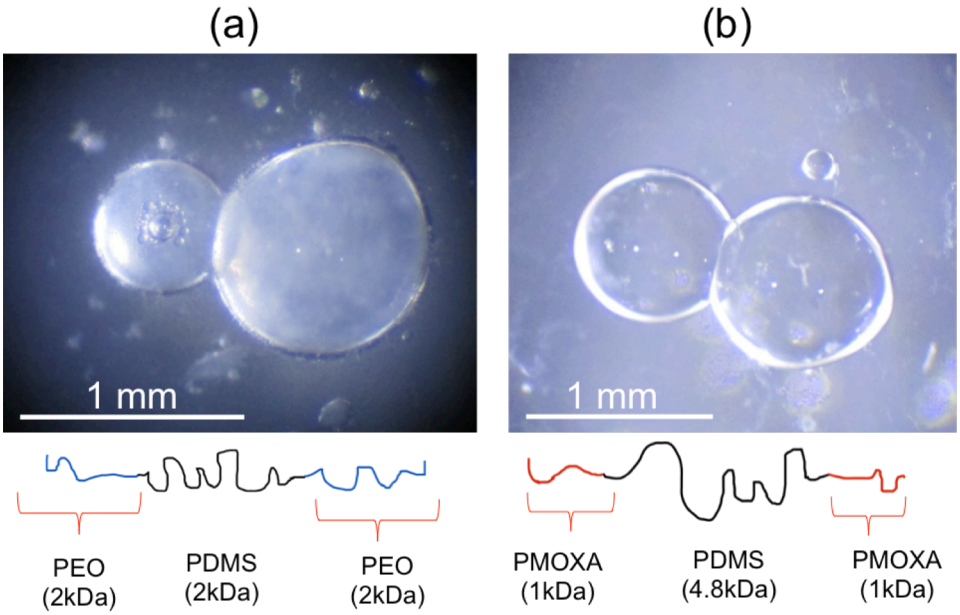

Figure 36: Pictures of spontanous CSI formation (*V*=0) between (a) PEO-b-PDMS-b-PEO-coated droplets and (b) PMOXA-b-PDMS-b-PMOXA-coated droplets residing in a sufficiently poor solvent mixture consisting of 0.1:0.8:3.2 (v:v:v) chloroform:hexadecane:squalene.

characterization of CSI formation in poor solvents. However, as a brief description of the mechanism for spontaneous formation, the poor solvent is excluded entropically from the PDMS chains, enabling attractive van der Waals interactions to drive spontaneous adhesion. When solvent is driven out entropically, there is no disjoining pressure barrier between droplets (as is shown in **Figure 36** for CSIs in *good* solvents) and thus no need for an applied electic field to initiate thinning of the membrane.

Together, these findings demonstrate that the relative solubility of the hydrophobic copolymer middle block in an oil dictates the adhesion response of adjacent triblock-coated droplets. Our understanding of the mechanism of

reversible, voltage-initiate adhesion for triblock polymer-coated droplets immersed in a *good* solvent is explained in the framework of the disjoining pressure. The disjoining pressure for reversible CSI formation in *good* solvent is illustrated in Figure 37b as a function of separation distance, *h*, between two polymer-coated droplets.

As two droplets initially approach one another (at large values of *h*), long-range repulsive interactions develop due to the presence of swollen polymer chains extending into the oil from each droplet surface. These interactions betwen polymer "brush" layers are entropic in nature and stem from a combination of osmotic repulsion interactions between solvated polymer coils which favors their expansion and the energy required to elastically stretch these chains [217]. The net effect is a repulsive barrier that prevents spontaneous adhesion. The application of voltage works to compress the thick interface and acts in opposition to these repulsive interactions, where the magnitude of the electrocompression[225] is given by

$$\Pi(h) = \frac{1}{2}\varepsilon_r \varepsilon_0 \left(\frac{V}{h}\right)^2 . \qquad \textbf{Equation 29}$$

This applied pressure thins the interface through both elastic compression of the chains and through hydraulic exlcusion of solvent from the interface. As applied voltage increases above zero but remains below the voltage threshold for adhesion, the system moves stably up the disjoining pressure curve (from right to left in Figure 37). A critical point is reached as soon as voltage reaches V_T at h_c

in Figure 37, whereupon the interface spontaneously transitions to an adhesive interface like those shown in Figure 36. This metastable point exists at a medium-range, critical separation distance, denoted as h_c, where the electrocompressive forces cancel the long-range repulsive interactions, thereby thinning the interface, such that medium-range attractive van der Waals interactions between the two droplets now become the dominate forces balancing the system. This metastable balance point, denoted as Π_c thus represents the peak of the repulsive barrier before the two droplets transition spontaneously into an adhered state with an equilibrium thickness, h_e (Figure 37b). The onset of adhesion is depicted as a reduction in the net disjoining pressure to a net negative value, and, importantly, is verified experimentally by the observed increase in contact between droplets when the voltage is increased above the threshold. Adhesion can be quantified by measuring or calculating the reduction in free energy per unit area of the system upon the formation of the adjoining interface[224] as given by

$$-\Delta F(V) = 2\gamma_m - \gamma_b(V) = 2\gamma_m(1-\cos\theta_v). \qquad \textbf{Equation 30}$$

Equation 7 is written as a function of the applied voltage to emphasize that membrane tension is a function of applied voltage when electrowetting occurs. Once driven to an adhesive state our measurements of C_m and thickness confirm that increasing the voltage further only changes the area of the interface via electrowetting.

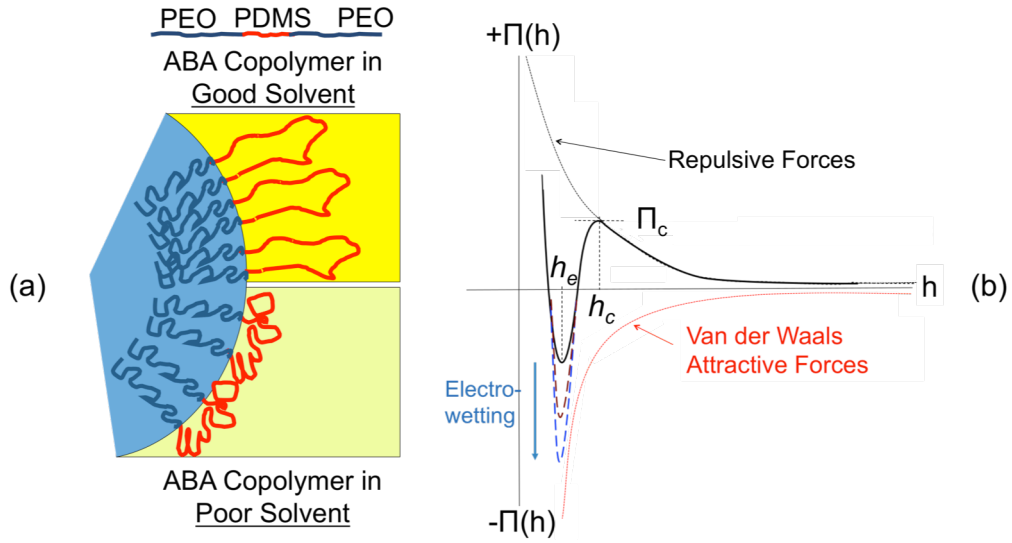

Figure 37: (a) Illustration of conformations of copolymer molecules at the water-oil interface in *good* and *poor* solvents. (b) Qualitative model for the disjoining pressure profile versus separation distance for CSI membranes.

In summary, applying voltage between polymer-coated droplets immersed in *good* solvents provides a positive disjoining pressure to expel solvent and compress the interface. The interface thins stably as the voltage is increased, up to a critical distance at which spontanous, attractive van der Waals interactions drive the droplets together to form an adhesive connection. Unlike recent reports of surfactant coated droplets that were driven together with voltage [225], the interfaces between copolymer-decorated droplets do not coalesce because of tight monolayer packing that results in stabilizing steric interactions between overlapping polymer chains at close distances. In the adhesive state, electrowetting merely causes the area of the interface to vary at constant thickness. Moreover, the process is reversible because the voltage-induced solvent expulsion establishes an osmotic pressure difference, between the bulk oil and the interfacial hydrophobic region, that favors driving solvent back into the

membrane. Thus when the bias is reduced, the voltage-induced pressure lessens, and the compression-induced osmotic pressure causes oil to re-enter the membrane, whereupon chain swelling thickens the interface and pries apart the droplets. This behavior corresponds to traversing the disjoining pressure curve in reverse, where the osmotic pressure provides the work needed to overcome the peak. Hence, the use of voltage to drive adhesion for surfactant-coated droplets in a *good* solvent provides a mechanism for obtaining complete reversibility of contact between adjacent volumes.

The energetics of voltage-initiated adhesion can be quantitatively compared for CSIs in the various oils by calculating the critical disjoining pressure, Π_c, and the free energy of formation, ΔF. While the free energy of formation is related to the disjoining pressure profile, as given by

$$\Delta F = -\int_{\infty}^{h_e} \Pi(h)\, dh \,, \qquad \textbf{Equation 31}$$

Our measurements of interfacial thickness via electrical capacitance are not sensitive to detecting changes in thickness greater than h_c (i.e. prior to droplet

Table 1: Energetics of DIB and voltage-initiated CSI formation

Oil type	V_T (mV)	θ_T (°)	γ_m (mN/m)	h_e (nm)	$\Pi_c(h_e)$ (kPa)	$-\Delta F(h_e)$ (mJ/m^2)	$\Delta F/2\gamma$ (% Reduction)
CSI/Hex	83	24.1	1.32	0.19	1.2	0.23	8.1
CSI/Decane	166	22	1.075	0.22	0.81	0.16	7.4
CSI/1:3 AR20:Hex	179	38.4	0.114	0.14	2.42	0.05	21.9
CSI/1:1 AR20:Hex	371	65.8	0.104	0.12	3.77	0.12	57.7

adhesion). Thus we are unable to convert values of ΔF into disjoining pressure units for the purposes of locating the minimum point in Figure 37b. Additionally, we make the approximation that h_c and h_e are close in value since our measurement of thickness represents h_e. The results of these calculations are presented in Table 1.

Using the mean values of threshold voltage, monolayer tension, contact angle at the threshold voltage, we find that the critical disjoining pressure varies between ~1-4 kPa for CSIs, and it increases with increasing amounts of silicone oil in the solvent and increasing equilibrium thickness. This finding suggests that more pressure is required to exclude a silicone-oil-based organic phase due to the greater solubility of the PDMS block in AR20. This finding is supported by the increased thickness that we computed for thinned interfaces in silicone oil—suggesting that more oil remains even after repulsion is overcome with voltage. For the two alkanes, we see more pressure (and higher voltage) is required to exclude decane compared to hexadecane. This trend is consistent with lipid bilayers formed in alkanes, where smaller molecule solvents tend to be retained in the membrane more due to higher solubility. The inconsistency is the fact that despite a greater barrier to adhesion (suggesting higher solubility of decane in PDMS) our thickness data (Figure 33c) does not indicate a statistically significant difference from that measured for CSIs in hexadecane, which has a lower adhesive barrier. The values of free energy of formation per unit area reflect the decrease in free energy gained by adopting a planar interface with reduced tension between droplets. Larger external contact angles and lower membrane

tensions thus correspond to a greater percentage reduction in free energy per membrane area compared to the energy per unit area (i.e. tension) of polymer monolayers prior to forming the adhesive interface. Thus, CSIs formed in silicone oil exhibit a much larger relative decrease (20-60%) in energy per unit area than those formed in alkanes (~8%), as well as that for a DPhPC DIB in hexadecane (~6%).

5.8 Conclusions and Contribution

To-date planar membranes assembled from triblock copolymer membranes have utilized a combination of *good* and *poor* solvents (typically chloroform—*good* and decane or toluene—*poor*) in proportions that leave the mixture predominantly *poor* for the middle hydrophobic block. This selection has resulted in the spontaneous membrane thinning [117, 118]. In contrast, in this chapter we showed that polymer-stabilized adhesion between droplets in a *good* solvent for the middle block is pressure-dependent and completely reversible, which indicates that there is an initial energy barrier to forming an adhesive interface. We quantified this barrier in the form the minimum applied pressure achieved via electrocompression needed to remove excess oil from between opposing monolayers. The results of these measurements showed that the height of the repulsive barrier to adhesion increases with increasing solubility of the hydrophobic block in the oil; thus, more voltage or mechanical pressure is required to exclude solvent. Characterizations of the thinned interface upon overcoming the barrier to adhesion show that CSIs formed in silicone oil-based

solvents yield thicker membranes that also exist at a lower tension state. These findings are supported by well-known brush theories that predict an increase in brush length and a decrease in area per molecule at the interface for polymers in a good solvent. However, the demonstration of tuning this adhesion between small-volume droplets using voltage offers new capability for both connecting and disconnecting polymer-stabilized aqueous volumes, enabling new forms of tunable modularity in droplet-based microfluidics, voltage-sensitive emulsions, and membrane-inspired material systems.

CHAPTER 6: MODELING MECHANOTRANSDUCTION [1]

6.1 Overview

In this chapter, the goal is to develop a model that captures the entire transduction process to understand the key physical parameters or design variables for the sensing response. This model combines Helfrich theory of membrane deformation and Stokes theory of pendulums moving in fluids to understand how parameters like hair length, membrane stiffness, and membrane capacitance affect the sensing current in response to airflow [2].

We aim to establish an order of magnitude approximation for the sensing current generated by the lipid membrane in response to prescribed airflow to provide physical insights into how single and multiple membrane networks can be used to sense mechanical perturbations. Describing the complete transduction process requires knowing separately: 1) how airflow affects hair motion; 2) how hair motion induces forces on nearby bilayers; 3) how this force drives membrane deformation; and 4) how dynamic changes in deformation state create variations in capacitance that generate current. This model provides physical insights into how membrane-based materials can be used for sensing mechanical stimuli—just like nature does.

[1] Note: This chapter presents findings reported in a recent journal paper submitted in Bioinspiration & Biomimetics - IOPscience entitled, “Toward cell-inspired materials that feel: measurements and modeling of mechanotransduction in droplet-based, multi-membrane arrays”.

6.2 Airflow Induced Hair Motion

Estimating the motion of a small-diameter hair induced by turbulent airflow is not trivial. The theoretical basis for describing hair motion in our transduction model employs Stoke's theory of pendulum motion in a fluid medium [226] to describe how the surrounding fluid augments the total drag and inertia of the hair in addition to acting as a forcing function that induces motion. Several prior studies on modeling the motion of insect hairs [227-229] also utilized Stoke's theory; in this work, we justified the use of a rigid-body model for hair motion based on observations that these insect hairs rotate and do not bend when perturbed. The

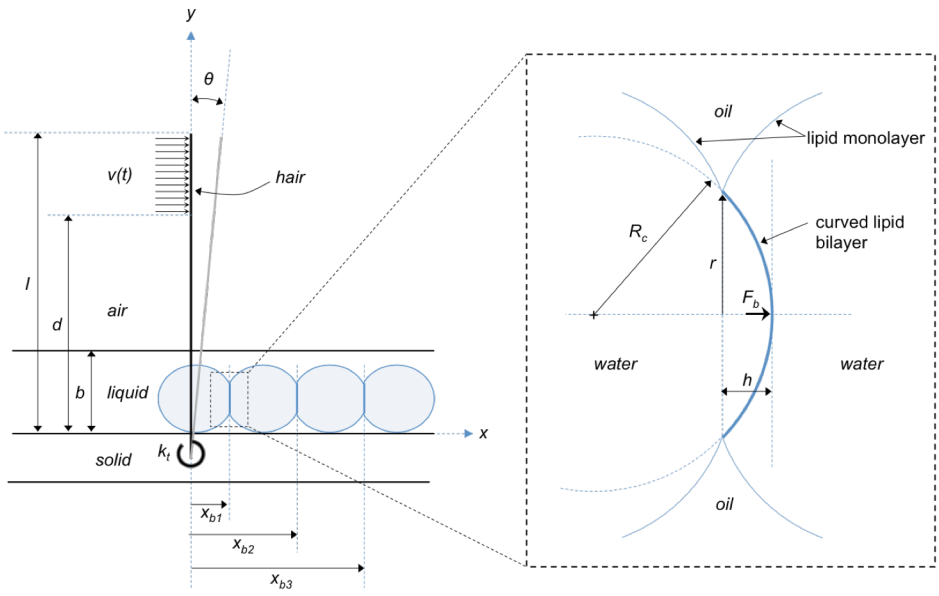

Figure 38: (a) Side view of a membrane-based hair cell sensor shows that the hair extends through two fluid media. (b) Side view of the geometry of a single lipid bilayer bending in response to an applied point force.

use of Stoke's theory is not constrained to rigid body motion. Park, et al[37] more recently applied Stoke's concepts of airflow induced drag and inertia to a cantilevered hair structure that underwent flow-induced bending in a single fluid medium. Motion was simulated by solving for the forced response of a distributed parameter model of a continuous hair with augmented (but constant across the length of the hair) damping and mass per unit length coefficients. Basic assumption and their justifications are shown in Table 3.

Our system is more complex in that the hair in a DIB-based sensor extends through multiple liquid media. Since the fluid media provide both driving forces that induce motion as well as adding drag and inertia to the beam, multiple layers of fluid creates an inhomogeneous cantilevered beam, whose effective damping and mass per unit length are different in each fluid layer. Therefore, to avoid the need for finite element methods [230] to approximate the bending response of an inhomogeneous hair and to retain an analytical model for describing how airflow creates hair motion, we choose to approximate the hair's motion as pure rigid body rotation (i.e. no bending).

The dynamic hair system considered herein is shown in Figure 38. This schematic shows a rigid, cylindrical hair with density, ρ_{hair}, radius, r_h, and total free length, l, that is supported by a solid substrate at the lower end and which extends in the y-direction through a shallow liquid layer of height, b, that represents the water droplets and oil. Horizontal airflow is applied across the top

portion of the hair from a height $y=d$ to the free end at $y=l$. The hair has a mass moment inertia,

Table 2: Table of symbols and definitions

Symbols	Definition	Symbols	Definition
I_h	Mass Moment Inertia of Hair	$F_{inertia}$	Inertial force per unit length
θ	Rotational angle of hair	$T_{inertia}$	Net inertial torque
K_t	Torsional spring with spring constant	c	Damping Coefficient
v	Sinusoidal velocity of airflow	μ_{fluid}	dynamic (shear) visousity
V_0	Velocity Amplitute	ν_{fluid}	Kinematic Viscousity
ω	Angular Frequency	F_{hair}	Force excerted by hair
t	Time	f	frequency of oscillating airflow
l	Length of the Hair	β	efficiency coefficient of transmitted force
d	The length of the hair without airflow	κ	Gaussian moduli of membrane
b	Height of the liquid in sensor	κ	bending moduli of membrane
R_c	Radius of curvature of membrane	J	total membrane curvature
r	Radius of membrane	K	Gaussian membrane curvature
h	height of the spherical cap at the center of the bilayer	f_B	energy per unit area of bending
F_b	Equivalent point force on bilayer	E_b	total energy due to bending
T_{air}	time changing torque on the hair's motion from air	W_F	the work done to create a spherical cap
T_{liquid}	time changing torque on the hair's motion from liquids	C	Capacitance
s	Stokes' parameter	A	Area
F_{drag}	drag force per unit length	C_m	Capacitance per unit Area (Specific Capacitance)
ρ	Density		
T_{drag}	drag-induced moment		

I_h, with respect to the axis of rotation at the fixed end where a torsional spring with spring constant, k_t, is included to represent the restoring torque provided by the substrate. Note the value of k_t is fitted manually in this model to achieve a similar lateral tip motion of the hair as measured during experiments. In the absence of the fluid layers and applied airflow, the equation of motion in terms of the rotational angle, θ, is

$$I_h\ddot{\theta} + k_t\theta = 0 \quad \textbf{Equation 32}$$

To perturb the hair, we assume a uniform, horizontal airflow extending from the surface of the liquid to the top of the hair with sinusoidal velocity in time given by

Table 3: List of assumption for the model development.

Assumptions	Justification
Hair is rigid body	Small angle motion. It might not be the most accurate approach but it allow us to consider this system as single degree of freedom lumped parameter model to approximate the distributed parameters in the system.
Uniform, horizontal airflow extending from the surface of the liquid to the top portion of the hair with sinusoidal velocity in time.	Observation of oscillatory movement of the hair allowed us to consider the airflow as a sinusoidal input. Basically, we assume that an oscillatory airflow, which can be thought of as a time changing torque on the hair
The liquid layer near the supported lower end is assumed to be still	This assumption allow the approximation of drag and inertia forces that are added to the hair.
Membrane is assumed to be pinned along its circumference	So the application of a centered, transverse force (pressure) results in a rotationally symmetric deflection of constant curvature of spherical cap. Therefor the circumference of the circle can be considered as fixed.
The membrane is assumed to be intrinsically flat, which is the case for DIBs formed between identical droplets.	Helfrich method is used to calculate free energy per unit area stored as the membrane bends.
Force which induces transverse deflection at the varies linearly with distance at small deflections, the work done to create a spherical cap of height, h.	This allows us to correlate the membrane deflection of the membrane to the applied point force on the membrane
As the membrane is deformed, neither its thickness or permittivity change, then C_m is constant.	This indicates that the total change in bilayer capacitance must instead result from the change in area incurred by bending

$$v(t) = v_0 \sin(\omega t), \qquad \textbf{Equation 33}$$

where v_0 is the amplitude and $\omega = 2\pi f$ is the angular frequency. While our own experiments have utilized steady airflow to perturb the hair, we observe the hair to undergo oscillatory motion as it bounces in and out of the air stream. Further, the transduction mechanism for current generation depends on a time rate change in capacitance, as opposed to a static change that could be caused by static bending of the hair. Thus, we assume that an oscillatory airflow, which can be thought of as a time changing torque on the hair's motion, $T_{air}(t)$, provides a good approximation of the driving force for hair motion. We have the list of assumptions in

The liquid layer near the supported lower end is assumed to be still. Nonetheless, modeling this layer of fluid using the same approach as that for the air medium [226] is necessary to approximate the drag and momentum that it adds to the hair. Similarly, the net effect of this layer is also that of a time dependent torque, $T_{liq}(t)$, such that

$$I_h\ddot{\theta} + k_t\theta = T_{air}(t) + T_{liq}(t). \qquad \textbf{Equation 34}$$

Then we derivate the drag- and inertia-induced torques from fluids on the hair. In both air and liquid, the net torque acting on the hair is separated into out-of-phase components contributed by drag forces and inertial forces on the hair that depend on the dimensionless Stokes' parameter[226],

$$s = \frac{1}{2} r_h \sqrt{\frac{\omega}{\nu}}, \qquad \textbf{Equation 35}$$

where, $\omega=2\pi f$, ν is the kinematic viscosity of air, and r_h is the cross-sectional hair radius. For a kinematic viscosity of $1.5\text{x}10^{-5}$ m^2/s in air, a hair with radius 40 μm subjected to an oscillating airflow at a frequency, f, of 180 Hz yields a value for s_{air} of 0.174. In contrast, a liquid layer, approximated using a kinetic viscosity of $1.5\text{x}10^{-6}$ m^2/s for water, yields a value of 0.549 for s_{liq}.

Using Stokes' theory, the drag force per unit length induced by fluid flow on a cylinder is given by

$$F_{drag}(y) = \left(\rho_{fluid} \pi r_h^2\right) \omega k' \left(v - y\dot{\theta}\right), \qquad \textbf{Equation 36}$$

where ρ_{fluid} is the density of the corresponding fluid layer and k' is a function that depends on the numerical value of s. The total drag-induced moment, then, across the portion of the hair's length exposed to the fluid is determined through the following integration

$$T_{drag} = \int_{y_1}^{y_2} F_{drag}(y)\, y\, dy. \qquad \textbf{Equation 37}$$

Separately, the inertial force per unit length incurred on the hair by the fluid is given by

$$F_{inertia}(y) = \left(\rho_{fluid} \pi r_h^2\right) k \left(\dot{v} - y\ddot{\theta}\right), \qquad \textbf{Equation 38}$$

where *k* is a different function that again depends on the value of *s*. Again, integrating the product of the inertial force and height along the length of the hair is used to determine the net torque.

$$T_{inertia} = \int_{y_1}^{y_2} F_{inertia}(y)\, y\, dy\,, \qquad \textbf{Equation 39}$$

Equations S3 and S5 show how the net moments in a given fluid phase are computed. Because of differences in fluid properties, velocity, and the value of the Stokes parameter for the region of the hair in air versus liquid, we now separate these calculations for the two media.

In air ($b \le y \le l$), where $s<0.3$, Stokes showed that

$$k' = \frac{G}{s^2} \qquad \textbf{Equation 40}$$

and

$$k = 1 - \frac{\pi G}{4 g s^2}\,, \qquad \textbf{Equation 41}$$

where for both

$$G = \frac{-g}{g^2 + \left(\pi/4\right)^2} \qquad \textbf{Equation 42}$$

and

$$g = \ln(s) + 0.61 \,. \qquad \textbf{Equation 43}$$

Using these definitions, the total drag moment induced by the still ($b \le y < d$) and flowing ($d \le y < l$) layers can be computed by

$$T_{drag}(t)\big|_{air} = \int_b^d A_1\left(-y\dot{\theta}\right) y\, dy + \int_d^l A_1\left(v - y\dot{\theta}\right) y\, dy \,, \qquad \textbf{Equation 44}$$

where, the drag coefficient is given by

$$A_1 = 4\pi\rho_{air}\nu_{air}G \,. \qquad \textbf{Equation 45}$$

Integrating Equation 44 yields

$$T_{drag}(t)\big|_{air} = A_1\left(\frac{l^2 - d^2}{2}\right)v(t) - A_1\left(\frac{l^3 - b^3}{3}\right)\dot{\theta}(t), \qquad \textbf{Equation 46}$$

which demonstrates the airflow acts as both a forcing function dependent on airspeed from $d \le y < l$ (1st term) as well an added source of viscous damping dependent on the speed of rotation (2nd term) across $b \le y < l$. Similarly, the total inertial moment induced by airflow is found by

$$T_{inertia}(t)\big|_{air} = \int_b^d A_2\left(-y\ddot{\theta}\right) y\, dy + \int_d^l A_2\left(\dot{v} - y\ddot{\theta}\right) y\, dy \,, \qquad \textbf{Equation 47}$$

where, the added coefficient of inertia per unit length is given by

$$A_2 = \pi\rho_{air} r_h^2 - \frac{\pi\rho_{air} v_{air} G}{2gf}\,. \qquad \textbf{Equation 48}$$

Again, integration yields an expression of the total inertial moment induced by airflow given by

$$T_{inertia}(t)\big|_{air} = A_2\left(\frac{l^2 - d^2}{2}\right)\dot{v}(t) - A_2\left(\frac{l^3 - b^3}{3}\right)\ddot{\theta}(t)\,, \qquad \textbf{Equation 49}$$

which again shows that the inertial moment induced by airflow acts as both a speed-dependent forcing term (1st term) and an as an added inertia to the system (2nd term).

Under liquid ($0 \le y \le b$), where s>0.3, the same approach is taken but different functions are used:

$$k' = \sqrt{2}s^{-1} + (1/2)s^{-2} \qquad \textbf{Equation 50}$$

and

$$k = 1 + \sqrt{2}s^{-1}\,. \qquad \textbf{Equation 51}$$

Because the liquid is not flowing (i.e $|v|$=0), integration of the drag force per unit length from 0 to b yields the following expression for the drag induced moment

$$T_{drag}(t)\big|_{liq} = A_3\left(\frac{b^3}{3}\right)\dot{\theta}(t)\,, \qquad \textbf{Equation 52}$$

where, using **Equation 50** for *k'*,

$$A_3 = \left(\pi p_{liq} r_h^2\right)\left(2\pi f\right)k' , \qquad \textbf{Equation 53}$$

and an inertia based moment written as

$$T_{inertia}\left(t\right)\Big|_{liq} = A_4\left(\frac{b^3}{3}\right)\ddot{\theta}\left(t\right), \qquad \textbf{Equation 54}$$

where, using **Equation 51** for *k*,

$$A_4 = \left(\pi p_{liq} r_h^2\right)k . \qquad \textbf{Equation 55}$$

Combining Equations Equation 46 and Equation 49 and Equation 52 and Equation 54, respectively, yields expressions for the net torques created by the two fluid media:

$$T_{air}\left(t\right) = \underbrace{\left(\frac{l^2 - d^2}{2}\right)\left[A_1 v\left(t\right) + A_2 \dot{v}\left(t\right)\right]}_{\text{forcing terms}} - \underbrace{\left(\frac{l^3 - b^3}{3}\right)\left[A_1 \dot{\theta}\left(t\right) + A_2 \ddot{\theta}\left(t\right)\right]}_{\text{added damping and inertia}}, \qquad \textbf{Equation 56}$$

and

$$T_{liq}\left(t\right) = \underbrace{\left(\frac{b^3}{3}\right)\left[A_3 \dot{\theta}\left(t\right) + A_4 \ddot{\theta}\left(t\right)\right]}_{\text{added damping and inertia}}. \qquad \textbf{Equation 57}$$

To find explicit expressions for $T_{air}(t)$ and $T_{liq}(t)$ in terms of θ and v, we consider that both fluid layers exhibit moments on the hair that depend on the horizontal relative velocity, $v - y\dot{\theta}$, and acceleration, $\dot{v} - y\ddot{\theta}$, of the fluid with respect to the hair. Using Stokes' theory to model the drag-induced and moment-induced forces per unit length caused by these fluid layers on the hair and integrating them over the portion of the hair's length in each fluid, we obtain expressions (Equation 46 and Equation 47) for the total torque generated by airflow in terms of the airspeed and its derivative and the derivatives of the rotational coordinate, θ. This result indicates that the air layer (including the still portion from $0 \le y < d$ and the flow field from $d \le y \le l$) acts as both a forcing function dependent on airspeed (1st group in Equation 56) as well an added source of viscous damping and inertia dependent on hair rotation (2nd group in Equation 56). A similar approach is pursued to obtain expressions (Equation 52 and Equation 54) for the drag and inertia-based torques on the hair from the still liquid layer. However, because the liquid layer has zero velocity, the total moment induced by this fluid (Equation 57) is only a function of the coordinate of rotation, θ, implying that the liquid layer does not drive motion, but only adds viscous damping and inertia to the equation of motion for the hair.

Combining the drag and inertia-induced moments in air and under liquid allows the complete equation of motion for the hair to be rewritten as

$$\left(I_h + I_{air} + I_{liq}\right)\ddot{\theta}(t) + \left(c_{air} + c_{liq}\right)\dot{\theta}(t) + k_t\theta(t) = \left(\frac{l^2 - d^2}{2}\right)\left(A_1 v(t) + A_2 \dot{v}(t)\right) \quad \textbf{Equation 58}$$

where

$$I_{air} = A_2\left(\frac{l^3 - b^3}{3}\right)$$
$$I_{liq} = A_4\left(\frac{b^3}{3}\right)$$
$$c_{air} = A_1\left(\frac{l^3 - b^3}{3}\right)$$
$$c_{liq} = A_3\left(\frac{b^3}{3}\right)$$

Equation 59

Expressions for the terms A1-A4 are described in the SI. Solving Equation 58 can be used to compute the resulting motion of the hair in response to varying airflow speeds and liquid layer heights. Inspection of Equation 58 confirms that when the liquid layer is removed (i.e. b = 0, and the full length of the hair resides in air), the added inertia and damping only come from the airflow. Second, the equation of motion also confirms that when the hair is fully submerged in still liquid (b = l), the forcing term on the right hand side is zero, which means the hair remains unperturbed by airflow above the liquid layer. The steady-state amplitude of hair rotation is given by

$$|\theta| = \left[\frac{\sqrt{(M_1)^2 + (M_2\omega)^2}}{\sqrt{(k_t - \omega^2 I_t)^2 + (c_t\omega)^2}}\right] v_0$$

Equation 60

where

$$M_1 = A_1 \frac{l^2 - d^2}{2}$$
$$M_2 = A_2 \frac{l^2 - d^2}{2} \quad .$$
$$I_t = I_h + I_{air} + I_{liq}$$
$$c_t = c_{air} + c_{liq}$$

Equation 61

Finally, the undamped natural frequency, f_0, of the coupled fluid-structure system is given by the square root of k_t/I_t.

6.3 Transmitted Force on Bilayer Generated by Hair Motion

The first part of the model yielded a relationship (Equation 60) between the speed of an applied sinusoidal airflow and the resulting rotational vibration of the hair. Now, we focus on the link between hair vibration and the force transmitted to a nearby lipid bilayer. Just as the liquid layer induces a net moment on the hair because of its motion, the hair contributes a resulting moment (and force) of the same magnitude on the fluid. While this moment is distributed from 0 to b, an effective point force under steady-state hair motion exerted at y_b, the height at which the center of the bilayer is positioned, can be written as

$$F_{hair} = \frac{|T_{liq}|}{y_b} \quad .$$

Equation 62

where the magnitude of total liquid-induced moment at steady-state is given by

$$\left|T_{liq}\right| = \frac{b^3}{3}\left(\sqrt{\left(A_3\omega\right)^2 + \left(A_4\omega^2\right)^2}\right)\left|\theta\right|, \qquad \textbf{Equation 63}$$

where the root mean squared is used since the drag-induced torque (which depends on rotational velocity) and inertia-induced torque (which depends on the rotational acceleration) do not occur in phase. Equation 62 estimates the total result force the hair exerts on the liquid layer. Stokes previously demonstrated that a solid plane moving through a fluid creates a propagating normal pressure front that decays as it moves away from the solid-liquid interface [226]. Specifically, at a distance *x* away from the plate, Stokes predicted that the normal pressure, *P*(*x*), to be given by

$$P\left(x\right) = 4\mu_{fluid} v_0 \sqrt{\frac{2\pi f}{\nu_{fluid}}} e^{-\sqrt{\frac{2\pi f}{\nu_{fluid}}}x} \qquad \textbf{Equation 64}$$

.

where μ_{fluid} and ν_{fluid} are the dynamic (shear) and kinematic viscosities of the fluid, respectively, and v_0 and f are the speed and frequency of oscillating airflow. This means that at a distance $x = x_{bi}$ away from the hair, the magnitude of the force acting on the i^{th} membrane is exponentially less than it is at the surface of the hair. Furthermore, since our system considers a small-diameter cylindrical hair rather than an infinite flat plate moving in a fluid, we expect there to be an even lower efficiency in transmitting force through liquid from the hair to the bilayer. Because of both factors, we choose instead to describe the net force

acting on both the adjacent and successive membranes present in a droplet array as empirical fractions of that exerted by the hair on the fluid:

$$F_{bi} = \beta_i F_{hair}\,, \qquad \textbf{Equation 65}$$

where the efficiency of transmitted force, β_i <<1 and $\beta_i > \beta_{i+1}$. Combing Equation 9, 10, and 13 allows the magnitude of the force on the i^{th} bilayer, F_{bi}, to be directly related to the magnitude of hair rotation:

$$F_{bi} = \beta_i \left[\frac{b^3}{3y_b} \left(\sqrt{\left(A_3\omega\right)^2 + \left(A_4\omega^2\right)^2} \right) |\theta| \right]. \qquad \textbf{Equation 66}$$

This approach allows the value of β to be estimated empirically from measurements of bilayer currents induced by airflow at a known flow rate and frequency of vibration.

6.4 Deformation Response of a Lipid Bilayer to an Applied Force

The following derivation considers the deformation of a circular, planar bilayer with a radius, *r*, and a fixed hydrophobic thickness, *t*, where *t*<<*r*. The circular membrane is assumed to be pinned along its circumference such that the application of a centered, transverse force (pressure) results in a rotationally symmetric deflection of constant curvature (Figure 40b). It is well established that it is much easier to bend a lipid bilayer than it is to laterally stretch it [231, 232]. Further, if the membrane is assumed to be intrinsically flat, which is the case for

DIBs formed between identical droplets [233], then Helfrich showed [232, 234, 235] that the free energy per unit area stored in bending is

$$f_B = \frac{1}{2}\kappa J^2 + \bar{\kappa} K \qquad \textbf{Equation 67}$$

where, κ and $\bar{\kappa}$ are the bending and Gaussian moduli of elasticity for the membrane, J is the total membrane curvature and K is the Gaussian curvature. For a circular membrane under radially-symmetric bending in the shape of a spherical cap, J is the sum of equal principle curvatures, each with radius, R_c, and K is the product of the two principle curvatures. Using these definitions, we can rewrite the energy per unit area of bending in terms of the radius of curvature for the membrane

$$f_B = \frac{2\kappa + \bar{\kappa}}{R_c^2} \qquad \textbf{Equation 68}$$

.

The total energy due to bending is then found by multiplying f_B by the area of the deformed membrane, A_b, where $A_b = 2\pi R_c h$ and h is the height of the spherical cap at the center of the bilayer (**Figure 38**). This substitution shows that the total energy of bending, E_B, is determined by the geometrical parameters (R_c and h) and the elastic moduli (κ and $\bar{\kappa}$), as given by

$$E_B = \frac{2\pi h\left(2\kappa + \bar{\kappa}\right)}{R_c} \qquad \textbf{Equation 69}$$

.

Equation 69 represents the total amount of stored energy in a membrane deformed from a flat state into a spherical cap with radius, R_c, and height, h. To relate this to the motion of the hair, we relate the stored energy to the work done on the membrane by an equivalent point force on bilayer, F_b, positioned at the center bilayer. Assuming this force, which induces transverse deflection at the center (**Figure 38**), varies linearly with distance at small deflections, the work done to create a spherical cap of height, h, is

$$W_F = \frac{1}{2} F_b h \quad . \qquad \textbf{Equation 70}$$

Ignoring damping in the membrane's response, we can thus treat the dynamic displacements observed experimentally as discrete, quasi-static solutions, where the work done by the horizontal force, W_F, is equal in magnitude to the energy of bending, E_B, in the bilayer, as written by

$$R_c = \frac{4\pi\left(2\kappa + \bar{\kappa}\right)}{F_b} \quad . \qquad \textbf{Equation 71}$$

This relationship results in an expression that inversely relates the applied force, F_b, to the induced radius of curvature, R_c, of the bent membrane. Note that h cancels, leaving R_c as a solvable term for known values of bending moduli (1.17×10^{-19}J or 28.5 kT for DPhPC membranes) and input force. Equation 71 thus provides a way to compute the amount of deformation created by an applied force in the transverse direction, and it can easily be rewritten in terms of an

equivalent mechanical pressure acting on the bilayer by multiply by the projected area, *A*, of the bilayer.

6.5 Electrical Response to Mechanical Deformation

It has been shown [4, 172] that the magnitude of capacitive sensing current, *i*, generated by the membrane hair cell is given by

$$i = \frac{dC}{dt}\left(V + \alpha V^3\right), \qquad \textbf{Equation 72}$$

, where, *dC/dt* represents the time rate of change in membrane capacitance caused by mechanical deformation of the bilayer, *V* is the transmembrane voltage, and *α* is the electrowetting constant. To arrive at a mechanoelectrical model for the membrane, we must relate *dC/dt* to the state of deformation in the membrane and its intrinsic capacitance per unit area, C_m. Modeled as a parallel plate capacitor, the capacitance per unit area of a bilayer describes the ratio of dielectric permittivity, *ε*, to the thickness, *t*, for the hydrophobic region of the membrane [157], as given by

$$C_m = \frac{C}{A} = \frac{\varepsilon}{t}. \qquad \textbf{Equation 73}$$

Values of C_m for synthetic lipid bilayers range from 0.1-1.0 μF/cm^2, depending on the length and type of the lipid acyl chains and the amount of trapped oil in the membrane [157]. DPhPC bilayers formed in hexadecane as used herein exhibit a membrane capacitance of 0.65 μF/cm^2 [157]. Assuming that when the membrane

is deformed, neither its thickness or permittivity change, then C_m is constant. This means that the total change in bilayer capacitance must instead result from the change in area incurred by bending, as written by

$$\Delta C = C_m \Delta A = C_m \left(2\pi R_c h - \pi r^2 \right) \quad \textbf{Equation 74}$$

,

where r is the radius of the flat, circular membrane. For $h > 0$, $R_c > r$, and $h < R_c$ the height of the spherical cap, h, can be written as:

$$h = R_c - \sqrt{R_c^2 - r^2} \quad \textbf{Equation 75}$$

.

This relationship enables Equations Equation 74 and Equation 71 to be combined to express the change in capacitance, ΔC, as a function of a transverse equivalent force, F_b.

The time required for the membrane to exhibit this change in capacitance depends on the initial deformation state of the membrane. For a perfectly flat membrane, where symmetric deformation to a bent state causes an increase in capacitance for bending in both directions, the capacitive current occurs at twice the frequency of the applied force [236]. Ochs and Petrov referred to this as the microphone effect [236, 237]. However, if the bilayer is initially curved, then an oscillating force increases the capacitance as curvature increases and then decreases capacitance as the membrane returns toward a flatter state. Because these increases and decreases occur in phase with the magnitude of the force, the induced current occurs at the same frequency as the source of mechanical

excitation [236]. Therefore the bilayer can exhibit changes in capacitance at one and two times the frequency of the input.

In our prior study, power spectral analysis of the frequency of measured capacitive currents in single-membrane hair cells demonstrated that energy in the current signal is evenly distributed at both the same frequency as the hair's motion as well as at two times this frequency [172]. This finding suggests that the membrane likely transitions between vibrating from a flat equilibrium condition to one that is distended to one side [236]. Previously, we approximated this multi-mode response with a double sinusoidal capacitance waveform, given by

$$C(t) = C_1 \sin(\omega t) + C_2 \sin(2\omega t), \qquad \textbf{Equation 76}$$

where C_1 and C_2 are the amplitudes of capacitance variation at one and two times the driving frequency, ω, respectively, to derive a relationship between the magnitude of the total change in capacitance, $|C|$, as a function of the measured root mean square (RMS) dC/dt:

$$|C| \approx 1.3 \frac{1}{\sqrt{2}\omega}\left(\frac{dC}{dt}\right)_{RMS}. \qquad \textbf{Equation 77}$$

Here we can instead use Equation 77 to compute the RMS value of dC/dt for a known amplitude of change in capacitance, assumed to be equal to that given by Equation 11 ($|C| = \Delta C$), as shown by

$$\left(\frac{dC}{dt}\right)_{RMS} \approx \frac{\sqrt{2}\omega}{1.3}\Delta C \quad .$$ **Equation 78**

Substituting Equation 74 into Equation 78 and then this result into Equation 72 provides an expression for the RMS value of capacitive current induced by dynamically deforming the membrane within an, ω:

$$(i)_{RMS} = \left[\frac{\sqrt{2}\omega}{1.3} C_m \left(2\pi R_c h - \pi r^2\right)\right]\left(V + \alpha V^3\right) \quad .$$ **Equation 79**

If instead, the membrane were assumed to produce current only at twice the frequency of the input stimulus (i.e. the microphone effect), then the time rate of change in capacitance can be computed from the change in capacitance that occurs in the first ¼ of an oscillation period, *T*, at which the capacitance reaches a maximum. Recalling that in this situation *T* is equal to the reciprocal of twice the frequency, the time rate of change in capacitance can be written as

$$\left(\frac{dC}{dt}\right)_{RMS} \approx \frac{2\sqrt{2}\omega}{\pi}\Delta C \quad .$$ **Equation 80**

Now, combining Equation 72, Equation 74, and Equation 80, we obtain an expression for the magnitude of RMS current produced by a capacitive lipid bilayer that oscillates at twice the driving frequency, ω:

$$(i)_{RMS} = \left[\frac{2\sqrt{2}\omega}{\pi} C_m \left(2\pi R_c h - \pi r^2\right)\right]\left(V + \alpha V^3\right) \quad .$$ **Equation 81**

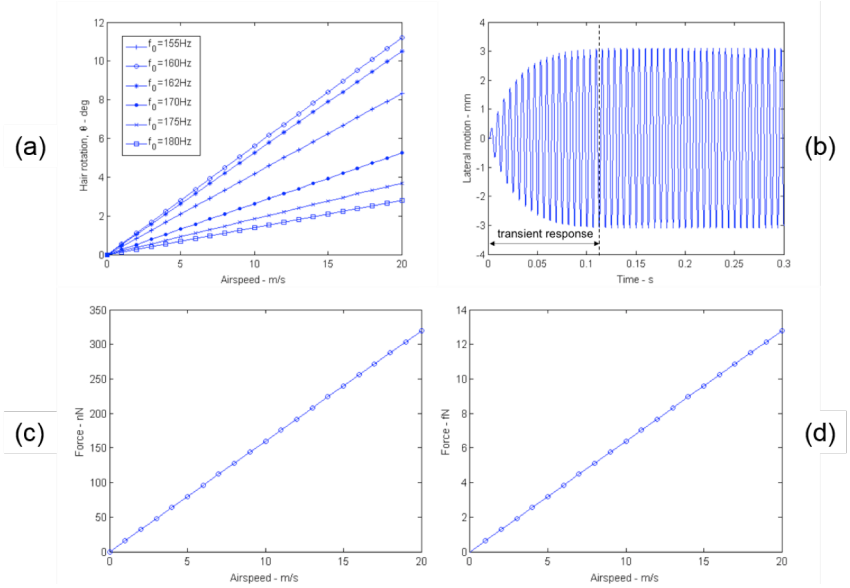

Figure 39: (a) Steady-state hair rotation versus air pseed for different values of undamped natural frequency, f_0. (b) Dynamic lateral motion of the tip of the hair in response to airflow at 20 m/s. (c) Amplitudes of force produced by hair motion on the fluid and (d) the equivalent point force applied to the membrane (b) versus airspeed. A value of $4x10^{-8}$ is used as the force transmission efficiency, β, in (d).

6.5.1 Comparison of Simulated and Measured Hair Cell Responses

a compares the predicted and measured steady-state tip motions of a hair versus airspeed when a horizontal stream of airflow is distributed across the top 15% of the free length of the hair. The model treats the velocity of the applied airflow as a sinusoidal waveform; a driving frequency of 160Hz is selected to mimic the observed oscillatory hair motion near this same frequency when a narrow stream of airflow is applied to the hair. The simulations consider a hair with a radius, free length, and density of 45 μm, 17 mm, and 1100 kg/m^3, respectively. The model also considers that ~24% of the free length of the hair is submerged under liquid (i.e. b = 4 mm), which is modeled as a single homogeneous medium with a

viscosity of 1.5×10^{-5} m^2/s and density of 900 kg/m^3. These values represent the averages of viscosity and density for aqueous droplet and oil present at the base of the hair in the experiments. Finally, the predicted hair motion is calculated for five different values of undamped natural frequency to illustrate the effect of this variable on simulated hair motion.

Figure 40a shows the steady-state lateral tip motion predicted for a rigid hair that undergoes pure rotation in response to the sinusoidal flow. The lateral motion is computed as the product of the free length of the hair and the sine of the steady-state hair's rotation angle, θ, as given in Figure 40b a for a plot of the computed steady-state amplitude of the rotation angle versus airspeed). These calculations show that the maximum amount of hair rotation is ca. 10°, which occurs at the highest velocity of 20 m/s. The measured data points and error bars represent the mean displacement of the hair ± 1 standard deviation, respectively, determined with an anemometer during n=3 separate 10-s trials at each airspeed on a single 17 mm long hair supported as shown in Figure 38. Both the measured and predicted displacements show that tip displacement varies linearly with respect to air velocity. The simulated tip motions in Figure 40a show that a value of ca. 155-165 Hz for f_0 yields predicted tip displacements that fit well to the measured amplitudes of tip motion versus airspeed. Since the airflow is assumed to oscillate at 160 Hz, this match in tip displacements indicates that the hair operates near resonance (likely as a result of the hair bouncing in and out of the narrow flow, or due to vortex-induced vibrations). Since hair vibration at resonance is expected to occur at a frequency that is lower than f_0, we utilize an

assumed value for f_0 of 162 Hz for the remainder of the calculations regarding the membrane's response to this oscillation.

In addition, transient hair motion (shown in Figure 39b by solving Equation 58 in response to a still initial condition for the hair) predicted by the model exhibits a time to reach steady state of approximately 0.12 s, which compares closely to the decay times observed for the flicking responses shown in Chapter 4. These results provide good evidence that the tip motion of a rigid hair in response to a sinusoidal airflow matches suitably to that observed for steady airflow across a flexible hair used in experiments.

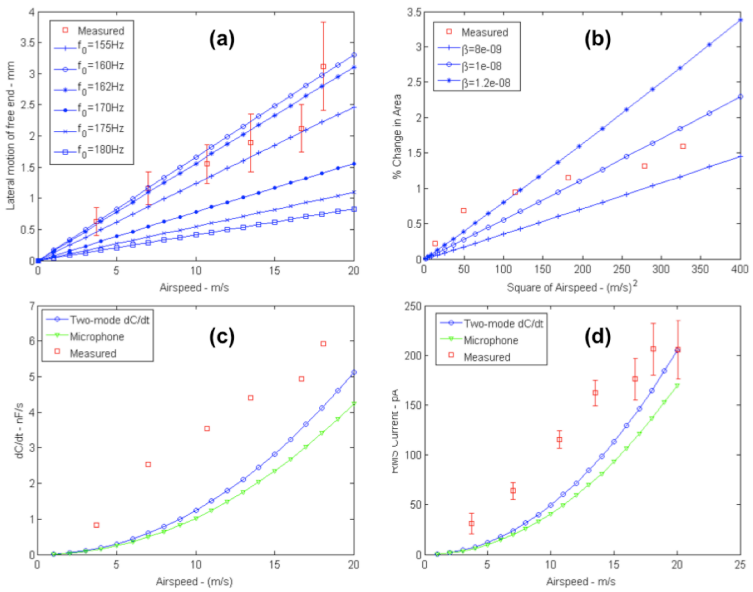

Figure 40: Comparisons between model predictions and data obtained on a two-droplet membrane based hair cell: (a) lateral motion of the tip of the hair versus airspeed; (b) percent change in bilayer area versus airspeed; (c) time rate of change in bilayer capacitance, *dC/dt*, versus airspeed, and (d) RMS current versus airspeed for an applied voltage of 40mV. Predictions for two-mode vibration (Equation 27) and single-frequency microphone effect (Equation 29) are provided in (c) and (d).

These data were also used to predict the equivalent point force induced by the hair on the fluid at a height equal to the center of the droplets (located 0.5 mm up from the pinned end) as given by Equations 11 and 12. Because the motion of the hair varies linearly with airspeed, we find this force also varies linearly versus airspeed with a sensitivity of 63 nN/m/s (see Figure 39c). Therefore, at a speed of 20m/s, the model for a rigid hair oscillating at 160 Hz in both liquid and air predicts that the hair creates a force in the direction of its own motion with a magnitude of ca. 1.26 μN.

Figure 40b compares measured values of percent change in bilayer area versus applied airspeed to those predicted from the radius of curvature of the deformed bilayer (Equation 71) using the expression for change in area shown in Equation 74. Calculating bilayer deformation requires selecting a value for the force transmission efficiency, β, that dictates the effective point force applied to the center of the membrane; here, three values of β are used to demonstrate the relative magnitude and sensitivity of this selection on the predicted force and resulting membrane deformation. This parameterized calculation shows that a β value of ca. $1x10^{-8}$ provides a reasonable match between membrane deformations versus airspeed. Note that a 3% dynamic change in membrane area at 20 m/s is reasonable, and consistent with prior studies which showed membrane rupture occurs under static loading at stretch ratios of 2-5% [71].

Such a small value for β signifies that the amount of force transferred from the motion of the hair to the membrane is on the order of fN (see **Figure 39**d). This is

not surprising since the liquid environment surrounding the hair is expected to result in poor force transmission to the membrane some distance away from the hair. However, the small β may also suggest that the model overestimates the force incurred on the fluid because of an overestimate in the hair motion itself (Equation 62) that would result from a hair undergoing bending in addition to rotation. Pure bending of a cantilevered hair would dictate very small amounts of transverse deflection near the fixed end; thus our estimate of hair motion at a height corresponding to the center of the bilayer may be artificially high. Nonetheless, both the data and predicted values show a similar, approximately linear relationship between the amplitude of bilayer area change versus flow speed.

The remainder of the simulated membrane response versus applied airspeed shows that model captures well the electrical measured changes in a circular membrane that has a radius of 100 μm and a specific capacitance of 0.65 μF/cm^2 (Figure 40 c-d). The measured data and error bars represent the average values ± 1 standard deviation for dC/dt and sensing current measured at each flow speed for n=3 separate single-membrane sensors that featured the same hair (i.e. each trial used the same substrate and hair but with new droplets and a new bilayer). In comparisons of both dC/dt and rms current, the simulated responses show that a two-frequency capacitive current generates a higher response that a single mode response at the same frequency of the hair's motion. The fact that both predictions underestimate the total dC/dt and rms current may indicate current developed by the membrane does not occur just at these two frequencies

but also includes motion across a range of frequencies. It is also possible that the thickness and specific capacitance of the membrane vary slightly during vibration, which would cause our use of values measured in a static configuration to undervalue the change in capacitance at a given voltage.

6.6 Discussion

The transduction model presented demonstrates that the physical properties of the hair and the dynamics of the hair's motion, as well as the area, thickness, dielectric permittivity, and bending modulus of the interfacial membrane (1.17×10^{-19} J or 28.5 kT for DPhPC membranes [238]) dictate the amount of membrane deformation and change in capacitance that produces current. In this work, the model was implemented to predict the sensing current generated by a single membrane adjacent to a hair perturbed by airflow. Figure 40d shows that we achieved a suitable approximation for the tip motion of a hair perturbed by airflow, as well as the change in capacitance and current by the membrane when a transmission efficiency factor, β, was selected to adjust the force applied to the membrane. These predictions can be extended to additional membranes in an array by utilizing empirically derived decay rates such as those found from the data of successive bilayer currents shown in Chapter 4. The primary limitations of our model include the facts that: 1) a rigid body model for hair motion likely overestimates the displacement of the hair at a height near the bilayer; and 2) we cannot exactly predict or measure both the force applied to the membrane and the dynamic shape of the bilayer as it vibrates.

Nonetheless, our findings demonstrate for the first the value of using an array of multiple lipid bilayers formed with more than two droplets to increase the magnitude of total sensing response and to enable distributed membrane-based sensing of hair motion for more than one hair in an array. This advance showcases the evolution of this system from a single hair, single membrane sensor to a higher-order functional assembly comprised of many droplets arranged 2D. Further, when combined with methods to encapsulate liquid-supported DIBs in a sealed-solid material using either a microfluidic approach [239] or via direct encapsulation of DIBs in a solid-organic phase (*manuscript in preparation*), we believe multi-membrane DIBs can enable the development of bio-inspired material systems that can perform mechanotransduction—i.e. feel their surroundings by sensing physical stimuli that cause the encased membranes to deform—in ways similar to how animals sense mechanical disturbances. To enable hair cell functionality in a fully-sealed assembly, we would need to add a hair structure that passes from the enclosed droplets through the sealing layer such that it could interact with a surrounding medium, such as water, which would normally displace (due to density differences or hydrodynamic flows) the oil and water droplets or contaminate the system in a way that prevents reliable lipid self-assembly at the surface of the droplets.

In summary, we view potential applications of DIB-based hair cells as being similar to those performed by the hair cells of living creatures, e.g. vibration sensing, flow detection, tactile sensing, and acoustic response. The reliability of this device demands that the membrane not only be durable, but that the

interaction between the hair and the membrane(s) be relatively consistent during operation. The use of block copolymer molecules for enhancing membrane stability [117] is one specific method in which the reliability of the membranes could be improved. However, unlike solid-state hair cell inspired sensors built from silicon or polymers, a soft biomolecular approach at sensing offers advantages such as lower cost and the potential for rapid re-assembly to refresh the system. Additionally, we emphasize that the use of biomembranes for enabling sensing provides a versatile environment for adding additional functionality to the system through the incorporation of transmembrane or membrane-active biomolecules. One example is the use of mechanosensitive transmembrane molecules, which would enable sensing currents in response to membrane stretch [187, 188]. Like in animals, where many hair cells are used to provide multi-modal forms of mechanotransduction, we thus believe the DIB can enable new forms of membrane-based sensing arrays that exhibit spatially, directional, and frequency selectivity to a variety of physical inputs including vibration, fluid flow, and also acoustic pressure.

6.7 CSI's in Hair Cell Sensor and Model

The hair cell sensor assembled in similar manner described in Chapter 3 using CSIs as the transducer between two droplets. While this model works for the DIB's, we examine this same mechanoelectrical model for our CSI hair cell sensors. We have performed hair cell experiments at two different airflow speeds (10.7 and 16.7 m/s)for CSIs under 1:1 AR20-Hex. A series of experiments were

performed at these two airflow speeds. Airflow was applied to the hair cell in a direction perpendicular to the bilayer in all cases. At each flow speed, the current produced by the bilayer was measured for 10s at applied transmembrane voltages from 100 to 400mV in 100mV steps (Figure 41a). Figure 41b shows the raw current response to continuous airflow at 10.7 m/s applied, and the increases in current correspond to stepwise increases in the applied dc voltage.

Figure 41c shows RMS values of the measured current versus applied voltage for 2 different flow speeds of 10.7 amd 16.7m/s. Each data point in this figure represents the average of the RMS current measured for three different bilayers formed in the same substrate and tested with the same hair at each voltage and

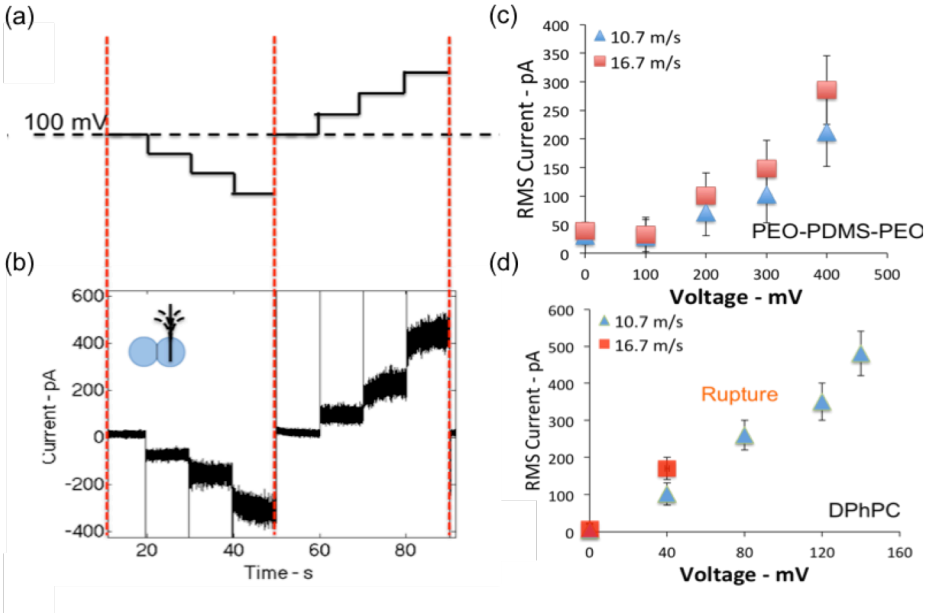

Figure 41: (a) applied transmembrane voltages from 100 to 400mV in 100mV steps, (b) the raw current response to continuous airflow at 10.7 m/s applied, RMS values of the measured current versus applied voltage for 2 different flow speeds of 10.7 amd 16.7m/s (c) for CSI and (d) for DPhPC DIB's.

speed. The measured current at zero volts during the airflow has been subtracted from each of the averaged current values to remove background current ($i_{V=0}$) not associated with membrane vibration. Consequently, the data show linear relationships between RMS current versus voltage for the various airflow speeds, where the slope of each current-voltage series represents the time rate of change of membrane capacitance, *dC/dt*, at each airflow speed. As well as the data presented in DIBs in chapter 3, the data show that lower airflow speeds produce less current per unit voltage, while faster airflow induces higher current output due to greater deflection of the hair. Figure 41d shows the data of DIB for the same airspeeds for the comparison reasons. These results confirm that the thicker CSI membranes withstand under larger airflow strength and larger applied voltage. The time rate change of the capacitance *(dC/dt)* for CSI membranes in these two speeds are computed as described in chapter 3. Moreover we can see that the CSI membranes produces a lower time rate change of capacitance in membrane under same airflow. This can be due to its larger thickness and lower tension.

Now that we have experimentally tested CSI, we are motivated to test the results of CSI hair cells with our developed hair cell model. Utilizing the specific capacitance of CSI in 1:1 AR20-Hex measured in Chapter 5 and the estimated value for its bending modulus, we estimated the *dC/dt* using our mechanotransduction model. The bending stiffness is 1.17×10^{-19}J for DPhPC membraneThe bending stiffness for the CSIs is estimated using [240, 241]:

$$K_b \propto d^2\gamma \qquad \text{Equation 82}$$

where d is the thickness of the membrane and γ is the membrane bilayer tension. With this proportional relationship and extimated values shown in chapter 5 we have estimated the bending stiffness for the CSI formed under 1:1 AR20-Hex to be $1.48\text{x}10^{-19}$J. Using this bensing stiffness modulus and specific capacitance of this type of membrane estimated in chapter 5, we can simulate the *dC/dt* for the CSI membrane hair cell formed under 1:1 AR20-Hex. Figure 42a comparing this simulated results with experimental data for both CSI and DIB. We can see that the experimentally measured dC/dt is matching both CSI and DIB simulated results. It can be seen the thicker CSI produces smaller time rate change of capacitance in membrane at similar applied airflow.

Moreover, in different approach, we used the simulated data and measured *dC/dt* to compute the mechanical properties of membranes. In this approach we run the

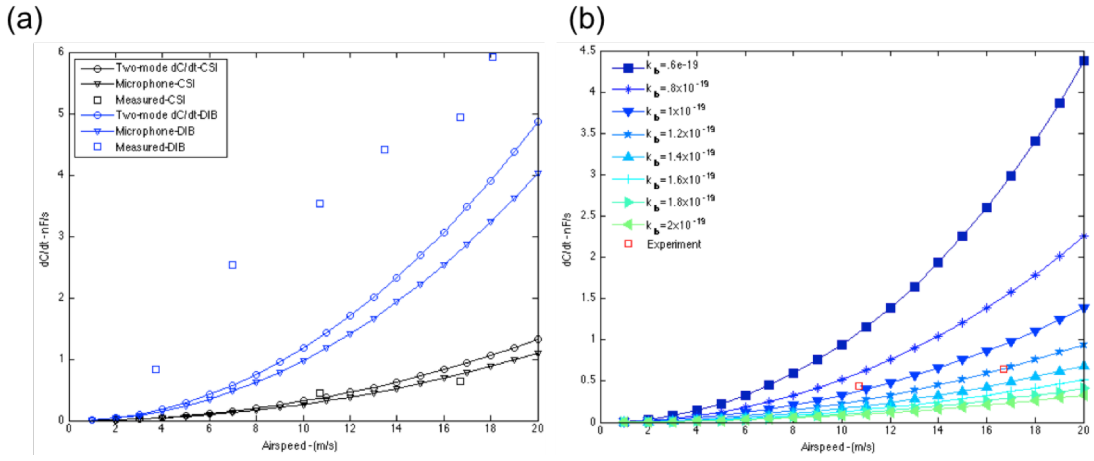

Figure 42: Time rate of change in lipid bilayer (a) and copolymer interface (b) capacitance, *dC/dt*, versus airspeed.

simulated results for different membrane bending modulus and we matched the simulated results to the experimental data (Figure 42b). As it can be seen in this figure the K_b is changed from $0.6x10^{-19}$ J to $2x10^{-19}$ J. We can see that the data matches the simulated results between 1.4-1.6 $x10^{-19}$ J. This results shows that not only the hair cell sensors have great potential for sensing flow but also can be used to predict the membrane physical properties. Moreover, we calculated the maximum percent change in area of $8*10^{-5}$ % and $1.15*10^{-4}$ % in two speed of 10.7 and 16.7 m/s, respectively. We can see the percent change of area in CSI cases are significantly lower to compare to DIB cases in same speed. This can be a result of thicker and stiffer CSI's and also can explain the larger range of operation.

Note that the β value is kept constant in both cases since this parameter is only depend mechanical boundaries which were same for both cases (assuming same fluid densities, droplet sizes and hair).

6.8 Conclusions

This chapter for the first time presented a mechanotransduction model for a membrane-based hair cell. This model combined Stoke's theory for the effects of fluids on the motion of the hair, Helfrich's expression for membrane bending, and our own model for voltage-dependent capacitive current produced by a vibrating membrane. Using a sinusoidal airflow as the input, our model predicted similar motions of the tip of the hair, and, with a single fitting parameter used to tune the amount of force transmitted to the bilayer from the hair, we also obtained close

matches in the magnitudes of the time rate of change in membrane capacitance and the sensing current. As described, this model can be extended to describe bilayer currents in a multi-membrane array by utilizing empirically derived rates of current decay in successive membranes. The order-of-magnitude approximations provided by this model will help us to improve hair cell inspired, membrane-based sensors through the selection and tuning of the material properties for both the aqueous volumes and the membranes themselves, as well as understand how hair properties and placement can be selected for specific sensing applications.

CHAPTER 7: CONCLUSIONS AND CONTRIBUTIONS

7.1 Overview and Summary

Our general approach in this work was to develop experimental and theoretical techniques for characterizing membrane based hair cell sensors that feature one or more membranes formed from either phospholipids or amphiphilic polymers. Multiple characterization techniques were performed for the purpose of better understanding how intra-droplet membrane systems can be used as mechanotransduction sensors. The research performed addressed specific scientific gaps and the outcome of these research activities enhanced understanding of these systems. The key findings in our work and the novel contribution of this dissertation are provided below.

7.1.1 **Research Objective 1:**

Develop a more robust hair cell embodiment, and thoroughly characterize membrane-based mechanotransduction, including sensitivity, directionality, and the frequency response of the membrane, in response to airflow and hair flicking.

The durable and robust hair cell sensor was developed by rooting a cantilevered hair into the substrate and allowing large, and repeated deformations of the hair without rupturing the membranes. Due to greater robustness, we were able to more fully characterize the mechanoelectrical transduction process of a membrane-based hair cell sensor both with discrete and continuous

perturbations. This presentation shows clearly that the time rate of change in bilayer capacitance is proportional to the strength of the applied stimulus (i.e. not the transmembrane voltage) and that *dC/dt* increases linearly with respect to the level of hair perturbation as given by airflow. Sensing currents at both resonance and lower frequency excitations show that the membrane vibrates at the same frequency of the hair. The sensitivity value for perpendicular (90°) airflow is highest at 4.05nF/s, whereas measured sensitivity is only 0.81nF/s and 0.27nF/s for 45° and parallel (0°) airflow, respectively. This result shows that the direction of the hair's motion directly influences the membrane's response to a particular perturbation. Moreover we showed that as the hair is being shaken with frequency lower than natural frequency of the hair, in a direction perpendicular to the membrane, it produces a time rate change of capacitance in the membrane at the same frequency of the input excitation. Also, our results indicate that as the hair is shaken with shaker, higher frequency simply cause higher rate of change in the applied hair displacement and therefore higher sensing response due to smaller *dt*. Moreover our results show that stiffer hydrogel-sandwiched membranes produce a larger response compared to bilayers formed between two liquid aqueous volumes. Furthermore, measurements of sensitivity (5-35 pA/m/s) and minimum (4.0-0.6m/s) and maximum (28-13m/s) sensing thresholds to airflow are performed for the first time, and we observe maximum electrical power (VxI) (~65pW) in the membrane occurs for combinations of slower airflow and higher voltage.

7.1.2 **Research Objective 2:**

Assemble and experimentally characterize the mechanotransduction responses of each membrane in a multi-membrane droplet array. The specific goals are to: a) understand how multiple membranes respond to the motion of one or more hairs in the array, b) assess the propagation of vibration in a droplet array by determining how many membranes away from a moving hair yield a sensing current, c) characterize the relative timing of sensing responses of each membrane relative to hair motion, and d) explore how multiple membranes respond to perturbations of multiple hairs in the array.

Mechanoelectrical transductions of hair motion using multi-membrane DIB arrays with more than 2 droplets and multiple hairs were characterized. Linear chains of up to 5 connected droplets demonstrate that perturbation of a single hair creates vibrations that propagate across several droplets, allowing for membranes that are not directly attached to the hair to still transduce its motion. Our results showed that membranes positioned closest to the hair generate the largest currents, while those farther away produce less current due to energy loss from fluid damping.

Moreover we have studies the effect of placement of the hair in membrane based hair cell array. Our result indicated that bilayers positioned on the same side of the excited droplet (i.e. the droplet contained hair) or symmetrically on both sides of the excited droplet transduce vibrational energy from the hair with the

amplitude being a function of distance from the hair. These transient responses of these droplet arrays is that the sensing currents for the asymmetric 3-bilayer array (i.e. all membrane in one side of the hair) appear to occur in synchronization, while the measured currents for the two bilayers positioned symmetrically on opposite sides of the hair are out-of-phase with each other. currents produced by all three bilayers in the asymmetric array are positively correlated with a time lag of 0.18 ms. In other trials (not shown), multiple membranes aligned on the same side of the hair again exhibited positive correlations, indicating that currents are nearly “in-phase”. The small time lag per successive droplet interface averages between 0.18 and 0.20 ms, which for vibration of the hair 158 Hz, corresponds to a phase angle of ca. 8.1°. Separately, cross-correlation analysis of the two bilayers for the symmetric 3-droplet, 2-bilayer array showed a negative maximum correlation coefficient at a time lag of 0.13 ms, confirming quantitatively that the currents are 180° ± 6.1° “out of phase.

Different lengths for the two hairs are intentionally selected to separate their characteristic frequencies of vibration. We used two hairs of different lengths to examine the frequency selectivity of a multi-bilayer DIB array. Power spectral densities (PSDs) of sensing currents reveal a predominant peak frequency at 293 Hz when the shorter hair is flicked and a separate peak at 158 Hz in when the longer hair is flicked for all the membranes in the array. Based on comparison of the responses with respect the length of the hair we showed that the

membranes in our hair cell sensor respond as cantilevered beams (i.e. the hair) in the system.

7.1.3 **Research Objective 3:**

Examine the role of polymer structure and oil selection on the assembly and physical properties of polymer-based membranes formed between droplets, and compare the mechanotransduction responses of polymer-based DIBs to those formed using lipids.

We characterized electrical and mechanical properties of CSI membrane such as voltage and electric fields required for formation and rupture, electrowetting, specific capacitance, membrane resistance, thickness and monolayer and intradroplet interface tensions.

We formed stabilized interfaces of poly(ethylene oxide)-b-poly(dimethyl siloxane)-b-poly(ethylene oxide) triblock copolymer stabilized interfaces (CSIs) between polymer-coated aqueous droplets in alkanes and silicone oil. We proved that, unlike lipid-coated droplets, triblock-coated droplets do not spontaneously adhere in oil when the organic phase is a *good* solvent for the hydrophobic PDMS block. A thinned planar membrane only forms at the interface between adjacent droplets upon application of sufficiently large transmembrane voltage, which removes excess solvent through electrocompression (Patent Filed: PD 15110).

We compared the voltage required to form and rupture these membranes. We observed that CSIs assembled in oil mixtures containing AR20 silicone oil display higher formation and rupture potentials than those obtained in alkanes.

We characterized the electrowetting behavior of CSI's. Our result indicated that at applied voltages above the threshold required to initiate membrane thinning, electrowetting causes the area of the CSI between droplets to increase while thickness remains constant. The membrane formed using CSI under good solvent exhibit relatively higher electrowetting constant. Moreover, we showed that CSI electrowetting increases with the fraction of silicone oil (good solvent) in the nonpolar solvent surrounding droplets.

Moreover we characterized the specific capacitance and thickness of CSIs under different combination of oils. CSIs formed in oils containing silicone oil exhibit lower values of C_m than those formed in alkanes. Therefore, CSIs in alkanes are thinner than those in silicone oil mixtures, which suggests that CSIs formed in alkanes contain less residual solvent upon voltage-initiated adhesion.

We also characterized the membrane resistance and compared them to the DIBs. While CSIs are exhibiting far lower values of nominal resistance (0.2-2 GΩ) than lipid bilayers (10-100GΩ), values of CSI membrane resistance on the order of 20-30MΩcm^2 are quite similar in magnitude to those for lipid bilayers (10-100MΩcm^2). Despite the higher rupture potentials for CSIs, the electric field sustained by a much thinner lipid membrane is approximately 2-3X higher than that which is required to cause rupture in the triblock-stabilized interfaces.

Finally, we measured and computed the monolayer and bilayer tension to better understand the energetics of the CSIs. While the monolayer tensions for CSIs in alkanes are similar in magnitude to that for a DPhPC monolayer (~1-1.3mN/m [221]), these data show that copolymer monolayers at a water-silicone oil mixture interface are considerably lower (~0.1mN/m). CSIs formed in alkanes exhibit membrane tensions (~2.0-2.5 mN/m) similar in magnitude to a lipid DIB, due to both similar values of monolayer tension and contact angle (20-30º).

7.1.4 **Research Objective 4:**

Develop a model that captures the entire transduction process to understand the key physical parameters or design variables for the sensing response. This model combines Helfrich theory of membrane deformation and Stokes theory of pendulums moving in fluids to understand how parameters like hair length, membrane stiffness, and membrane capacitance affect the sensing current in response to airflow.

Our model combines Stoke's theory for the effects of fluids on the motion of the hair due to vortex-induced vibration, Helfrich's expression for membrane bending, and our own model for voltage-dependent capacitive current produced by a vibrating membrane. We described the net force acting on both the adjacent and successive membranes present in a droplet array as empirical fractions of that exerted by the hair with a efficiency factor of b. The value of b is estimated empirically from measurements of bilayer currents induced by airflow at a known flow rate and frequency of vibration.

Final expression of our model estimates current generated as a function of frequency, specific capacitance, bending modulus, force applied to membrane (f_b); where this f_b itself is a function of flow speed and tip displacement. With this model we were able to predict the hair lateral tip motion, and then the percent change of area of the membrane for different b values and match the estimations with the measured data to find the accurate b for our system. After finding the b, the dC/dt is estimated based on known specific capacitance and bending modulus of the membrane and therefore we used membrane current model to estimate the current which matched well with the measured data for both DIB's and CSI's. Our results shows that the current generated by the hair cell sensor can be predicted for given airflow and membrane.

Lastly, we used this model in reverse for CSI's hair cells with thicker which causes them for lower stiffness

7.2 Conclusions

Membrane-based hair cell sensors show capabilities for sensing both discrete and continuous types of perturbations. In this study, we showed that the current response of a revised membrane-based sensor is dependent on several parameters: 1) the voltage across the membrane, 2) the strength, direction, and frequency of the perturbation, and 3) the material compositions of the aqueous volumes used to form the bilayer. The revised embodiment features a hair that is rooted firmly in the polymeric substrate that also supports the lipid bilayer.

Compared to the first generation membrane-based hair cell sensor, the results of these experiments show that the new embodiment is much more durable, allowing large and repeated deformations of the hair. Due to greater robustness, we were able to more fully characterize the mechanoelectrical transduction process of a membrane-based hair cell sensor.

Our results confirm that the bilayer exhibits a time rate of change in capacitance (*dC/dt*) due to transverse bending in response to motion of the hair, where the magnitude of *dC/dt* depends on the strength and direction of the applied stimulus. Similar to the first generation of the hair cell sensor, analysis of the hair's motion relative to measured sensing currents at both resonance and lower frequency excitations show that the membrane vibrates at the same frequency of the hair. However, the higher values of *dC/dt* (0.8-6nS/s) and percent change in membrane area (0.2-2.0%) indicate that cantilevering the hair in the solid substrate results in greater energy transfer to the membrane resulting in bending; this is likely due to both a stiffening effect of the hair and added transmission of energy through the substrate. A more subtle benefit of the revised embodiment is the fact that the lipid aqueous volumes can be either pure liquids or liquid-swollen gels material. Our tests on both types of volumes show that the freedom to vary the material composition can be used to tailor both the mechanical properties and sensitivity.

In context to its use as a sensor, this study yielded new information regarding the sensitivity and dynamic range of a membrane-based hair cell in response to

airflow. These tests revealed that the current output by a sensor varies linearly with respect to the applied airflow for a given voltage level. However, a trade-off exists: while increasing the voltage amplifies the sensitivity of the response to airflow and reduces the minimum airflow speed that can be detected, it also narrows the range of airspeeds that can be detected without rupturing the bilayer. Nonetheless, the results confirm that the applied voltage can be used to tune the performance to a given application. A voltage <60mV may be best suited for sensing airflow across a wide range of speeds, while increasing the applied voltage to ~100mV can provide greater sensitivity and a lower threshold for detecting slower sources of airflow. This finding is especially important when comparing sensor modalities and in configuring a membrane-based sensor for a specific sensing application.

For the first time multi-bilayer DIB networks resemble the membrane-divided compartments native to living cells. In this study, serial arrays of lipid-coated droplets were connected to create a multi-bilayer hair cell sensor featuring one or more hair structures. Similar to a single-bilayer hair cell sensor, each 5 nm-thick membrane in the array functions as a flexible capacitor that generates current in response to vibration. This finding was confirmed by measuring the individual bilayer currents across all interfaces in the array. Bilayers positioned closest to the hair generate the largest capacitive currents, while those positioned farther away generated lower outputs. The reduction in currents across successive interfaces shows that energy is dissipated in the system, likely in the form of viscous damping, both in the droplets and in the surrounding oil reservoir. Our

experiments also showed that a serial DIB array produces a similar total sensing response to that predicted for several single DIB hair cell sensors. Different length hairs in the hair cell sensor produced currents with different characteristic frequencies, which we used to show how the motion of the hair induces current in every membrane of a serial array and how hairs rooted in the PDMS substrate act as cantilevered beams in free vibration. Also, shorter, stiffer hairs produced larger bilayer currents than longer, more compliant hairs. The fact that bilayer currents decay at successive interfaces away from the hair enables stimulus localization in arrays with multiple hairs.

In next part of the work, we replaced the lipid with copolymer to achieve a better stability. To-date planar membranes assembled from triblock copolymer membranes have utilized a combination of *good* and *poor* solvents (typically chloroform—*good* and decane or toluene—*poor*) in proportions that leave the mixture predominantly *poor* for the middle hydrophobic block. This selection has resulted in the spontaneous membrane thinning [117, 118]. In contrast, our study showed that polymer-stabilized adhesion between droplets in a *good* solvent for the middle block is pressure-dependent and completely reversible, which indicates that there is an initial energy barrier to forming an adhesive interface. We quantified this barrier in the form the minimum applied pressure achieved via electrocompression needed to remove excess oil from between opposing monolayers. The results of these measurements showed that the height of the repulsive barrier to adhesion increases with increasing solubility of the hydrophobic block in the oil; thus, more voltage or mechanical pressure is

required to exclude solvent. Characterizations of the thinned interface upon overcoming the barrier to adhesion show that CSIs formed in silicone oil-based solvents yield thicker membranes that also exist at a lower tension state. These findings are supported by well-known brush theories that predict an increase in brush length and a decrease in area per molecule at the interface for polymers in a good solvent. However, the demonstration of tuning this adhesion between small-volume droplets using voltage offers new capability for both connecting and disconnecting polymer-stabilized aqueous volumes, enabling new forms of tunable modularity in droplet-based microfluidics, voltage-sensitive emulsions, and membrane-inspired material systems.

In the chapter 6, we presented for the first time a mechanotransduction model for a membrane-based hair cell. This model combines Stoke's theory for the effects of fluids on the motion of the hair, Helfrich's expression for membrane bending, and our own model for voltage-dependent capacitive current produced by a vibrating membrane. Using a sinusoidal airflow as the input, our model predicted similar motions of the tip of the hair, and, with a single fitting parameter used to tune the amount of force transmitted to the bilayer from the hair, we also obtained close matches in the magnitudes of the time rate of change in membrane capacitance and the sensing current. As described, this model can be extended to describe bilayer currents in a multi-membrane array by utilizing empirically derived rates of current decay in successive membranes. The order-of-magnitude approximations provided by this model will help us to improve hair cell inspired, membrane-based sensors through the selection and tuning of the

material properties for both the aqueous volumes and the membranes themselves, as well as understand how hair properties and placement can be selected for specific sensing applications.

7.3 Contribution

We developed for the first time multi-membrane inter-droplet transducers and showed that the inter-droplet membrane based sensors can be developed for special mechanical sensing applications with large range of sensitivity and operation. In this work, we studied the parameters that affect and tune the formation and sensing characteristics of the inter-droplet membrane-based sensors. Both mechanical and electrical parameters are shown to be effective in sensing characteristics of membrane-based sensors. We showed that these parameters can be tuned by altering the surfactant and solvent for desired sensing. We showed that how the selection of solvent and surfactant affect the mechanical and electrical characteristics of inter-droplet sensors.

In second part of our work, for the first time, we characterized voltage activated polymeric inter-droplet membranes in thermodynamically good solvents. We showed that the solubility of the hydrophobic chain of the membrane in solvent plays a key role in both the mechanical and electrical properties of the copolymer membrane. This contribution demonstrates that in addition to phospholipid membranes, mechanotransduction can be performed using synthetic amphiphilic polymers, which greatly increases the ability to tune the characteristics of the membrane for a desired sensing application.

In last part of our study, we developed a complete mechanotransduction model for describing the relationship between airflow and sensing current for hair cell sensors that use a thin membrane as the sensing element. Describing the complete transduction process required us to understand: 1) how airflow affects hair motion; 2) how hair motion induces forces on nearby bilayers; 3) how this force drives membrane deformation; and 4) how dynamic changes in deformation state create variations in capacitance that generate current. This model provided physical insights into how membrane-based materials can be used for sensing mechanical stimuli—just like nature does.

7.4 Future Work

Membrane based materials have shown a great potential to be used as a new class of smart materials and transducers. While in this work we showed that the fluid capacitive membrane transducers can be developed using biomolecules and polymers, there is still great potential so investigate how these types of sensors can be further tuned by the incorporation of peptides, proteins and other bio-nano materials that add new functionality such as stimuli-regulated transport. Since there are full ranges of materials that can induce conductance on these membranes by creation of pore, there is a great possibility that these materials can increase the functionality and sensitivity of these types of membrane-based sensors. These membrane-based sensors can be also improved by placing them in enclosed encapsulated environment so that they can be durably operated in

variety of environments. Some parallel efforts in our lab are working on development of fully encapsulated inter-droplet membrane systems.

The durability, tune-ability and range of operation of membrane based hair cell sensors are improved when the polymers instead of lipids are used to construct these membrane-based transducers instead of lipids. The voltage-activated and durable polymeric membranes have great potential for other applications and can also be used to study and develop compartmentalized drug delivery systems and particle packaging applications. Different diblock and triblock copolymer can be used to study these membrane-based systems to better understand the effect of solvents and polymer type exchanges on formation, mechanical and electrical properties and functionality of these membranes. It will be very interesting to find the critical mechanical, physical and electrical values for different properties of these membranes where different peptides and proteins are allowed to insert up on application of voltage.

The new class of membrane-based smart materials can be developed using block copolymers and lipid under different types of solvents. The interaction of these types of materials with proteins and peptides can lead to develop multi-modal sensing devices, which uses biomolecules and mechanical stimuli to produce electrical signal. Moreover, these types of materials may be utilized to develop energy harvesting and self-powered sensors using ionic voltage across the membrane (i.e. salt concentration gradient).

REFERENCES

1. *Bio-mimetic Drag Reduction – Part 1: Sensing.* 2012.

2. Sarles, S.A., *Physical encapsulation of interface bilayers*. 2010, Virginia Polytechnic Institute and State University.

3. Sarles, S.A., J.D. Madden, and D.J. Leo, *Hair cell inspired mechanotransduction with a gel-supported, artificial lipid membrane.* Soft matter, 2011. **7**(10): p. 4644-4653.

4. Sarles, S.A., J.D.W. Madden, and D.J. Leo, *Hair cell inspired mechanotransduction with a gel-supported, artificial lipid membrane.* Soft Matter, 2011. **7**(10): p. 4644-4653.

5. Hein, M.A., et al., *Fabrication of bioinspired inorganic nanocilia sensors.* Magnetics, IEEE Transactions on, 2013. **49**(1): p. 191-196.

6. Ochs, A.L. and R.M. Burton, *Electrical response to vibration of a lipid bilayer membrane.* Biophysical journal, 1974. **14**(6): p. 473-489.

7. Crowley, K., et al. *Paper-based MEMS hair cell array*. in *SENSORS, 2013 IEEE*. 2013. IEEE.

8. Park, H., et al. *A Hair-cell Structure based Piezoelectric Energy Harvester Operating under Three Dimensional Arbitrary Vibrations*. in *Journal of Physics: Conference Series*. 2013. IOP Publishing.

9. Selva, P., C.M. Oman, and H.A. Stone, *Mechanical properties and motion of the cupula of the human semicircular canal.* Journal of Vestibular Research, 2009. **19**(3): p. 95-110.

10. Dallos, P. and B.N. Evans, *High-Frequency Motility of Outer Hair Cells and the Cochlear Amplifier.* Science, 1995. **267**(5206): p. 2006-2009.

11. Zheng, J., et al., *Prestin is the motor protein of cochlear outer hair cells.* Nature, 2000. **405**(6783): p. 149-155.

12. Raphael, R.M., A.S. Popel, and W.E. Brownell, *A Membrane Bending Model of Outer Hair Cell Electromotility.* Biophysical Journal, 2000. **78**(6): p. 2844-2862.

13. McHenry, M.J. and S.M. van Netten, *The flexural stiffness of superficial neuromasts in the zebrafish (Danio rerio) lateral line.* Journal of Experimental Biology, 2007. **210**(23): p. 4244-4253.

14. Albert, et al., *Arthropod touch reception: spider hair sensilla as rapid touch detectors.* Journal of Comparative Physiology A: Neuroethology, Sensory, Neural, and Behavioral Physiology, 2001. **187**(4): p. 303-312.

15. Barth, F.G., *How To Catch the Wind: Spider Hairs Specialized for Sensing the Movement of Air.* Naturwissenschaften, 2000. **87**(2): p. 51-58.

16. Spoon, C. and W. Grant, *Biomechanics of hair cell kinocilia: experimental measurement of kinocilium shaft stiffness and base rotational stiffness with Euler-Bernoulli and Timoshenko beam analysis.* J Exp Biol, 2011. **214**(5): p. 862-870.

17. Sachs, F., *Stretch-Activated Ion Channels: What Are They?* Physiology, 2010. **25**(1): p. 50-56.

18. Ingber, D.E., *Cellular mechanotransduction: putting all the pieces together again.* FASEB J., 2006. **20**(7): p. 811-827.

19. Camalet, S., et al., *Auditory sensitivity provided by self-tuned critical oscillations of hair cells.* Proceedings of the National Academy of Sciences, 2000. **97**(7): p. 3183-3188.

20. Cazals, Y., J.-M. Aran, and J.-P. Erre, *Frequency sensitivity and selectivity of acoustically evoked potentials after complete cochlear hair cell destruction.* Brain research, 1982. **231**(1): p. 197-203.

21. Hudspeth, A. and D. Corey, *Sensitivity, polarity, and conductance change in the response of vertebrate hair cells to controlled mechanical stimuli.*

Proceedings of the National Academy of Sciences, 1977. **74**(6): p. 2407-2411.

22. Todd, N.P.M., S.M. Rosengren, and J.G. Colebatch, *Tuning and sensitivity of the human vestibular system to low-frequency vibration.* Neuroscience letters, 2008. **444**(1): p. 36-41.

23. Ingber, D.E., *Cellular mechanotransduction: putting all the pieces together again.* The FASEB journal, 2006. **20**(7): p. 811-827.

24. García, J.R. and A.J. García, *Cellular mechanotransduction: sensing rigidity.* Nature materials, 2014. **13**(6): p. 539-540.

25. Sackin, H., *Stretch-activated ion channels.* Kidney international, 1995. **48**(4): p. 1134-1147.

26. Guharay, F. and F. Sachs, *Stretch-activated single ion channel currents in tissue-cultured embryonic chick skeletal muscle.* The Journal of physiology, 1984. **352**: p. 685.

27. Ding, J., R. Salvi, and F. Sachs, *Stretch-activated ion channels in guinea pig outer hair cells.* Hearing research, 1991. **56**(1): p. 19-28.

28. Kirber, M.T., J.V. Walsh Jr, and J.J. Singer, *Stretch-activated ion channels in smooth muscle: a mechanism for the initiation of stretch-induced contraction.* Pflügers Archiv, 1988. **412**(4): p. 339-345.

29. Engel, J.M., et al., *Polyurethane rubber all-polymer artificial hair cell sensor.* Microelectromechanical Systems, Journal of, 2006. **15**(4): p. 729-736.

30. Peleshanko, S., et al., *Hydrogel-Encapsulated Microfabricated Haircells Mimicking Fish Cupula Neuromast.* Advanced Materials, 2007. **19**(19): p. 2903-2909.

31. Park, H., et al., *A Hair-cell Structure based Piezoelectric Energy Harvester Operating under Three Dimensional Arbitrary Vibrations.* Journal of Physics: Conference Series, 2013. **476**(1): p. 012130.

32. Mountain, D.C. and A.E. Hubbard, *A piezoelectric model of outer hair cell function.* The Journal of the Acoustical Society of America, 1994. **95**(1): p. 350-354.

33. Engel, J., et al. *Polyurethane rubber as a MEMS material: characterization and demonstration of an all-polymer two-axis artificial hair cell flow sensor*. in *Micro Electro Mechanical Systems, 2005. MEMS 2005. 18th IEEE International Conference on*. 2005. IEEE.

34. Engel, J.M., et al., *Polyurethane rubber all-polymer artificial hair cell sensor.* Microelectromechanical Systems, Journal of, 2006. **15**(4): p. 729-736.

35. Abdulsadda, A.T. and X. Tan, *An artificial lateral line system using IPMC sensor arrays.* International Journal of Smart and Nano Materials, 2012. **3**(3): p. 226-242.

36. Dagamseh, A., et al., *Dipole-source localization using biomimetic flow-sensor arrays positioned as lateral-line system.* Sensors and Actuators A: Physical, 2010. **162**(2): p. 355-360.

37. Park, B.K. and J.S. Lee, *Dynamic behavior of flexible sensory hair in an oscillating flow.* Journal of mechanical science and technology, 2012. **26**(4): p. 1275-1282.

38. Masoud, H. and A. Alexeev, *Harnessing synthetic cilia to regulate motion of microparticles.* Soft Matter, 2011. **7**(19): p. 8702-8708.

39. Rizzi, F., et al., *Biomimetics of underwater hair cell sensing.* Microelectronic Engineering, 2015. **132**: p. 90-97.

40. Qualtieri, A., et al., *Stress-driven AlN cantilever-based flow sensor for fish lateral line system.* Microelectronic Engineering, 2011. **88**(8): p. 2376-2378.

41. Basak, S., A. Raman, and S.V. Garimella, *Dynamic response optimization of piezoelectrically excited thin resonant beams.* Journal of vibration and acoustics, 2005. **127**(1): p. 18-27.

42. Minne, S., S. Manalis, and C. Quate, *Parallel atomic force microscopy using cantilevers with integrated piezoresistive sensors and integrated piezoelectric actuators.* Applied Physics Letters, 1995. **67**(26): p. 3918-3920.

43. Jaffe, H. and D. Berlincourt, *Piezoelectric transducer materials.* Proceedings of the IEEE, 1965. **53**(10): p. 1372-1386.

44. Doron, E., Y. Porat, and Y. Tsaliah, *Piezoelectric transducer*. 2000, Google Patents.

45. Biot, M.A., *Theory of propagation of elastic waves in a fluid-saturated porous solid. I. Low-frequency range.* The Journal of the Acoustical Society of America, 1956. **28**(2): p. 168-178.

46. James, A.J., M.K. Smith, and A. Glezer, *Vibration-induced drop atomization and the numerical simulation of low-frequency single-droplet ejection.* Journal of Fluid Mechanics, 2003. **476**: p. 29-62.

47. Bawa, P. and R. Stein, *Frequency response of human soleus muscle.* J Neurophysiol, 1976. **39**(4): p. 788-793.

48. Frangioni, J.V., et al., *The mechanism of low-frequency sound production in muscle.* Biophysical journal, 1987. **51**(5): p. 775-783.

49. Mueller, P., et al., *Reconstitution of cell membrane structure in vitro and its transformation into an excitable system.* Nature, 1962. **194**: p. 979-980.

50. Tien, H.T., S. Carbone, and E. Dawidowicz, *Formation of "black" lipid membranes by oxidation products of cholesterol.* 1966.

51. Bayley, H., et al., *Droplet interface bilayers.* Molecular BioSystems, 2008. **4**(12): p. 1191-1208.

52. Davis, H., *Biophysics and physiology of the inner ear.* Physiological reviews, 1957. **37**(1): p. 1-49.

53. Hardin, P.J. and R.R. Jensen, *Small-scale unmanned aerial vehicles in environmental remote sensing: Challenges and opportunities.* GIScience & Remote Sensing, 2011. **48**(1): p. 99-111.

54. Holliday, D., et al., *Acoustical Sensing of Small-Scale Vertical.* MicroC AT sets the NEW standard in accurate moored CT instruments, 1998. **11**(1): p. 18.

55. Sarles, S.A. and D.J. Leo, *Physical encapsulation of droplet interface bilayers for durable, portable biomolecular networks.* Lab on a Chip, 2010. **10**(6): p. 710-717.

56. Sarles, S.A. and D.J. Leo, *Regulated attachment method for reconstituting lipid bilayers of prescribed size within flexible substrates.* Analytical chemistry, 2010. **82**(3): p. 959-966.

57. Danos, V. and C. Laneve, *Formal molecular biology.* Theoretical Computer Science, 2004. **325**(1): p. 69-110.

58. Alberts, B., et al., *Molecular biology of the cell, 1994.* Garland, New York: p. 139-194.

59. Daniels, B.S., et al., *Glomerular basement membrane: in vitro studies of water and protein permeability.* American Journal of Physiology-Renal Physiology, 1992. **262**(6): p. F919-F926.

60. SKou, J.C., *Enzymatic basis for active transport of Na+ and K+ across cell membrane.* Physiological Reviews, 1965. **45**(3): p. 596-618.

61. Yeagle, P.L., *Cholesterol and the cell membrane.* Biochimica et Biophysica Acta (BBA)-Reviews on Biomembranes, 1985. **822**(3): p. 267-287.

62. Cooper, R., et al., *Modification of red cell membrane structure by cholesterol-rich lipid dispersions. A model for the primary spur cell defect.* Journal of Clinical Investigation, 1975. **55**(1): p. 115.

63. Brown, M.S. and J.L. Goldstein, *The SREBP pathway: regulation of cholesterol metabolism by proteolysis of a membrane-bound transcription factor.* Cell, 1997. **89**(3): p. 331-340.

64. Hille, B., *Ion channels of excitable membranes*. Vol. 507. 2001: Sinauer Sunderland, MA.

65. Loewenstein, W.R., *Junctional intercellular communication: the cell-to-cell membrane channel.* Physiological Reviews, 1981. **61**(4): p. 829-913.

66. Cole, K.S. *Permeability and impermeability of cell membranes for ions*. in *Cold Spring Harbor Symposia on Quantitative Biology*. 1940. Cold Spring Harbor Laboratory Press.

67. Simons, K. and W.L. Vaz, *Model systems, lipid rafts, and cell membranes 1.* Annu. Rev. Biophys. Biomol. Struct., 2004. **33**: p. 269-295.

68. Latorre, R. and O. Alvarez, *Voltage-dependent channels in planar lipid bilayer membranes.* Physiological reviews, 1981. **61**(1): p. 77-150.

69. Tien, H.T. and A. Ottova, *The bilayer lipid membrane (BLM) under electrical fields.* Dielectrics and Electrical Insulation, IEEE Transactions on, 2003. **10**(5): p. 717-727.

70. Asami, K., T. Hanai, and N. Koizumi, *Dielectric properties of yeast cells.* The Journal of membrane biology, 1976. **28**(1): p. 169-180.

71. Needham, D. and R.S. Nunn, *Elastic deformation and failure of lipid bilayer membranes containing cholesterol.* Biophysical journal, 1990. **58**(4): p. 997.

72. Brown, A. and L. Birnbaumer, *Direct G protein gating of ion channels.* American Journal of Physiology-Heart and Circulatory Physiology, 1988. **254**(3): p. H401-H410.

73. Lindahl, E. and M.S. Sansom, *Membrane proteins: molecular dynamics simulations.* Current opinion in structural biology, 2008. **18**(4): p. 425-431.

74. Baumann, G. and P. Mueller, *A molecular model of membrane excitability.* Journal of supramolecular structure, 1974. **2**(5-6): p. 538-557.

75. Kagan, B.L., et al., *Antimicrobial defensin peptides form voltage-dependent ion-permeable channels in planar lipid bilayer membranes.* Proceedings of the National Academy of Sciences, 1990. **87**(1): p. 210-214.

76. Walter, A. and J. Gutknecht, *Permeability of small nonelectrolytes through lipid bilayer membranes.* The Journal of membrane biology, 1986. **90**(3): p. 207-217.

77. Deamer, D.W. and J. Bramhall, *Permeability of lipid bilayers to water and ionic solutes.* Chemistry and physics of lipids, 1986. **40**(2): p. 167-188.

78. Abidor, I., et al., *Electric breakdown of bilayer lipid membranes: I. The main experimental facts and their qualitative discussion.* Journal of Electroanalytical Chemistry and Interfacial Electrochemistry, 1979. **104**: p. 37-52.

79. Henn, F.A. and T.E. Thompson, *Synthetic lipid bilayer membranes.* Annual review of biochemistry, 1969. **38**(1): p. 241-262.

80. Szoka Jr, F. and D. Papahadjopoulos, *Comparative properties and methods of preparation of lipid vesicles (liposomes).* Annual review of biophysics and bioengineering, 1980. **9**(1): p. 467-508.

81. Eisenberg, M., J.E. Hall, and C. Mead, *The nature of the voltage-dependent conductance induced by alamethicin in black lipid membranes.* The Journal of membrane biology, 1973. **14**(1): p. 143-176.

82. Lin, W.-C., et al., *Lipid asymmetry in DLPC/DSPC-supported lipid bilayers: a combined AFM and fluorescence microscopy study.* Biophysical journal, 2006. **90**(1): p. 228-237.

83. Mashaghi, A., et al., *Optical anisotropy of supported lipid structures probed by waveguide spectroscopy and its application to study of supported lipid bilayer formation kinetics.* Analytical chemistry, 2008. **80**(10): p. 3666-3676.

84. Crane, J.M., V. Kiessling, and L.K. Tamm, *Measuring lipid asymmetry in planar supported bilayers by fluorescence interference contrast microscopy.* Langmuir, 2005. **21**(4): p. 1377-1388.

85. Castellana, E.T. and P.S. Cremer, *Solid supported lipid bilayers: From biophysical studies to sensor design.* Surface Science Reports, 2006. **61**(10): p. 429-444.

86. Naumann, R., et al., *Incorporation of Membrane Proteins in Solid-Supported Lipid Layers.* Angewandte Chemie International Edition in English, 1995. **34**(18): p. 2056-2058.

87. Cornell, B., et al., *Tethered-bilayer lipid membranes as a support for membrane-active peptides.* Biochemical Society Transactions, 2001. **29**(Pt 4): p. 613-617.

88. Schiller, S.M., et al., *Archaea analogue thiolipids for tethered bilayer lipid membranes on ultrasmooth gold surfaces.* Angewandte Chemie International Edition, 2003. **42**(2): p. 208-211.

89. McGillivray, D.J., et al., *Molecular-scale structural and functional characterization of sparsely tethered bilayer lipid membranes.* Biointerphases, 2007. **2**(1): p. 21-33.

90. Tanford, C., *The hydrophobic effect and the organization of living matter.* Science, 1978. **200**(4345): p. 1012-1018.

91. Tanford, C., *The Hydrophobic Effect: Formation of Micelles and Biological Membranes 2d Ed*. 1980: J. Wiley.

92. Chandler, D., *Interfaces and the driving force of hydrophobic assembly.* Nature, 2005. **437**(7059): p. 640-647.

93. McNaught, A.D. and A.D. McNaught, *Compendium of chemical terminology*. Vol. 1669. 1997: Blackwell Science Oxford.

94. Lang, H., C. Duschl, and H. Vogel, *A new class of thiolipids for the attachment of lipid bilayers on gold surfaces.* Langmuir, 1994. **10**(1): p. 197-210.

95. Torchilin, V.P., *Multifunctional nanocarriers.* Advanced drug delivery reviews, 2012. **64**: p. 302-315.

96. Israelachvili, J.N. and H. Wennerstroem, *Entropic forces between amphiphilic surfaces in liquids.* The Journal of Physical Chemistry, 1992. **96**(2): p. 520-531.

97. Sarles, S.A. and D.J. Leo, *Membrane-based biomolecular smart materials.* Smart materials and structures, 2011. **20**(9): p. 094018.

98. Chaudhury, M.K., *Self-assembled monolayers on polymer surfaces.* Biosensors and Bioelectronics, 1995. **10**(9): p. 785-788.

99. Kawano, R., et al., *A Portable Lipid Bilayer System for Environmental Sensing with a Transmembrane Protein.* PloS one, 2014. **9**(7): p. e102427.

100. Nielsen, C.H., *Biomimetic membranes for sensor and separation applications.* Analytical and bioanalytical chemistry, 2009. **395**(3): p. 697-718.

101. Wu, H.-C. and H. Bayley, *Single-molecule detection of nitrogen mustards by covalent reaction within a protein nanopore.* Journal of the American Chemical Society, 2008. **130**(21): p. 6813-6819.

102. Hwang, W.L., et al., *Electrical behavior of droplet interface bilayer networks: experimental analysis and modeling.* Journal of the American Chemical Society, 2007. **129**(38): p. 11854-11864.

103. Hwang, W.L., et al., *Asymmetric droplet interface bilayers.* Journal of the American Chemical Society, 2008. **130**(18): p. 5878-5879.

104. Maglia, G., et al., *Droplet networks with incorporated protein diodes show collective properties.* Nature nanotechnology, 2009. **4**(7): p. 437-440.

105. Holden, M.A., D. Needham, and H. Bayley, *Functional bionetworks from nanoliter water droplets.* Journal of the American Chemical Society, 2007. **129**(27): p. 8650-8655.

106. Reimhult, E. and K. Kumar, *Membrane biosensor platforms using nano- and microporous supports.* Trends in Biotechnology, 2008. **26**(2): p. 82-89.

107. Heitz, B.A., et al., *Polymerized Planar Suspended Lipid Bilayers for Single Ion Channel Recordings: Comparison of Several Dienoyl Lipids.* Langmuir, 2011. **27**(5): p. 1882-1890.

108. Punnamaraju, S., H. You, and A.J. Steckl, *Triggered Release of Molecules across Droplet Interface Bilayer Lipid Membranes Using Photopolymerizable Lipids.* Langmuir, 2012. **28**(20): p. 7657-7664.

109. Dorn, K., et al., *Permeability characteristics of polymeric bilayer membranes from methacryloyl and butadiene lipids.* Journal of the American Chemical Society, 1984. **106**(6): p. 1627-1633.

110. Benz, R., W. Prass, and H. Ringsdorf, *Black lipid membranes from polymerizable lipids.* Angewandte Chemie International Edition in English, 1982. **21**(S5): p. 869-880.

111. Cashion, M.P. and T.E. Long, *Biomimetic design and performance of polymerizable lipids.* Accounts of Chemical Research, 2009. **42**(8): p. 1016-1025.

112. Meier, W., *Polymer nanocapsules.* Chemical Society Reviews, 2000. **29**(5): p. 295-303.

113. Tanaka, H., et al., *Thermochromic phase transition of a polydiacetylene, poly (ETCD), studied by high-resolution solid-state carbon-13 NMR.* Macromolecules, 1989. **22**(3): p. 1208-1215.

114. Okada, S., et al., *Color and chromism of polydiacetylene vesicles.* Accounts of Chemical Research, 1998. **31**(5): p. 229-239.

115. Nardin, C., et al., *Nanoreactors based on (polymerized) ABA-triblock copolymer vesicles.* Chemical Communications, 2000(15): p. 1433-1434.

116. Meier, W., et al., *Stabilization of planar lipid membranes: A stratified layer approach.* Physical Chemistry Chemical Physics, 2000. **2**(20): p. 4559-4562.

117. Wong, D., T.-J. Jeon, and J. Schmidt, *Single molecule measurements of channel proteins incorporated into biomimetic polymer membranes.* Nanotechnology, 2006. **17**(15): p. 3710.

118. Nardin, C., M. Winterhalter, and W. Meier, *Giant Free-Standing ABA Triblock Copolymer Membranes.* Langmuir, 2000. **16**(20): p. 7708-7712.

119. Kowal, J., et al., *Planar Biomimetic Membranes Based on Amphiphilic Block Copolymers.* ACS Macro Letters, 2014. **3**(1): p. 59-63.

120. Gonzalez-Perez, A., et al., *Biomimetic triblock copolymer membranes: from aqueous solutions to solid supports.* Soft Matter, 2011. **7**(3): p. 1129-1138.

121. Morton, D., et al., *Tailored polymeric membranes for Mycobacterium smegmatis porin A (MspA) based biosensors.* Journal of Materials Chemistry B, 2015. **3**(25): p. 5080-5086.

122. Srinivas, G., D.E. Discher, and M.L. Klein, *Self-assembly and properties of diblock copolymers by coarse-grain molecular dynamics.* Nat Mater, 2004. **3**(9): p. 638-644.

123. Kamat, N.P., J.S. Katz, and D.A. Hammer, *Engineering Polymersome Protocells.* The Journal of Physical Chemistry Letters, 2011. **2**(13): p. 1612-1623.

124. Percec, V., et al., *Self-Assembly of Janus Dendrimers into Uniform Dendrimersomes and Other Complex Architectures.* Science, 2010. **328**(5981): p. 1009-1014.

125. Shen, Y.-x., et al., *Biomimetic membranes: A review.* Journal of Membrane Science, 2014. **454**: p. 359-381.

126. Srinivas, G., D.E. Discher, and M.L. Klein, *Key Roles for Chain Flexibility in Block Copolymer Membranes that Contain Pores or Make Tubes.* Nano Letters, 2005. **5**(12): p. 2343-2349.

127. Kumar, M., et al., *Highly permeable polymeric membranes based on the incorporation of the functional water channel protein Aquaporin Z.* Proceedings of the National Academy of Sciences, 2007. **104**(52): p. 20719-20724.

128. Itel, F., et al., *Dynamics of Membrane Proteins within Synthetic Polymer Membranes with Large Hydrophobic Mismatch.* Nano Letters, 2015. **15**(6): p. 3871-3878.

129. Mueller, P. and D.O. Rudin, *Action Potentials induced in Biomolecular Lipid Membranes.* Nature, 1968. **217**(5130): p. 713-719.

130. Mueller, P., et al., *Reconstitution of Excitable Cell Membrane Structure in Vitro.* Circulation, 1962. **26**: p. 1167-1171.

131. Montal, M. and P. Mueller, *Formation of Bimolecular Membranes from Lipid Monolayers and a Study of their Electrical Properties.* Proc. Nat. Acad. Sci. USA, 1972. **69**(12): p. 3561-3566.

132. Funakoshi, K., H. Suzuki, and S. Takeuchi, *Lipid Bilayer Formation by Contacting Monolayers in a Microfluidic Device for Membrane Protein Analysis.* Anal. Chem., 2006. **78**(24): p. 8169-8174.

133. Holden, M.A., D. Needham, and H. Bayley, *Functional Bionetworks from Nanoliter Water Droplets.* J. Am. Chem. Soc., 2007. **129**(27): p. 8650-8655.

134. Taylor, G.J. and S.A. Sarles, *Heating-Enabled Formation of Droplet Interface Bilayers Using Escherichia coli Total Lipid Extract.* Langmuir, 2015. **31**(1): p. 325-337.

135. Astafyeva, K., et al., *Stability of C12Ej Bilayers Probed with Adhesive Droplets.* Langmuir, 2015. **31**(24): p. 6791-6796.

136. Poulin, P., et al., *Evidence for newton black films between adhesive emulsion droplets.* Physical review letters, 1996. **77**(15): p. 3248.

137. Poulin, P. and J. Bibette, *Adhesion of Water Droplets in Organic Solvent.* Langmuir, 1998. **14**(22): p. 6341-6343.

138. Evans, E., *Adhesion of surfactant—membrane covered droplets: Special features and curvature elasticity effects.* Colloids and Surfaces, 1990. **43**(2): p. 327-347.

139. Poulin, P. and J. Bibette, *Adhesion between pure and mixed surfactant layers.* Langmuir, 1999. **15**(14): p. 4731-4739.

140. Jack, J.J.B., D. Noble, and R.W. Tsien, *Electric current flow in excitable cells*. 1975: Clarendon Press Oxford.

141. Goldman, D.E., *Potential, impedance, and rectification in membranes.* The Journal of General Physiology, 1943. **27**(1): p. 37-60.

142. Bordi, F., C. Cametti, and A. Gliozzi, *Impedance measurements of self-assembled lipid bilayer membranes on the tip of an electrode.* Bioelectrochemistry, 2002. **57**(1): p. 39-46.

143. Goldberg, S.N., et al., *Radio-Frequency Thermal Ablation with NaCl Solution Injection: Effect of Electrical Conductivity on Tissue Heating and Coagulation—Phantom and Porcine Liver Study 1.* Radiology, 2001. **219**(1): p. 157-165.

144. Römer, W. and C. Steinem, *Impedance analysis and single-channel recordings on nano-black lipid membranes based on porous alumina.* Biophysical journal, 2004. **86**(2): p. 955-965.

145. Tien, H.T. and A.L. Ottova, *The lipid bilayer concept and its experimental realization: from soap bubbles, kitchen sink, to bilayer lipid membranes.* Journal of membrane science, 2001. **189**(1): p. 83-117.

146. Pethig, R., *Dielectric and electrical properties of biological materials.* Electromagnetic Biology and Medicine, 1985. **4**(2): p. vii-ix.

147. Thiam, A.R., N. Bremond, and J.r.m. Bibette, *From stability to permeability of adhesive emulsion bilayers.* Langmuir, 2012. **28**(15): p. 6291-6298.

148. Poulin, P. and J. Bibette, *Wetting of emulsions droplets: From macroscopic to colloidal scale.* Physical review letters, 1997. **79**(17): p. 3290.

149. White, S., *Formation of" solvent-free" black lipid bilayer membranes from glyceryl monooleate dispersed in squalene.* Biophysical journal, 1978. **23**(3): p. 337.

150. Sarles, S.A. and D.J. Leo, *Tailored current-voltage relationships of droplet-interface bilayers using biomolecules and external feedback control.* Journal of intelligent material systems and structures, 2009.

151. Helfrich, W., *Elastic properties of lipid bilayers: theory and possible experiments.* Z. Naturforsch. c, 1973. **28**(11): p. 693-703.

152. Ide, T. and T. Ichikawa, *A novel method for artificial lipid-bilayer formation.* Biosensors and Bioelectronics, 2005. **21**(4): p. 672-677.

153. Hudspeth, A.J. and D.P. Corey, *Sensitivity, polarity, and conductance change in the response of vertebrate hair cells to controlled mechanical stimuli.* Proceedings of the National Academy of Sciences, 1977. **74**(6): p. 2407-2411.

154. Crawford, A.C. and R. Fettiplace, *The frequency selectivity of auditory nerve fibres and hair cells in the cochlea of the turtle.* The Journal of Physiology, 1980. **306**(1): p. 79-125.

155. Roberts, W., R. Jacobs, and A. Hudspeth, *Colocalization of ion channels involved in frequency selectivity and synaptic transmission at presynaptic active zones of hair cells.* The Journal of Neuroscience, 1990. **10**(11): p. 3664-3684.

156. Brundin, L., A. Flock, and B. Canlon, *Sound-induced motility of isolated cochlear outer hair cells is frequency-specific.* Nature, 1989. **342**(6251): p. 814-816.

157. Taylor, G.J., et al., *Direct in situ measurement of specific capacitance, monolayer tension, and bilayer tension in a droplet interface bilayer.* Soft Matter, 2015. **11**(38): p. 7592-7605.

158. Nguyen, M.-A., N. Tamaddoni, and S.A. Sarles. *Interrogation of Bilayers in a Multi-Droplet Cluster for Membrane-Based Sensing*. in *ASME 2015 Conference on Smart Materials, Adaptive Structures and Intelligent Systems*. 2015. American Society of Mechanical Engineers.

159. Sarles, S.A., et al., *Bilayer Formation between Lipid-Encased Hydrogels Contained in Solid Substrates.* ACS Applied Materials & Interfaces, 2010. **2**(12): p. 3654-3663.

160. Gross, L.C.M., et al., *Determining Membrane Capacitance by Dynamic Control of Droplet Interface Bilayer Area.* Langmuir, 2011. **27**(23): p. 14335-14342.

161. Thompson, J.R., et al., *Enhanced Stability and Fluidity in Droplet on Hydrogel Bilayers for Measuring Membrane Protein Diffusion.* Nano Lett., 2007. **7**(12): p. 3875-3878.

162. Heron, A.J., et al., *Direct Detection of Membrane Channels from Gels Using Water-in-Oil Droplet Bilayers.* J. Am. Chem. Soc., 2007. **129**(51): p. 16042-16047.

163. Hwang, W.L., et al., *Asymmetric Droplet Interface Bilayers.* Journal of the American Chemical Society, 2008. **130**(18): p. 5878-5879.

164. Tamaddoni, N. and A. Sarles. *Characterizing the sources of current generated by a membrane-based hair cell sensor*. in *ASME 2013 Conference on Smart Materials, Adaptive Structures and Intelligent Systems*. 2013. American Society of Mechanical Engineers.

165. Todorov, A.T., A.G. Petrov, and J.H. Fendler, *First Observation of the Converse Flexoelectric Effect in Bilayer Lipid Membranes.* The Journal of Physical Chemistry, 1994. **98**(12): p. 3076-3079.

166. Todorov, A.T., A.G. Petrov, and J.H. Fendler, *Flexoelectricity of Charged and Dipolar Bilayer Lipid Membranes Studied by Stroboscopic Interferometry.* Langmuir, 1994. **10**(7): p. 2344-2350.

167. Sarles, S.A., *The use of virtual ground to control transmembrane voltages and measure bilayer currents in serial arrays of droplet interface bilayers.* Smart Materials and Structures, 2013. **22**(9): p. 094023.

168. Villar, G., A.J. Heron, and H. Bayley, *Formation of droplet networks that function in aqueous environments.* Nat Nano, 2011. **6**(12): p. 803-808.

169. Elani, Y., et al., *Novel technologies for the formation of 2-D and 3-D droplet interface bilayer networks.* Lab on a Chip, 2012. **12**(18): p. 3514-3520.

170. Wauer, T., et al., *Construction and Manipulation of Functional Three-Dimensional Droplet Networks.* ACS Nano, 2013. **8**(1): p. 771-779.

171. Villar, G., A.D. Graham, and H. Bayley, *A Tissue-Like Printed Material.* Science, 2013. **340**(6128): p. 48-52.

172. Tamaddoni, N., E.C. Freeman, and S.A. Sarles, *Sensitivity and directionality of lipid bilayer mechanotransduction studied using a revised, highly durable membrane-based hair cell sensor.* Smart Materials and Structures, 2015. **24**(6): p. 065014.

173. McGary, P.D., et al., *Magnetic nanowires for acoustic sensors.* Journal of Applied Physics, 2006. **99**(8): p. 08B310.

174. Liu, C., *Micromachined biomimetic artificial haircell sensors.* Bioinspiration & biomimetics, 2007. **2**(4): p. S162.

175. Peleshanko, S., et al., *Hydrogel-Encapsulated Microfabricated Haircells Mimicking Fish Cupula Neuromast.* Advanced materials, 2007. **19**(19): p. 2903-2909.

176. McConney, M.E., et al., *Biologically inspired design of hydrogel-capped hair sensors for enhanced underwater flow detection.* Soft Matter, 2009. **5**(2): p. 292-295.

177. Kottapalli, A.G., et al., *A flexible liquid crystal polymer MEMS pressure sensor array for fish-like underwater sensing.* Smart Materials and Structures, 2012. **21**(11): p. 115030.

178. Droogendijk, H., et al., *A biomimetic accelerometer inspired by the cricket's clavate hair.* Journal of the Royal Society interface, 2014. **11**(97): p. 20140438.

179. Pang, C., et al., *Highly Skin-Conformal Microhairy Sensor for Pulse Signal Amplification.* Advanced Materials, 2015. **27**(4): p. 634-640.

180. Kottapalli, A.G.P., et al., *Nanofibril scaffold assisted MEMS artificial hydrogel neuromasts for enhanced sensitivity flow sensing.* Scientific reports, 2016. **6**: p. 19336.

181. Hudspeth, A., *Extracellular current flow and the site of transduction by vertebrate hair cells.* The Journal of Neuroscience, 1982. **2**(1): p. 1-10.

182. Robles, L. and M.A. Ruggero, *Mechanics of the Mammalian Cochlea.* Physiological Reviews, 2001. **81**(3): p. 1305-1352.

183. Ashmore, J., *Cochlear Outer Hair Cell Motility.* Physiological Reviews, 2008. **88**(1): p. 173-210.

184. Elliott, S.J. and C.A. Shera, *The cochlea as a smart structure.* Smart Materials and Structures, 2012. **21**(6): p. 064001.

185. Hudspeth, A., *The cellular basis of hearing: the biophysics of hair cells.* Science, 1985. **230**(4727): p. 745-752.

186. Hudspeth, A., et al., *Putting ion channels to work: mechanoelectrical transduction, adaptation, and amplification by hair cells.* Proceedings of the National Academy of Sciences, 2000. **97**(22): p. 11765-11772.

187. Najem, J.S., et al., *Multifunctional, Micropipette-based Method for Incorporation And Stimulation of Bacterial Mechanosensitive Ion Channels in Droplet Interface Bilayers.* 2015(105): p. e53362.

188. Najem, J.S., et al., *Activation of bacterial channel MscL in mechanically stimulated droplet interface bilayers.* Scientific Reports, 2015. **5**: p. 13726.

189. Syeda, R., et al., *Screening blockers against a potassium channel with a droplet interface bilayer array.* Journal of the American Chemical Society, 2008. **130**(46): p. 15543-15548.

190. Freeman, E., M.A. Creasy, and D.J. Leo, *Deterministic models of bilayer networks with stimuli-responsive properties.* Smart Materials and Structures, 2012. **under review**.

191. Creasy, M.A., et al., *Deterministic model of biomolecular networks with stimuli-responsive properties.* Journal of Intelligent Material Systems and Structures, 2015. **26**(8): p. 921-930.

192. Pelrine, R., et al. *Dielectric elastomer artificial muscle actuators: toward biomimetic motion*. in *SPIE's 9th Annual International Symposium on Smart Structures and Materials*. 2002. International Society for Optics and Photonics.

193. Bruhn, B.R., et al., *Osmosis-based pressure generation: dynamics and application.* PloS one, 2014. **9**(3): p. e91350.

194. Schroeder, T.B., et al., *Dynamics of Bio-Inspired Pressure Generation.* Biophysical Journal, 2014. **106**(2): p. 615a.

195. Punnamaraju, S. and A.J. Steckl, *Voltage Control of Droplet Interface Bilayer Lipid Membrane Dimensions.* Langmuir, 2010. **27**(2): p. 618-626.

196. Barth, F.G., *Spider senses–technical perfection and biology.* Zoology, 2002. **105**(4): p. 271-285.

197. Baconguis, I. and E. Gouaux, *Structural plasticity and dynamic selectivity of acid-sensing ion channel-spider toxin complexes.* Nature, 2012. **489**(7416): p. 400-405.

198. Fan, Z., et al., *Design and fabrication of artificial lateral line flow sensors.* Journal of Micromechanics and Microengineering, 2002. **12**(5): p. 655.

199. Yang, Y., et al., *Artificial lateral line with biomimetic neuromasts to emulate fish sensing.* Bioinspiration & biomimetics, 2010. **5**(1): p. 016001.

200. Crissman, H., P. Mullaney, and J. Steinkamp, *Methods and applications of flow systems for analysis and sorting of mammalian cells.* Methods Cell Biol, 1975. **9**(0): p. 179-246.

201. Sukharev, S.I., et al., *A large-conductance mechanosensitive channel in E. coli encoded by mscL alone.* Nature, 1994. **368**(6468): p. 265-268.

202. Gross, L.C., et al., *Determining membrane capacitance by dynamic control of droplet interface bilayer area.* Langmuir, 2011. **27**(23): p. 14335-14342.

203. Sarles, S.A. and D.J. Leo, *Tailored Current—Voltage Relationships of Droplet-Interface Bilayers Using Biomolecules and External Feedback Control.* Journal of Intelligent Material Systems and Structures, 2009. **20**(10): p. 1233-1247.

204. Tamaddoni, N., et al., *Reversible, voltage-activated formation of biomimetic membranes between triblock copolymer-coated aqueous droplets in good solvents.* Soft Matter - Royal Society of Chemistry, 2016.

205. Thompson, J.R., et al., *Enhanced stability and fluidity in droplet on hydrogel bilayers for measuring membrane protein diffusion.* Nano letters, 2007. **7**(12): p. 3875-3878.

206. Taylor, G.J. and S.A. Sarles, *Heating-enabled formation of droplet interface bilayers using Escherichia coli total lipid extract.* Langmuir, 2014. **31**(1): p. 325-337.

207. Hwang, W.L., et al., *Asymmetric Droplet Interface Bilayers.* J. Am. Chem. Soc., 2008. **130**(18): p. 5878-5879.

208. Mruetusatorn, P., et al., *Control of Membrane Permeability in Air-Stable Droplet Interface Bilayers.* Langmuir, 2015. **31**(14): p. 4224-4231.

209. Boreyko, J.B., et al., *Air-stable droplet interface bilayers on oil-infused surfaces.* Proceedings of the National Academy of Sciences, 2014. **111**(21): p. 7588-7593.

210. Heron, A.J., et al., *Simultaneous Measurement of Ionic Current and Fluorescence from Single Protein Pores.* Journal of the American Chemical Society, 2009. **131**(5): p. 1652-1653.

211. Gross, L.C.M., O.K. Castell, and M.I. Wallace, *Dynamic and Reversible Control of 2D Membrane Protein Concentration in a Droplet Interface Bilayer.* Nano Letters, 2011. **11**(8): p. 3324-3328.

212. *Polymer handbook*, J. Brandrup, E.H. Immergut, and E.A. Grulke, Editors. 1999, New York : Wiley-Interscience: New York.

213. Othman, M.B.H., et al., *Dielectric constant and refractive index of poly (siloxane–imide) block copolymer.* Materials & Design, 2011. **32**(6): p. 3173-3182.

214. White, S.H., *The lipid bilayer as a `solvent' for small hydrophobic molecules.* Nature, 1976. **262**(5567): p. 421-422.

215. White, S.H., *Formation of "solvent-free" black lipid bilayer membranes from glyceryl monooleate dispersed in squalene.* Biophys. J., 1978. **23**(3): p. 337-347.

216. Valincius, G., et al., *Soluble Amyloid β-Oligomers Affect Dielectric Membrane Properties by Bilayer Insertion and Domain Formation: Implications for Cell Toxicity.* Biophysical Journal, 2008. **95**(10): p. 4845-4861.

217. Israelachvili, J.N., *Intermolecular and Surface Forces (3rd Edition)*. 2011, Saint Louis, MO, USA: Academic Press.

218. Beaucage, G., et al., *Symmetric, Isotopic Blends of Poly(dimethylsiloxane).* Macromolecules, 1996. **29**(26): p. 8349-8356.

219. McIntosh, T.J., S. Simon, and R. MacDonald, *The organization of n-alkanes in lipid bilayers.* Biochimica et Biophysica Acta (BBA)-Biomembranes, 1980. **597**(3): p. 445-463.

220. Requena, J. and D.A. Haydon, *The lippmann equation and the characterization of black lipid films.* Journal of Colloid and Interface Science, 1975. **51**(2): p. 315-327.

221. Venkatesan, G.A., et al., *Adsorption Kinetics Dictate Monolayer Self-Assembly for Both Lipid-In and Lipid-Out Approaches to Droplet Interface Bilayer Formation.* Langmuir, 2015. **31**(47): p. 12883-12893.

222. de Gennes, P.G., *Conformations of Polymers Attached to an Interface.* Macromolecules, 1980. **13**(5): p. 1069-1075.

223. Thiam, A.R., N. Bremond, and J. Bibette, *From Stability to Permeability of Adhesive Emulsion Bilayers.* Langmuir, 2012. **28**(15): p. 6291-6298.

224. Needham, D. and D.A. Haydon, *Tensions and free energies of formation of "solventless" lipid bilayers. Measurement of high contact angles.* Biophys. J., 1983. **41**(3): p. 251-257.

225. Liu, Z., et al., *Droplet-based electro-coalescence for probing threshold disjoining pressure.* Lab on a Chip, 2015. **15**(9): p. 2018-2024.

226. Stokes, G.G., *On the effect of the internal friction of fluids on the motion of pendulums.* Transactions of the Cambridge Philosophical Society, 1851. **9**: p. 8-106.

227. Fletcher, N.H., *Acoustical response of hair receptors in insects.* Journal of comparative physiology, 1978. **127**(2): p. 185-189.

228. Devarakonda, R., F.G. Barth, and J.A.C. Humphrey, *Dynamics of Arthropod Filiform Hairs. IV. Hair Motion in Air and Water.* Philosophical Transactions of the Royal Society of London B: Biological Sciences, 1996. **351**(1342): p. 933-946.

229. Humphrey, J.A.C., et al., *Dynamics of Arthropod Filiform Hairs. I. Mathematical Modelling of the Hair and Air Motions.* Philosophical Transactions of the Royal Society of London B: Biological Sciences, 1993. **340**(1294): p. 423-444.

230. Chakraborty, A., S. Gopalakrishnan, and J. Reddy, *A new beam finite element for the analysis of functionally graded materials.* International Journal of Mechanical Sciences, 2003. **45**(3): p. 519-539.

231. Marsh, D., *Elastic curvature constants of lipid monolayers and bilayers.* Chemistry and Physics of Lipids, 2006. **144**(2): p. 146-159.

232. Campelo, F., et al., *Helfrich model of membrane bending: From Gibbs theory of liquid interfaces to membranes as thick anisotropic elastic layers.* Advances in Colloid and Interface Science, 2014. **208**: p. 25-33.

233. Dixit, S.S., et al., *Droplet Shape Analysis and Permeability Studies in Droplet Lipid Bilayers.* Langmuir, 2012. **28**(19): p. 7442-7451.

234. Helfrich, W., *Elastic properties of lipid bilayers: theory and possible experiments.* Zeitschrift für Naturforschung C, 1973. **28**(11-12): p. 693-703.

235. Bassereau, P., B. Sorre, and A. Lévy, *Bending lipid membranes: Experiments after W. Helfrich's model.* Advances in Colloid and Interface Science, 2014. **208**: p. 47-57.

236. Ochs, A.L. and R.M. Burton, *Electrical response to vibration of a lipid bilayer membrane.* Biophysical journal, 1974. **14**(6): p. 473.

237. Petrov, A.G. and P.N. Usherwood, *Mechanosensitivity of cell membranes.* European biophysics journal, 1994. **23**(1): p. 1-19.

238. Vitkova, V., et al., *Alamethicin influence on the membrane bending elasticity.* European Biophysics Journal, 2006. **35**(3): p. 281-286.

239. Nguyen, M., et al., *Hydrodynamic trapping for rapid assembly and in situ electrical characterization of droplet interface bilayer arrays* Lab Chip, 2016. **submitted**.

240. Bermudez, H., D. Hammer, and D. Discher, *Effect of bilayer thickness on membrane bending rigidity.* Langmuir, 2004. **20**(3): p. 540-543.

241. Evans, E., W. Rawicz, and B. Smith, *Concluding remarks back to the future: mechanics and thermodynamics of lipid biomembranes.* Faraday discussions, 2013. **161**: p. 591-611.

VITA

Nima Tamaddoni, born in May 1, 1986, is the youngest son of Mitra Hashemian and Essy Tamaddoni and younger brother of Tina and Tannaz Tamaddoni.Nima has finished his Bachlor's, Masters and PhD of Mechanical Engineering from the University of Tennessee with over 10 high impact journal and conference publications and two patents. While working on his PhD under supervision of Dr. Andy Sarles, he and his business partner invented the world's first single use liposme extruder as their first product of their startup company, filed for a patent, and ready to commercialize the product worldwide. The health care industry and research scientists have already embraced this product. Nima's focus at T&T is on business development and marketing strategies of the products and services. A proven entrepreneur and a successful student and business owner, Nima has demonstrated at an early age that perseverance and hard work pays dividend as evident in the success of this product early in its launch. With an eminent PhD in Mechanical Engineering and a relentless personality; Nima is proving himself not only as a talented innovator but also a "visionary businessman".